

QUANTUM SENSING WITH SQUEEZED LIGHT

A Dissertation

by

FU LI

Submitted to the Office of Graduate and Professional Studies of
Texas A&M University

in partial fulfillment of the requirements for the degree of

DOCTOR OF PHILOSOPHY

Chair of Committee,	Marlan O. Scully
Co-Chairs of Committee,	Marlan O. Scully Girish Agarwal
Committee Members,	Alexei Sokolov, M. Suhail Zubairy,
Head of Department,	Grigory Rogachev

May 2021

Major Subject: Physics

Copyright 2021 Fu Li

ABSTRACT

In this dissertation, a twin-beam squeezed state combined with various experiments and computational techniques were applied to investigate quantum systems including quantum sensing and quantum coherence. These quantum ideas can provide us with methodologies to achieve unprecedented sensitivity and resolution for sensing and imaging, which is far beyond the classical measurement could achieve. These new methods based on quantum physics are revolutionizing the scales at which one can do sensing, imaging and microscopy with applications in diverse fields from physics and engineering to chemical, biology and medicine. The quantum sensing has clear bearing on many future technologies.

In our lab, the quantum light source is a twin-beam squeezed state, which is generated via four-wave mixing nonlinear processes in a ^{85}Rb vapor cell. Our goal is to develop novel quantum sensing techniques by engineering quantum light sources and by improving the quantumness of these sources, so that they can be utilized in proof of principle applications as well as other related applications, such as the weak absorption measurement, decoherence investigation, and two-photon microscopy.

To investigate the quantum system, we first measured the quantumness of the twin-beam squeezed state, which has 6.5dB squeezed noise below the shot-noise limit. We demonstrated that an electron-multiplying charge-coupled-device EMCCD camera can capture the temporal images which provides the dynamic information. Thus, EMCCD camera can be used to measure the temporal quantum noise of twin beams squeezed light, and we observed $\sim 25\%$ of temporal quantum noise reduction with respect to the shot-noise limit, which was given by coherent state. To the best of our knowledge, this is the first experimental showcase that an EMCCD camera can be used to acquire quantum properties of light in the temporal domain.

One of the most serious challenges to the implementation of quantum technology, such as quantum communication and quantum methodology, is decoherence, which due to the quantum state interacting with environment. The quantum decoherence has been extensively investigated theo-

retically. Thus, we report a novel experimental scheme on the study of decoherence of a two-mode squeezed vacuum state via its second harmonic generation signal. One of the most important properties of squeezed light is the nonzero quantum correlation $\langle \hat{a}\hat{b} \rangle$ between two entangled modes \hat{a} and \hat{b} , our scheme can directly extract the decoherence of this quantum correlation. This is the first experimental study on the decoherence effect of a squeezed vacuum state, and also the first experimental study on the decoherence effect of a squeezed vacuum state without full density matrix tomography. We obtain a good agreement between the experimental results and the theoretical calculation.

Based on the quantumness of the twin-beam squeezed state, we demonstrated that direct absorption measurement can be performed with sensitivity beyond the shot-noise limit. By using laser beam, the theoretical absorption measurement limit which be called the shot noise, is due to the fundamental Poisson distribution of photon number of laser radiation. With the twin-beam squeezed state, we present detailed theoretical analysis for the expected quantum advantage, which well agrees with experimental result. More than 1.2 dB quantum advantage for the measurement sensitivity is obtained at faint absorption levels ($\leq 10\%$). The observed quantum advantage when corrected for optical loss would be equivalent to 3 dB.

Another quantum application of the twin-beam squeezed state is two-photon absorption (TPA) fluorescence sensing or imaging. For a classical illumination, the TPA is extremely small and the quadratic dependence on the input photon flux, which means that high peak-intensity pulsed laser are used to get a faithful result. However, the bio-sample or biological specimen may be damaged by such strong peak-intensity pulsed laser. Here, we report that by using a two-mode squeezed light source for TPA, a linear dependence on the input photon- pair flux is obtained. An enhancement of ~ 47 is achieved in fluorescein biomarkers as compared to classical TPA with CW excitation.

Finally, we investigated beyond sub-Rayleigh imaging via high order correlation of speckle illumination. We provide experimental evidence by demonstrating resolution beyond what is achievable by second order correlations. We present results up to 25^{th} order. We also show an increased visibility of cumulant correlations compared to moment correlations. The correlation algorithm

also be used in bio-imaging, and we demonstrated that the correlation do provide the map of water moving in a bio-sample. Our findings clearly suggest the benefits of using higher order intensity cumulants in other disciplines like astronomy and biology.

DEDICATION

To my family
who love and support me all the time.

ACKNOWLEDGMENTS

First, I would like to express my sincere gratitude to my advisors Dr. Marlan O. Scully and Dr. Girish Agarwal for all their support, encouragement and patience during these years. Their scientific insights always inspired me and I enjoyed all the work and discussions we had during my graduate study. I am deeply appreciative of my committee member Dr. M. Suhail Zubairy and Dr. Alexei Sokolov, for their time and suggestions.

I would also like to extend my deepest gratitude to Dr. Tian Li and Dr. Charles Altuzarra, who trained me to be an experimentalist in the field of quantum optics. We have worked together on many experiment projects over years and successfully published the work. I would like to thank all my colleagues in IQSE group: Dr. Kai Wang, Dr. Anatoly A. Svidzinsky, Zehua Han, Jizhou Wang, Dr. Ze he, Dr. Shengwen Li, Dr. Tao Peng, Dr. Anton Classen. It was a great pleasure to work with all of them and I deeply appreciate all their help and suggestions.

Last but not least, I deeply thank my parents for their unconditional trust, timely encouragement, and endless patience. It was their love that raised me up again when I got weary. The family of my sister have also been generous with their love and encouragement despite the long distance between us.

CONTRIBUTORS AND FUNDING SOURCES

Contributors

This work was supported by a dissertation committee consisting of Professors Marlan O. Scully[co-advisor] of the Department of Physics and Astronomy, Girish Agarwal[co-advisor] of the Department of Biological and Agricultural Engineering and Department of Physics and Astronomy, M. Suhail Zubairy and Alexei Sokolov of the Department of Physics and Astronomy.

The four-wave mixing (FWM) setup were prepared by Dr.Tian Li and maintained by Dr. Tian Li and me. The theoretical simulation of quantum advantage for absorption in Chapter 4 were done by Dr.Tian Li. The DCM laser dye and fluorescein samples in Chapter 5 were prepared by Dr.Tian Li, and experiment data was collected by Tian Li and me. In Chapter 6, the mask object was prepared and designed by Dr.Charles Altuzarra and me.

All other work conducted for the dissertation was completed by myself independently.

Funding Sources

Graduate study were supported by by the Herman F. Heep and Minnie Belle Heep Texas A&M University Endowed Fund held/administered by the Texas A&M Foundation, AFOSR, Office of Naval Research and Robert A. Welch Foundation.

NOMENCLATURE

CW	Continuous-Wave
SQL	Standard Quantum Limit
4WM	Four-Wave Mixing
PIA	Phase-Insensitive Amplifier
PSA	Phase-Sensitive Amplifiers
EPR	Einstein-PodolskyRosen
CCD	Charge-Coupled-Device
EMCCD	Electron-Multiplying Charge-Coupled-Device
AOM	Acousto-Optic Modulator
SPDCs	Spontaneous Parametric Down-Converters
BBO	Beta Barium Borate
TMSV	Two-Mode Squeezed Vacuum
SHG	Second Harmonic generation
ND	neutral density
CSi	Cauchy-Schwartz inequalities
DC	Direct Current
TPA	Two-Photon Absorption
ETPA	Entangled TPA
PMT	PhotoMultiplier Tube
CMOS	Complementary Metal–Oxide–Semiconductor
sCOMS	Scientific CMOS
PSF	Point-Spread Function

SBS

Stimulated Brillouin Scattering

TABLE OF CONTENTS

	Page
ABSTRACT	ii
DEDICATION	v
ACKNOWLEDGMENTS	vi
CONTRIBUTORS AND FUNDING SOURCES	vii
NOMENCLATURE	viii
TABLE OF CONTENTS	x
LIST OF FIGURES	xiii
1. INTRODUCTION AND LITERATURE REVIEW	1
1.1 Four-wave mixing	2
1.2 Phase-insensitive amplifier	5
1.3 Quantum mechanics for linear optical amplifiers.....	7
1.3.1 Correlation between two-modes squeezed vacuum.....	12
1.3.2 Intensity difference of Two-modes squeezed state	14
1.4 Outline	15
2. TEMPORAL QUANTUM NOISE REDUCTION ACQUIRED BY AN ELECTRON- MULTIPLYING CHARGE-COUPLED-DEVICE CAMERA	18
2.1 Introduction.....	18
2.2 Experimental setup.....	21
2.3 Results & Analysis.....	25
2.3.1 Temporal two-mode squeezing measured by photodiodes	25
2.3.2 Temporal quantum noise reduction acquired by an EMCCD camera.....	25
2.4 Conclusions.....	29
3. EXPERIMENTAL STUDY OF DECOHERENCE OF THE TWO-MODE SQUEEZED VACUUM STATE VIA SECOND HARMONIC GENERATION	31
3.1 Introduction.....	31
3.2 Theoretical Analysis	33
3.2.1 Cauchy-Schwartz inequity violation for the phase-sensitive correlation $\langle \hat{a}\hat{b} \rangle$.	33

3.2.2	Characterization of decoherence of two-mode squeezed vacuum state via its SHG signal	35
3.2.3	Characterization of decoherence of the two-mode squeezed vacuum state via its SHG signal	37
3.3	Experiment and Results	38
3.3.1	Experimental setup	38
3.3.2	Results	40
3.4	Conclusions.....	43
4.	OBSERVATION OF QUANTUM ADVANTAGE WITH SQUEEZED LIGHT FOR ABSORPTION MEASUREMENT	46
4.1	introduction.....	46
4.2	Theoretical analysis of the quantum advantage for measurement sensitivity	49
4.3	Experimental demonstration of the quantum advantage	51
4.4	Results and Analysis	56
4.5	Discussion	61
4.6	Methods.....	62
4.6.1	Squeezing measurement.....	63
4.6.2	EMCCD camera settings	64
5.	SQUEEZED LIGHT INDUCED TWO-PHOTON ABSORPTION FLUORESCENCE OF FLUORESC EIN BIOMARKERS.....	65
5.1	Second-order perturbation theory for two-photon process	65
5.2	Experiment	74
5.2.1	DCM in DMSO.....	77
5.3	Raw data and post-processing	81
5.4	Conclusions.....	82
6.	BEYOND SUB-RAYLEIGH IMAGING VIA HIGH ORDER CORRELATION OF SPECKLE ILLUMINATION.....	85
6.1	Introduction.....	85
6.2	Theoretical Basis	86
6.3	Experimental Results	89
6.4	Bio-imaging via correlation	95
6.5	Conclusion.....	95
6.6	Correlation calculation.....	98
6.7	The cumulant formulas	99
7.	CONCLUDING REMARKS	101
7.1	Summary of results	101
7.2	Outlook	102
7.2.1	Stimulated Brillouin scattering	103

REFERENCES105

LIST OF FIGURES

FIGURE	Page
1.1 Energy (a) and momentum (b) conservation in the 4WM, where $\omega_1, \omega_2, \omega_3, \omega_4$ are three angular frequencies of input fields, and $\vec{k}_1, \vec{k}_2, \vec{k}_3$ are three wave vectors. The relation between wave vectors k_i and angular frequencies ω_i are given by $k_i = n_i \omega_i / c$	3
1.2 4-level double- Λ atomic configuration.	5
1.3 Experiment sketch and atomic energy diagram for PIA, where a very strong pump beam is used to drive the 4WM runing. One port is seeded with a probe beam, and another is seeded with a vacuum state. Due to the 4WM interactions, an amplified probe beam and a new generated conjugate beam are emitted, where Δ and δ present the one- and two-photon detuning, respectively.	6
1.4 (a) Experiment realization and atomic energy diagram represented with operators. One port is seeded with a probe beam, and another is seeded with a vacuum state. Three inputs are crossed at the center of the atomic vapor with a small relative angle to fulfill the phase matching condition. (b) The atomic level scheme, two ground states and one excited state with three input modes a, b and c, where Δ and δ present the one- and two-photon detuning, respectively.	8
1.5 Two-mode intensity difference squeezing as a function of G_{PIA}	15
2.1 (a) Experimental setup in which a seeded ^{85}Rb vapor cell produces strong quantum-correlated twin beams via FWM. The twin beams are separated from the pump by a $2 \times 10^5 : 1$ polarizer and then focused onto the EMCCD camera. The camera is enclosed in a light-proof box with filters mounted to block ambient light. The AOM on the probe beam path is used to pulse the twin beams with $1 \mu\text{s}$ FWHM and duty cycle of $1/12$. PBS: polarizing beam splitter, PM fiber: polarization-maintaining fiber. (b) Level structure of the D1 transition of ^{85}Rb atom. The optical transitions are arranged in a double- Λ configuration, where ν_p, ν_c and ν_1 stand for probe, conjugate and pump frequencies, respectively, fulfilling $\nu_p + \nu_c = 2\nu_1$. The width of the excited state in the level diagram represents the Doppler broadened line. Δ is the one-photon detuning, δ is the two-photon detuning, and ν_{HF} is the hyperfine splitting in the electronic ground state of ^{85}Rb	20

2.2	(a) Time sequencing of the pump and twin beams. The pulse duration of $1 \mu\text{s}$ and the duty cycle of $1/12$ is realized by pulsing the probe beam with an AOM. The CW pump beam is present all the time. (b) Typical images of the twin beams captured by the EMCCD camera with four consecutive pulses.	22
2.3	Temporal photon counts fluctuations of the probe $N_p(t)$ and conjugate $N_c(t)$ obtained by integrating the photon counts in the cropped regions in fig. 4.3. Clear similarities can be observed between the twin beams. The strong noise reduction in the subtraction as opposed to the summation of the $N_p(t)$ and $N_c(t)$ depicted in showcases strong correlations between them. The factor of 0.8 is for a better different fluctuation reduction.	23
2.4	Temporal photon counts fluctuations obtained by integrating the photon counts in the cropped regions of two independent coherent beams. The beam size of two coherent beam is same with the size of probe and conjugate beam, and the EMCCD setting is also identical.	24
2.5	Intensity-difference noise power spectrum for the squeezed twin beams (blue line) and for the standard quantum limit (red line), obtained by a balanced photodetector in conjunction with a radio frequency spectrum analyzer (with a resolution and video frequency bandwidth of 300 kHz and 100 Hz, respectively). A two-mode squeezing of 6.5 dB is achieved around the analysis frequency of 1 MHz.	26
2.6	The temporal quantum noise reduction characterization σ as a function of the time interval δt between successive images for different beams of light. Green squares: twin beams; blue dots: coherent beams; black triangles: probe beam only; red triangles: conjugate beam only.	28
3.1	Theoretical decoherence characterization of the TMSV state via its SHG signal. To isolate the effect of decoherence on the quantum correlation $\langle \hat{a}\hat{b} \rangle$, experiment is performed by holding power p constant, i.e., $p \equiv p_0$	36

3.2	(a) Experimental setup in which a CW laser-pumped ^{85}Rb vapor cell produces a TMSV state via the FWM process. The TMSV beam (i.e. the ‘light cone’) is separated from the pump beam by a $\sim 2 \times 10^5 : 1$ polarizing beam splitter after the cell. The SHG signal from the BBO crystal is collected by an EMCCD camera. Two low-pass filters are mounted in front of the camera to eliminate undesired excitation photons. The BBO crystal and the EMCCD camera are enclosed in a light-proofing box to block ambient light. PBS: polarizing beam splitter, ND: neutral density filter, LP: low-pass filter. (b) Level structure of the D1 transition of ^{85}Rb atom. The optical transitions are arranged in a double- Λ configuration, where ν_p, ν_c and ν_1 stand for probe, conjugate and pump frequencies, respectively, fulfilling $\nu_p + \nu_c = 2\nu_1$ and $\nu_c - \nu_p = 2\nu_{\text{HF}}$. The width of the excited state in the level diagram represents the Doppler broadened line. Δ is the one-photon detuning. ν_{HF} is the hyperfine splitting in the electronic ground state of ^{85}Rb . (c) Image of the cross-section of the TMSV state, i.e., the ‘light cone’, where the bright central spot is the residual pump beam.	39
3.3	TMSV beam (light cone) power as a function of pump power. Dashed line is the theoretical fit according to Eq. (3.8) with $r \equiv \alpha P$, where P is the pump power.	41
3.4	SHG signal as a function of the TMSV beam (light cone) power. Dashed line is a polynomial fit according to Eq. (3.17) with $\text{ND} = 0$	42
3.5	SHG signals induced by $80 \mu\text{W}$ partially-decoherent TMSV beams of light (blue dots, left-hand side y -axis) and $80 \mu\text{W}$ coherent beams of light (red dots, right-hand side y -axis) as a function of transmission of ND filters. Dashed blue line is the theoretical fit according to Eq. (3.17).	44
4.1	Theoretical prediction for the quantum advantage (Qu. Adv.) for absorption $\alpha = 5\%$ as a function of optical transmission in the probe beam path η_p and conjugate beam path η_c . The squeezing parameter $r = 1.1$ corresponds to 6.5 dB two-mode squeezing.	51

4.2	<p>(a) Experimental setup in which a seeded ^{85}Rb vapor cell produces strong quantum-correlated twin beams via FWM. The twin beams are separated from the pump by a $\sim 2 \times 10^5 : 1$ polarizer after the cell. The probe beam passes through an absorption ‘sample’ (i.e., a combination of a $\lambda/2$ plate and a PBS) while the conjugate beam serves as a reference, before they are focused onto an EMCCD camera. The camera is enclosed in a light-proof box with filters mounted to block ambient light. The AOM in the probe beam path is used to pulse the twin beams with $2 \mu\text{s}$ FWHM and duty cycle of $1/12$. PBS: polarizing beam splitter, PM fiber: polarization-maintaining fiber. (b) Level structure of the D1 transition of ^{85}Rb atom. The optical transitions are arranged in a double-Λ configuration, where ν_p, ν_c and ν_1 stand for probe, conjugate and pump frequencies, respectively, fulfilling $\nu_p + \nu_c = 2\nu_1$. The width of the excited state in the level diagram represents the Doppler broadened line. Δ is the one-photon detuning, δ is the two-photon detuning, and ν_{HF} is the hyperfine splitting in the electronic ground state of ^{85}Rb. (c) Measured intensity-difference noise power spectrum for the squeezed twin beams (blue line) and for the SNL (red line), obtained with a radio frequency spectrum analyzer (with resolution and video bandwidth of 300 kHz and 100 Hz, respectively). A squeezing of 6.5 dB is achieved.</p>	52
4.3	<p>(a) Time sequencing of the pump and twin beams. The pulse duration of $2 \mu\text{s}$ and duty cycle of $1/12$ is realized by pulsing the probe beam with an AOM. The CW pump beam is present all the time. (b) Typical images of the twin beams with absorption $\alpha = 3 \%$ captured by the EMCCD camera. This subfigure is the ‘real life’ version of subfigure (a). It is an image of four consecutive pulses with the pulse width and duty cycle shown in subfigure (a). (c) Temporal photon counts fluctuations of the probe $N_p(t)$ and conjugate $N_c(t)$ obtained by integrating the photon counts in the cropped regions in (b). Clear similarities can be observed between the twin beams. (d) The strong noise reduction in the subtraction as opposed to the summation of the $N_p(t)$ and $N_c(t)$ depicted in (c) showcases strong correlations between them.</p>	54
4.4	<p>Actual absorption α as a function of the measurement signal S_α defined in Eq. (4.4). The inset is a zoom-in view of the first four data points to illustrate the sizes of x and y uncertainties.</p>	57
4.5	<p>Temporal quantum noise reduction σ as a function of absorption α for the bright squeezed light (blue squares) and coherent light (red dots). Dashed blue line is the theoretical prediction with $\eta_p = 0.61$, $\eta_c = 0.63$ and $r = 1.1$.</p>	59
4.6	<p>Quantum advantage as a function of absorption α. Dashed blue line is the theoretical prediction with $\eta_p = 0.61$, $\eta_c = 0.63$ and $r = 1.1$. The quantum advantage is only significant (> 1 dB) for small values of α ($< 20 \%$), and for $\alpha > 60 \%$ there is no quantum advantage.</p>	61

5.1	Absorption spectra for coherent light (solid line), light with squeezed-phase fluctuations (dashed line), and light with squeezed-amplitude fluctuations (dash-dotted line) [158]. The parameters chosen are $\Gamma = 0.1\gamma$, $2\epsilon/\gamma = 0.2$, and $I_c = 5 * I_{sqz}$	70
5.2	(a) Squeezed-light TPA setup in which a seeded ^{85}Rb cell produces strong quantum-correlated twin beams via FWM. The twin beams are focused onto the sample with a $10\times$ objective. Fluorescence is collected at an angle of 90° with a second $10\times$ objective and fed into a photomultiplier tube (PMT). Two short-pass filters in front of the PMT exclude stray pump photons. The setup is enclosed in a light-proof box. (b) Level structure of the D1 transition of ^{85}Rb atoms. The optical transitions are arranged in a double- Λ configuration, where ν_p , ν_c and ν_1 stand for probe, conjugate and pump frequencies, respectively, fulfilling $\nu_p + \nu_c = 2\nu_1$. The width of the excited state in the level diagram represents the Doppler broadened line. Δ is the one-photon detuning, δ is the two-photon detuning, and ν_{HF} is the hyperfine splitting in the electronic ground state of ^{85}Rb . (c) Measured intensity-difference noise power spectrum for the squeezed twin beams (blue line) and for the standard quantum limit (red line), obtained with a radio frequency spectrum analyzer (with a resolution and video bandwidth of 300 kHz and 100 Hz, respectively). A squeezing of 6.5 dB is achieved. (d) Molecular structures of DCM and fluorescein.	72
5.3	Fluorescence rates versus excitation power. The red diamonds and the red (dash-dotted) line show the measured values for the coherent excitation and the respective quadratic fit. The green stars are the rates for SL-TPA induced by the twin-beam excitations, and the green (dash-dotted) line is the respective linear fit. Error bars denoting one standard deviation, and enhancement of a factor of ~ 50 with squeezed light at 8 mW. The fluorescence signal from 4 mW of squeezed light excitation is also shown. Inset: raw voltage output from the PMT for coherent light (red) and squeezed light (green) excitations of 8 mW optical power. The shaded area for each curve represents one standard deviation.	75
5.4	Fluorescence rates for 8 mW SL-TPA with three different two-photon detunings δ , shown in the atomic level structure in Fig. 5.2(b) as δ . Red, green and blue bars are for $\delta = -10$ MHz, -5 MHz and 0 MHz, respectively. This figure demonstrates degraded SL-TPA enhancements as a function of the relative arrival times of the entangled photon pairs.	78
5.5	Fluorescence signal of DCM versus excitation power of coherent light (red) and squeezed light (green). Coherent light fitting curve obeys a quadratic behavior, while squeezed light fitting curve shows a polynomial behavior, indicating a high input of entangled photon-pair flux.	80
5.6	Typical photomultiplier voltage divider circuit using negative high voltage, image from wikipedia websit.	82
5.7	The PMT voltage raw data of fluorescence signal from DCM. The time-step of two continue data point is 0.25 ns, and $7 * 10^6$ points are collected by a oscilloscope.	83

5.8	The post-processed PMT voltage raw data of fluorescence signal from DCM.	83
6.1	Color online. The experimental setup. (a) The laser incident on a rotating ground glass (GG) generates speckled light. The light transmitting through the mask (M) and iris is collected by the camera (CMOS) with a lens (L) $f=150\text{mm}$. Here, distance $d' = d = 300\text{mm}$. (b) Several image frames are recorded to compute the high order correlation images. (c) A pixel's temporal intensity fluctuation. (d) The mask object, notably four dots. (e) Laser illumination intensity (Int.) imaging without Ground Glass (GG), for which the image of the four dots is blurred since the Rayleigh limit is twice the distance of the dot separation.	87
6.2	Color online. The speckle pattern coherence length $l_c \propto 24\mu\text{m}$. The target object is removed, and multi-frames images are measured, see (a). The correlations of the intensity fluctuation $\langle \delta I(\rho'_1) \delta I(\rho'_2) \rangle$ are calculated, see (b)	90
6.3	Color online. Comparison of traditional intensity imaging and high order moment imaging. (a) The average intensity (Avg.) imaging of speckle illumination, and the images reconstructed by the 2^{nd} , 9^{th} , 12^{th} , 20^{th} and 25^{th} order central moment (b, c, d, e, f). (g) The contrast comparison from images of different orders by summing two rows of pixels that are centered with the holes. (h) The visibility and standard deviation as a function of the moment orders computed by using the different frame numbers.	92
6.4	Color online. Comparison of cumulant and moment imaging. (a) The 2^{nd} order central moment μ_2 image. Since the ratio of the Raleigh limit to dots separation is $50/25 = 2$, which is larger than the resolution improvement $\sqrt{2}$ that μ_2 yields, the image is blurred. (b, c) for 6^{th} order moment and cumulant image, respectively. (d) The contrast comparison of different order images by taking two rows of pixels that are centered with the holes, and (e) the visibility and standard deviation of moment versus cumulant with 50 000 frames.....	94
6.5	(a) A laser beam illuminates on a random medium which move at velocity V with direction labeled, and a time varying speckle pattern is generated as result of interference of scattered light. The result of 6^{th} order cumulant imaging (b).	96
6.6	(a) The conventional microscopy leaf cell imaging with white illumination, and cell image is a stable imaging. The flower and leaf image (b).	96
6.7	The second order correlation imaging of time varying speckle pattern, which clearly shows the water moving region and moving intensity (a), and its zoom imaging result (b).	97
7.1	Stimulated Brillouin scattering(SBS) setup, where sample is illuminated by a strong pump field to enhance the signal.	103

7.2 Stimulated Brillouin scattering(SBS) setup with squeezed light, where sample is illuminated by a strong pump beam and a probe beam. The correlation detection between the output of probe beam and conjugate beam will suppress the noise, therefore, gives us better result than any classical approaches. 104

1. INTRODUCTION AND LITERATURE REVIEW

In the last two decades, numerous discoveries have established that quantum ideas will pave the way for a wide range of applications in the next generation of quantum technologies and quantum communications. The basis for many of these applications revolves around quantum coherence, quantum entanglement and quantum interference. These quantum ideas can provide us with methodologies to achieve unprecedented sensitivity and resolution for sensing and imaging [1–6], which is far beyond the classical measurement could achieve. These new methods based on quantum physics are revolutionizing the scales at which one can do sensing, imaging and microscopy with applications in diverse fields from physics and engineering to chemical, biology and medicine. The quantum sensing has clear bearing on many future technologies.

Even the most advanced classical sensors are bounded by a hard limit in precision—the standard quantum limit (SQL) [7–9] that arises from statistical fluctuations. In a conventional (classical) optical interferometer the precision with which an unknown optical phase ϕ can be measured is limited to $\delta\phi = 1/\sqrt{N}$, where N is the average number of photons used to probe. The measurement of optical phase is extremely useful in metrology due to the fact that many other quantities can be subsequently inferred, such as the change of index of refraction, the change of displacement and the change of concentration, etc. In order to acquire a better phase sensitivity, increasing N is usually possible, by increasing laser power for example. However, in some scenarios, the practical limits of laser power are reached and increasing the integration time will reduce the bandwidth of the measurement below that is required. In other scenarios, the object to be measured may be sensitive to light, such that one would like to minimize the photon flux or total number of photons that the object is exposed to in order to reach the required precision. By integrating a quantum light source into an interferometric configuration, the SQL can be overcome - quantum metrology enables the more fundamental Heisenberg limit of precision, $\delta\phi = 1/N$, to be reached [10–12].

One of important issues in quantum sensing is the sensitivity of measurement. The sensitivity is measured by how much we go below the standard quantum limit (SQL). By using the non-

linear interaction between light and atoms, a quantum feature known as squeezed light can be produced. This particular quantum state of light has great potential in sensing far beyond classical limit. Such a hypersensitive optical sensing scheme can be utilized for ultra-sensitive measurements of phase, displacements and extremely weak absorption in systems ranging from physics to biology. Quantum light is especially useful for this purpose, both two-mode squeezed light and entangled photon pairs are great sources of producing supersensitivity in metrology. Using the entangled photon pairs and the two-mode squeezed light, some of recent experiments have demonstrated roughly 50% to 70% improvement in the sensitivity beyond SQL.

In our lab, the quantum light source is a twin-beam squeezed light, which is generated via four-wave mixing nonlinear processes in a ^{85}Rb vapor cell, where interactions between two, or three fields produce two, or one new fields respectively. Our goal is to develop novel quantum sensing techniques by engineering quantum light sources and by improving the quantumness of these sources, so that they can be utilized in proof of principle applications as well as other related applications, such as the weak absorption measurement, decoherence investigation, and two-photon microscopy.

Thus, we will discuss the generation of twin-beam squeezed light based on the four-wave mixing in the first chapter.

1.1 Four-wave mixing

In classical model, the response of a material interacting with an external electric field, can be described with a power series in the electric field strength [13–15]

$$\vec{P} = \epsilon_0 \chi^{(1)} \vec{E} + \epsilon_0 \chi^{(2)} \vec{E} \vec{E} + \epsilon_0 \chi^{(3)} \vec{E} \vec{E} \vec{E} + \dots, \quad (1.1)$$

The $\chi^{(i>1)}$ is expansion coefficient, which is known as nonlinear susceptibilities, i.e. $\chi^{(3)}$ is a fourth rank tensor. As higher order nonlinear coefficient decreases progressively so that the power series converges to a finite value.

The four-wave mixing (4WM) processes is from the third order nonlinear susceptibility $\chi^{(3)}$.

To have a better understanding on 4WM process, we do a closer examination of the third order nonlinear polarization $P_i^{(3)}$, and its form of the polarization is rewritten as

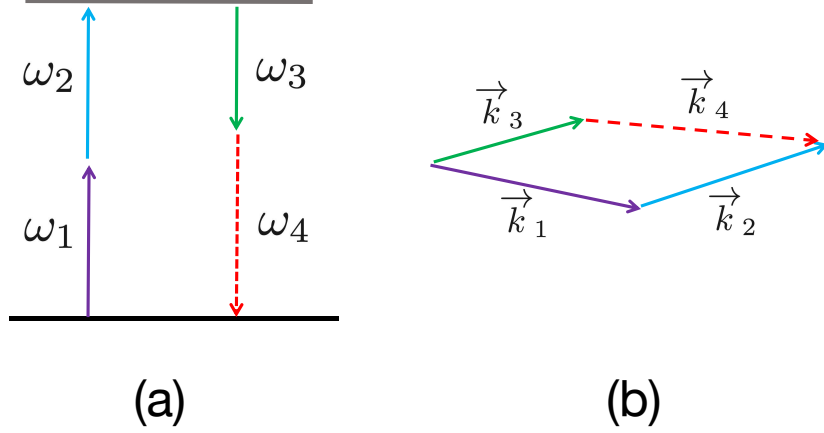


Figure 1.1: Energy (a) and momentum (b) conservation in the 4WM, where $\omega_1, \omega_2, \omega_3, \omega_4$ are three angular frequencies of input fields, and $\vec{k}_1, \vec{k}_2, \vec{k}_3$ are three wave vectors. The relation between wave vectors k_i and angular frequencies ω_i are given by $k_i = n_i \omega_i / c$.

$$\begin{aligned}
 P_i^{(3)}(\omega_4, \vec{r}) &= \frac{1}{2} \epsilon_0 \chi_{ijkl}^{(3)}(\omega_1, \omega_2, -\omega_3) E_j E_k E_l^* \cdot \\
 &\quad \exp \left[i \left(\vec{k}_1 + \vec{k}_2 - \vec{k}_3 \right) \cdot \vec{r} - (\omega_1 + \omega_2 - \omega_3) t \right] + c.c. \\
 &= \frac{1}{2} \epsilon_0 \chi_{ijkl}^{(3)}(\omega_1, \omega_2, -\omega_3) E_j E_k E_l^* \cdot \exp \left[i \vec{k}_4 \cdot \vec{r} - \omega_4 t \right] + c.c. \quad (1.2)
 \end{aligned}$$

The relation of angular frequencies and wave vectors between input and output fields reads,

$$\omega_4 = \omega_1 + \omega_2 - \omega_3 \quad (1.3)$$

$$\vec{k}_4 = \vec{k}_1 + \vec{k}_2 - \vec{k}_3 \quad (1.4)$$

Equations (1.3,1.4) give us energy and momentum conservation [15], where ω_i are angular frequencies of fields, and \vec{k}_i are their wave vectors, and i, j, k, l present x, y and z electric field component. The dependence of wave vectors k_i and angular frequencies ω_i are given by $k_i = n_i \omega_i / c$, where n_i is the refraction index at frequency ω_i .

This third order non-linearity processing describes a interaction between four waves: three input fields, $\omega_{1,2,3}$, and the fourth generated field ω_4 . For those four fields, their propagation direction, polarization and frequency are given by k_i , E_i and ω_i . Experimentally, we know that, measurable quantity is the field intensity, $|E|^2$, not amplitude E , and its measured intensity is proportional to $|\chi^{(3)}|^2$. The amplitude of generated output field with frequency ω_4 is a superposition of emission fields, that are generated from each atom via 4WM processes. Thus, we have the generated filed reads

$$E_i(\omega_4, \vec{r}') = \int G(\vec{r}', \vec{r}) E_i(\omega_4, \vec{r}) d\vec{r}, \quad (1.5)$$

where $G(\vec{r}')$ is the Fresnel propagator with \vec{r}' on the observation plan, and the integration is over the whole 4WM interacting volume.

So, Equation (1.2,1.5) also implies that effective 4WM between the four waves only occur when energy and momentum are both conserved, which results constructive interference., where $\omega_1 + \omega_2 - \omega_3 - \omega_4 = 0$ and $\vec{k}_1 + \vec{k}_2 - \vec{k}_3 - \vec{k}_4 = 0$. Otherwise, the random phase $\exp \left[i \left(\vec{k}_1 + \vec{k}_2 - \vec{k}_3 \right) \cdot \vec{r}' \right]$ will terminate the 4WM processing. The “phase mismatching” factor is given by

$$\vec{\delta k} = \vec{k}_1 + \vec{k}_2 - \vec{k}_3 - \vec{k}_4 \quad (1.6)$$

The “perfect phase matching” condition is $\vec{\delta k} = 0$. In Fig. 1.1, we show the satisfaction of these two conditions schematically.

In our experiment, we are focus on the phase-insensitive amplification, in which the 4WM processes are generated via a double- Λ energy level configuration. Our result shows that the 4WM

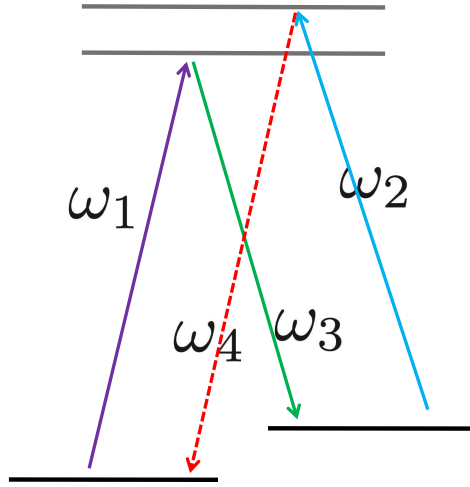


Figure 1.2: 4-level double- Λ atomic configuration.

based on the double- Λ scheme can be used to generate a squeezed light, i.e., two beams with their intensity difference fluctuation smaller than the shot-noise which is defined with coherent light.

1.2 Phase-insensitive amplifier

Based on 4WM process in sodium vapor, its first quantum squeezing light was demonstrated about 30 years ago [16]. After that, different squeezing mechanisms in vapor have been proposed and experimentally demonstrated [17–23]. Recent investigations show us that 4WM in an atomic vapor can be used to generate an effective and reliable source of squeezed light and continuous-variable entanglement [24–29].

The sketch of 4WM-based PIA scheme in an atomic vapor is shown in Fig 1.3, where a small angle between probe and pump crossed in an atomic vapor is for momentum conservation. The energy diagram tells us that two photons from a strong pump field are converted into a pair of photons, probe and conjugate, which are spatially separated with a small angle around 0.3 degree because of the momentum conservation (see the energy diagram in Fig. 1.3). The 4WM process will amplify the probe beam with a gain factor G , which is defined by $G = \frac{I_{out}}{I_{in}}$ where I_{out} and

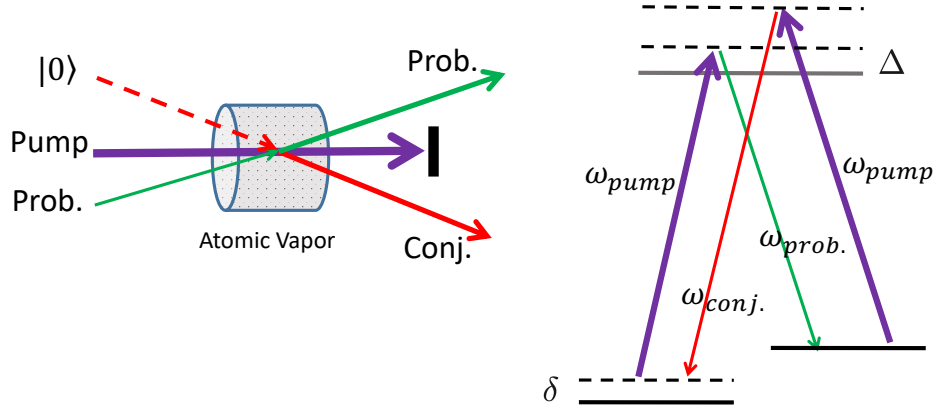


Figure 1.3: Experiment sketch and atomic energy diagram for PIA, where a very strong pump beam is used to drive the 4WM running. One port is seeded with a probe beam, and another is seeded with a vacuum state. Due to the 4WM interactions, an amplified probe beam and a new generated conjugate beam are emitted, where Δ and δ present the one- and two-photon detuning, respectively.

I_{in} are input and output intensity of probe beam. Meanwhile, we have the conjugate intensity $(G - 1) * I_{in}$, which generated from vacuum state. This amplification process is independent of the phase of the input probe field, so we call it phase insensitive amplification (PIA).

This squeezed light generation scheme based on 4WM has been extensively investigated and implemented in atomic-based quantum sensing, and quantum memories, such as in weak absorption measurement and an optically tunable delay for entangled beams of light with Einstein-Podolsky-Rosen(EPR) levels of entanglement [26], the generation of high-purity narrowband single photons [30] and the realization of an SU(1,1) quantum interferometer with high phase sensitivity [31, 32].

In our lab, the quantum light source is a twin-beam squeezed light, which is generated via four-wave mixing nonlinear processes in a ^{85}Rb vapor cell, where interactions between two, or three fields produce two, or one new fields respectively. Our goal is to develop novel quantum sensing techniques by engineering quantum light sources and by improving the quantumness of these

sources, so that they can be utilized in proof of principle applications as well as other related applications, such as the weak absorption measurement, decoherence investigation, and two-photon microscopy.

For a better understanding about squeezed light generation, we will give its quantum mechanical model expression, see the next section below.

1.3 Quantum mechanics for linear optical amplifiers

A linear optical amplifier is defined by a linear dependence between its outputs and its inputs, which was described in [33]. As there may more than one input fields, so a linear amplifier can be a phase insensitive amplifier (PIA) or phase sensitive amplifier (PSA). For a former amplifier, its gain and noise are independent of the phase of the input light, and inevitably adds extra noise to the input signal, while with the latter one, it is possible to noiselessly amplify an input signal. We will provide a simple quantum-mechanical model that based on 4WM processing, and derive the amplifier linear dependence, noise properties of the PIA. Under the quantum-mechanical model, we will have a clear physical picture that what is the squeezed parameter, and how it will be used in quantum sensing.

Our 4WM is based on a double- Λ configuration, see Fig. 1.4. As we know 4WM process involves three modes; probe, conjugate and pump, and its creation operator reads \hat{a} , \hat{b} and \hat{c} , respectively. This process is a loop interaction that annihilates a pump photon and creates a probe photon, annihilates second pump photon and then creates a conjugate photon; or vice versa. So, the we could get its interaction Hamiltonian [34, 35], which reads

$$H_I = i\hbar\chi\hat{c}^2\hat{a}^\dagger\hat{b}^\dagger + h.c. \quad (1.7)$$

with the effective interaction strength χ which depends on the third-order nonlinear susceptibility $\chi^{(3)}$ and the interaction length L in the vapor. To drive the 4WM, a very strong pump is used in experiment, therefor, the pump mode \hat{c} will be replace with classical. parameter. So, the

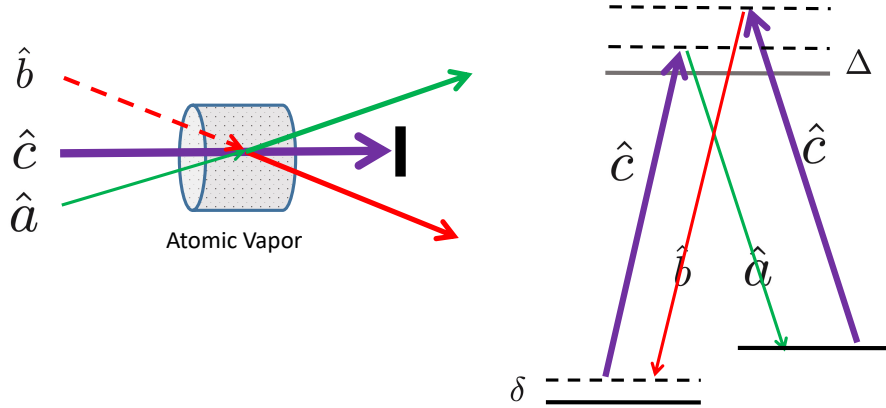


Figure 1.4: (a) Experiment realization and atomic energy diagram represented with operators. One port is seeded with a probe beam, and another is seeded with a vacuum state. Three inputs are crossed at the center of the atomic vapor with a small relative angle to fulfill the phase matching condition. (b) The atomic level scheme, two ground states and one excited state with three input modes a, b and c, where Δ and δ present the one- and two-photon detuning, respectively.

interaction Hamiltonian in Eq. 1.7 can then be rewritten as:

$$H_I = i\hbar\xi e^{i\theta} a^\dagger b^\dagger + h.c. \quad (1.8)$$

Without loss of generality, the $\theta = 2\phi_c$ with ϕ_c the phase of pump field, and ξ is the strength of interaction that depends on 1) the third-order nonlinear susceptibility, 2) the path length of the interaction and 3) the intensity of the pump. In atomic system, the third-order nonlinear susceptibility ξ is a function of Δ and δ as well, see Fig. 1.4.

In the interaction picture, the time evolution equation is given by

$$\frac{d\hat{O}}{dt} = \frac{1}{i\hbar} [\hat{O}, \hat{H}_I], \quad (1.9)$$

We can obtain the time evolution for operators \hat{a} and \hat{b}^\dagger :

$$\frac{d\hat{a}}{dt} = \xi e^{i\theta} \hat{b}^\dagger \quad (1.10)$$

$$\frac{d\hat{b}^\dagger}{dt} = \xi e^{-i\theta} \hat{a} \quad (1.11)$$

Solve above differential equations, we have the operators read

$$\hat{a}(t) = \cosh(\xi t) \hat{a} + e^{i\theta} \sinh(\xi t) \hat{b}^\dagger \quad (1.12)$$

$$\hat{b}^\dagger(t) = \cosh(\xi t) \hat{b}^\dagger + e^{-i\theta} \sinh(\xi t) \hat{a} \quad (1.13)$$

with $r = \xi t$, where t is the interaction time, which depends on the path length L with relation $t = L/v_g$, where v_g is the group velocity. The output operator are

$$\hat{a}_f = \cosh(r) \hat{a} + e^{i\theta} \sinh(r) \hat{b}^\dagger \quad (1.14)$$

$$\hat{b}_f^\dagger = \cosh(r) \hat{b}^\dagger + e^{-i\theta} \sinh(r) \hat{a} \quad (1.15)$$

The PIA experimental realization is sketched in Fig.1.4, where the probe input is seeded with a coherent field and the conjugate input is seeded with vacuum state. To fulfill the phase matching condition, those inputs are crossed in an atomic vapor with a relatively small angle, see Fig.1.1.

In this 4WM process, let's seed the probe port with a coherent state input $|\alpha_a\rangle$, and seed conjugate port by a vacuum state. So, we have the input state reads $|\alpha_a, 0_b\rangle$. It is not difficult to get the mean output photon number $\langle \hat{n}_{a,b} \rangle$ and its photon-number variance $\Delta \hat{n}_{a,b}^2 = \langle \hat{n}_{a,b}^2 \rangle - \langle \hat{n}_{a,b} \rangle^2$.

Here we notate \hat{a}_f^\dagger to be signal beam and \hat{b}_f^\dagger to be conjugate beam. For the input field $|\alpha_a, 0_b\rangle$, the mean output photon number and photon-number variance of the conjugate beam are given by

$$\begin{aligned}
\langle \hat{n}_b \rangle &= \sinh^2(r) \langle 0, \alpha | \hat{a}^\dagger \hat{a} | \alpha, 0 \rangle \\
&= (|\alpha|^2 + 1) \sinh^2(r)
\end{aligned} \tag{1.16}$$

$$\Delta \hat{n}_b^2 = \frac{1}{2} [1 + (1 + 2|\alpha|^2) \cosh 2r] \sinh^2 r \tag{1.17}$$

The same with the probe beam, its mean output photon number and photon-number variance read

$$\begin{aligned}
\langle \hat{n}_a \rangle &= \cosh^2(r) \langle 0, \alpha | \hat{a}^\dagger \hat{a} | \alpha, 0 \rangle + \sinh^2(r) \langle 0, \alpha | bb^\dagger | \alpha, 0 \rangle \\
&= |\alpha|^2 \cosh^2(r) + \sinh^2(r)
\end{aligned} \tag{1.18}$$

$$\Delta \hat{n}_a^2 = \frac{1}{2} [-1 + (1 + 2|\alpha|^2) \cosh 2r] \cosh^2 r \tag{1.19}$$

It is clear that there is no input phase ϕ_i dependence either in the gain or in the noise expression.

If we define $G_{PIA} = \cosh^2 r$ and assume an input coherent state that is sufficiently bright, e.g. $|\alpha_a|^2 \gg 1$, above equations could be simplified to

$$\langle \hat{n}_a \rangle = |\alpha|^2 \cosh^2 r = G_{PIA} \langle \hat{n}_{in} \rangle \tag{1.20}$$

$$\Delta \hat{n}_a^2 = |\alpha|^2 \cosh^2 r \cosh 2r = G_{PIA} (2G_{PIA} - 1) \Delta \hat{n}_{in}^2 \quad (1.21)$$

$$\langle \hat{n}_b \rangle = |\alpha|^2 \sinh^2 r = (G_{PIA} - 1) \langle \hat{n}_{in} \rangle \quad (1.22)$$

$$\Delta \hat{n}_a^2 = |\alpha|^2 \sinh^2 r \cosh 2r = (G_{PIA} - 1) (2G_{PIA} - 1) \Delta \hat{n}_{in}^2 \quad (1.23)$$

Since for a coherent state input seeding mode a, $\Delta \hat{n}_{in}^2 = \langle \hat{n}_{in} \rangle = |\alpha|^2$. It is clear that there is no input phase ϕ_i dependence either in the gain or in the noise expression. In the quantum optics community, we would like to call the output probe and conjugate \hat{a} and \hat{b} “twin beams”.

To characterize the correlation of each beam, we also calculated its $g^{(2)}$ value, which reads

The $g_b^{(2)}$ for conjugate beam

$$g_b^{(2)} = \frac{\langle \hat{b}_f^\dagger \hat{b}_f^\dagger \hat{b}_f \hat{b}_f \rangle}{\langle \hat{b}_f^\dagger \hat{b}_f \rangle^2} = 1 + \frac{1}{|\alpha|^2 + 1} \quad (1.24)$$

$$\xrightarrow{|\alpha| \gg 1} 1 \quad (1.25)$$

$$\xrightarrow{|\alpha| \leq 1} 2 \quad (1.26)$$

The $g_a^{(2)}$ for signal beam

$$g_a^{(2)} = \frac{\langle \hat{a}_f^\dagger \hat{a}_f^\dagger \hat{a}_f \hat{a}_f \rangle}{\langle \hat{a}_f^\dagger \hat{a}_f \rangle^2} = 1 + \frac{\sinh^4(r) + 2|\alpha|^2 \cosh^2(r) \sinh^2(r)}{(\sinh^2(r) + \cosh^2(r) |\alpha|^2)^2} \quad (1.27)$$

$$\xrightarrow{|\alpha| \gg 1} 1 \quad (1.28)$$

$$\xrightarrow{|\alpha| \leq 1} 2 \quad (1.29)$$

Note that $g^{(2)}$ of each beam is the same with coherent $g^{(2)}$ value, which equals to 1, when the input probe state is a bright coherent light with $|\alpha| \gg 1$. If the input probe state is a vacuum state, the each output beam is a two-mode squeezed vacuum, which displays a thermal state behavior with $g^{(2)} = 2$.

1.3.1 Correlation between two-modes squeezed vacuum

For a coherent probe input, we have discussed the average photon number $\langle \hat{n} \rangle$, its fluctuations $\langle \Delta^2 \hat{n} \rangle$ and $g^{(2)}$ for each mode.

In this subsection, we are interested in two-modes squeezed vacuum, where input probe state is a vacuum state, not a coherent state. The generated two-mode squeezed states is given by

$$|re^{i\theta}\rangle = S(re^{i\theta}) |0, 0\rangle \quad (1.30)$$

where $S(re^{i\theta}) = \exp(re^{i\theta} \hat{a}^\dagger \hat{b}^\dagger - re^{-i\theta} \hat{a} \hat{b})$. In the photon-number representation, the explicit result reads

$$|re^{i\theta}\rangle = \frac{1}{\cosh r} \sum_{n=0}^{\infty} e^{in\theta} (\tanh r)^n |n n\rangle \quad (1.31)$$

Note that if mode \hat{a} has n-photons, then mode \hat{b} must have n-photons, this property also indicates the correlation between mode \hat{a} and \hat{b} . Meanwhile, we also could get the properties,

$$\langle \hat{a}^2 \rangle = \langle \hat{b}^2 \rangle = 0 \quad (1.32)$$

$$\langle \hat{a} \rangle = \langle \hat{b} \rangle = 0 \quad (1.33)$$

We also found that the state $|re^{i\theta}\rangle$ cannot be rewritten as a factorized product of the states for the individual modes.

$$|re^{i\theta}\rangle \neq |\psi_a\rangle |\psi_b\rangle. \quad (1.34)$$

Such a state is called an entangled state, and its entanglement depends on the squeeze parameter r .

The quantum correlation also can be characterized by $|\langle \hat{a}\hat{b} \rangle|$.

$$\langle \hat{a}\hat{b} \rangle = \cosh r \sinh r e^{i\theta} \quad (1.35)$$

$$\langle \hat{a}^\dagger \hat{b} \rangle = 0. \quad (1.36)$$

In chapter 3, we will have more discussing, and show that such correlation $\langle ab \rangle$ can directly extract via second order correlation $\langle \hat{a}^\dagger \hat{a} \hat{b}^\dagger \hat{b} \rangle$, which reads

$$\begin{aligned} \langle \hat{a}^\dagger \hat{a} \hat{b}^\dagger \hat{b} \rangle &= \langle \hat{a}^\dagger \hat{a} \rangle \langle \hat{b}^\dagger \hat{b} \rangle + |\langle \hat{a}\hat{b} \rangle|^2 \\ &= \sinh^2 r \times \cosh^2 r + \sinh^4 r, \end{aligned} \quad (1.37)$$

the phase-sensitive correlation $|\langle \hat{a}\hat{b} \rangle|$ has the value of $\sinh r \times \cosh r$ and satisfies the equality sign. The decoherence of the intensity-intensity correlation $G_{ab}^{(2)}$ between the two modes is therefore given by

$$G_{ab}^{(2)} = \langle \hat{a}^\dagger \hat{a} \hat{b}^\dagger \hat{b} \rangle_t = \beta^2 (\sinh^2 r \times \cosh^2 r + \sinh^4 r). \quad (1.38)$$

The correlation of E.q.(1.38) will be further discussed and investigated in chapter 4, both theoretically and experimentally.

1.3.2 Intensity difference of Two-modes squeezed state

A state is squeezed, by definition, if any of its quadrature whose standard deviation that falls below the coherent-state value. In another word, we defined the coherent state to be the boundary between classical state and squeezed state.

As we know, after the linear amplification, the noise of each mode (\hat{a} or \hat{b}) is also amplified, so they are not a squeezed state independently. While, the noise of the intensity difference of twin beams is squeezed, which is given by

$$\hat{n}_{diff} = \hat{n}_a - \hat{n}_b = \hat{a}^\dagger \hat{a} - \hat{b}^\dagger \hat{b} \quad (1.39)$$

$$\Delta \hat{n}_{diff}^2 = \frac{1}{4} [(-1 + 3|\alpha|^2) + (1 + |\alpha|^2) \cosh 4r] - \frac{1}{2} (1 + |\alpha|^2) \sinh^2 2r \cos 4\phi_c \quad (1.40)$$

For simplicity and without the loss of generality, we set the pump phase $\phi_c = 0$, then the above expression is reduced to

$$\Delta \hat{n}_{diff}^2 = |\alpha|^2 \quad (1.41)$$

The shot noise level of the twin beams is just their summation,

$$\Delta \hat{n}_{snl}^2 = (\cosh^2 r + \sinh^2 r) |\alpha|^2 = (2G_{PIA} - 1) |\alpha|^2 \quad (1.42)$$

We define the two-mode intensity-difference squeezing in dB to be

$$SQZ_{diff} = 10 \log_{10} \left(\frac{\Delta \hat{n}_{diff}^2}{\Delta \hat{n}_{snl}^2} \right) = 10 \log_{10} \left(\frac{1}{2G_{PIA} - 1} \right) \quad (1.43)$$

In Fig. 1.5 we plot the two-mode intensity difference squeezing as a function of G_{PIA} . More squeezing can be achieved with greater PIA gain.

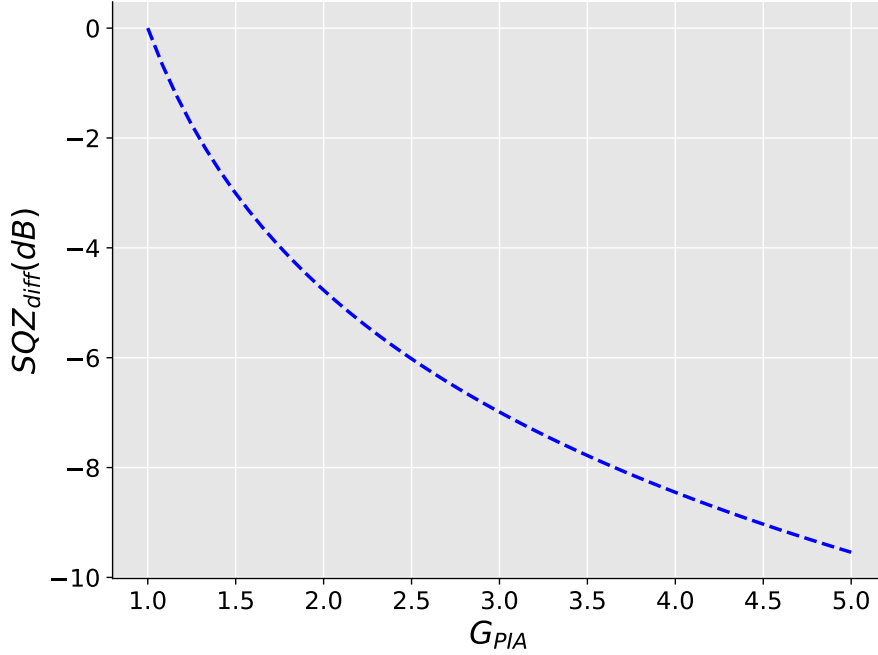


Figure 1.5: Two-mode intensity difference squeezing as a function of G_{PIA}

1.4 Outline

In this thesis, we utilize a PIA to prepare two-mode quantum correlations in the form of photon-number-difference squeezed optical beams, i.e., twin beams. We then report an important technical advance in the squeezed light arena, which allows one to use an EMCCD camera to achieve squeezing measurements in the temporal domain as well. We also investigated the decoherence

of a two-mode squeezed vacuum state via its second harmonic generation signal. With the twin beams squeezed light source, the direct absorption measurement was demonstrated with sensitivity beyond the shot-noise limit. The next utility of bright two-mode squeezed light source based on FWM is in ultra-low intensity TPA for biosensing and bioimaging, which provides a ~ 47 -fold enhancement for squeezed light compared to coherent light. The last chapter is devoted to the sub-Rayleigh imaging via high order correlation of speckle illumination.

In Chapter 2, we demonstrated that an electron-multiplying charge-coupled-device camera can be used to measure the temporal quantum noise of twin beams squeezed light. For the quantum noise reduction in the temporal domain, ‘bucket detectors,’ usually composed of photo-diodes with operational amplifiers, are used to register the intensity fluctuations in beams of light within the detectors’ bandwidth. Here, we report on measurements of the temporal quantum noise reduction in bright twin beams using an EMCCD camera. The temporal images captured by our technique are potentially important in obtaining dynamical information on evolving systems.

In Chapter 3, we report a novel experimental scheme on the study of decoherence of a two-mode squeezed vacuum state via its second harmonic generation signal. Our scheme can directly extract the decoherence of the phase-sensitive quantum correlation $\langle \hat{a}\hat{b} \rangle$ between two entangled modes \hat{a} and \hat{b} . Such a correlation is the most important characteristic of a two-mode squeezed state. More importantly, this is an experimental study on the decoherence effect of a squeezed vacuum state, which has been rarely investigated.

In Chapter 4, we use bright squeezed light to demonstrate that direct absorption measurement can be performed with sensitivity beyond the shot-noise limit. This is a direct sub-shot-noise measurement of absorption that requires neither homodyne/lock-in nor logic coincidence detection schemes. We present detailed theoretical analysis for the expected quantum advantage, and experimentally demonstrate the advantage of quantum light for measurements on open systems. Our results are similar to those reported for phase measurements.

In Chapter 5, we investigate two-photon absorption fluorescence rates in fluorescein biomarkers and in DCM laser dye, induced by a coherent CW excitation light and by the bright two-

mode squeezed light. For the coherent CW excitation both fluorophores show the well-expected quadratic dependence on the input photon flux. The experimental results for fluorescein with SL-TPA, however, demonstrate a linear dependence on the input optical power, along with a ~ 47 -fold TPA fluorescence enhancement for 8 mW squeezed light compared to 8 mW coherent light. This can be attributed to the predominant occurrence of entangled two-photon absorption of quantum-correlated photon pairs.

In Chapter 6, we implement an imaging scheme that goes beyond the sub-Rayleigh limit. We show that the object's true features can be recovered where a traditional diffraction-limited imaging method yields a completely blurred image. This is done by correlating photon counts at each pixel with two post-processing functions: moments and cumulants. In addition, and more importantly, we explore using cumulants, which, as demonstrated, show much more improvement as compared to moments.

Finally, Chapter 7 provides the summary and outlooks for possible future investigations.

2. TEMPORAL QUANTUM NOISE REDUCTION ACQUIRED BY AN ELECTRON-MULTIPLYING CHARGE-COUPLED-DEVICE CAMERA*

Electron-multiplying charge-coupled-device cameras (EMCCDs) have been used to observe quantum noise reductions in beams of light in the transverse spatial degree of freedom. For the quantum noise reduction in the temporal domain, ‘bucket detectors,’ usually composed of photodiodes with operational amplifiers, are used to register the intensity fluctuations in beams of light within the detectors’ bandwidth. Here, we report on measurements of the *temporal* quantum noise reduction in bright twin beams using an EMCCD camera. The four-wave mixing process in an atomic rubidium vapor cell is used to generate the bright twin beams of light. We observe $\sim 25\%$ of temporal quantum noise reduction with respect to the shot-noise limit in images captured by the EMCCD camera. Our technique could make it possible to take advantage of the spatial and temporal quantum properties of light simultaneously with an EMCCD camera, which would potentially benefit many applications using quantum states of light. The temporal images captured by our technique are potentially important in obtaining dynamical information on evolving systems.

2.1 Introduction

Quantum noise fluctuations in a beam of light below the shot-noise limit (SNL), i.e., squeezed light, was first observed in a groundbreaking experiment by Slusher *et al.* [37] using the process of four-wave-mixing (FWM) in an atomic vapor of sodium atoms. Since then squeezed light was implemented to enable enhanced communication rates [38–41] and improved detection of weak forces such as gravitational waves [42, 43]. The latter was demonstrated first at the GEO600 gravitational wave detector [44] and later at the LIGO detector [45]. These applications, although proposed more than three decades ago, are still some of the most prominent applications of squeezed light. In addition to these applications, squeezed states have also been shown to be the source

*Part of this chapter is reprinted from Ref. [36] (Fu Li, Tian Li and Girish S. Agarwal, "Temporal quantum noise reduction acquired by an electron-multiplying charge-coupled-device camera," *Opt. Express* 28, 37538-37545 (2020)) with permission from the The Optical Society (OSA).

of quantum teleportation [46, 47], continuous-variable quantum computing [48], quantum error correction coding [49, 50], phase estimation [51] and tracking [52], fundamental tests of quantum mechanics (such as the Einstein-Podolsky-Rosen gedanken experiment) [53–55], quantum imaging [56, 57] of e.g., biological samples [58], clock synchronization [59] and magnetometry [60, 61]. Moreover in recent years, a squeezed light source has been the work horse for quantum state engineering, in particular non-Gaussian state generation using the method of photon subtraction [62–65] as required for various quantum processing protocols [66–70].

It is interesting to note that the experimental platforms for generating squeezed light, such as nonlinear crystals, fibers and atomic ensembles used in the 80’s are still the same as those used today for generating much more efficient squeezing. Although significant advancements have been made from the initial 0.3 dB squeezing [37] till today’s near 15 dB squeezing [71], those advancements have mainly been of technical nature, i.e., successful development of low-noise electronics for phase locking, low loss optical components and high quantum efficiency photodiodes have led to largely improved systems.

Most of the aforementioned studies pertaining to squeezed light are in the temporal domain acquired by ‘bucket detectors’, i.e., photodiodes with operational amplifiers having sufficient bandwidth. Nevertheless, squeezed light can also be achieved in the transverse spatial degree of freedom using electron-multiplying charge-coupled-device cameras (EMCCDs) [72–75]. Here, we report yet another important technical advance in the squeezed light arena, which allows one to use an EMCCD camera to achieve squeezing measurements in the *temporal* domain as well. For imaging applications using EMCCDs temporal information usually has no relevance. However, for a large class of systems if one wants to study temporal effects, like motional effects - an example would be the Brownian motion of bacteria where one would like to find out motility. It is absolutely essential to have temporal images, and the wealth of information contained in the temporal images hardly needs to be emphasized. Our technique demonstrates the possibility of taking such temporal images in the quantum domain, which can be potentially applied in obtaining dynamical information on evolving systems.

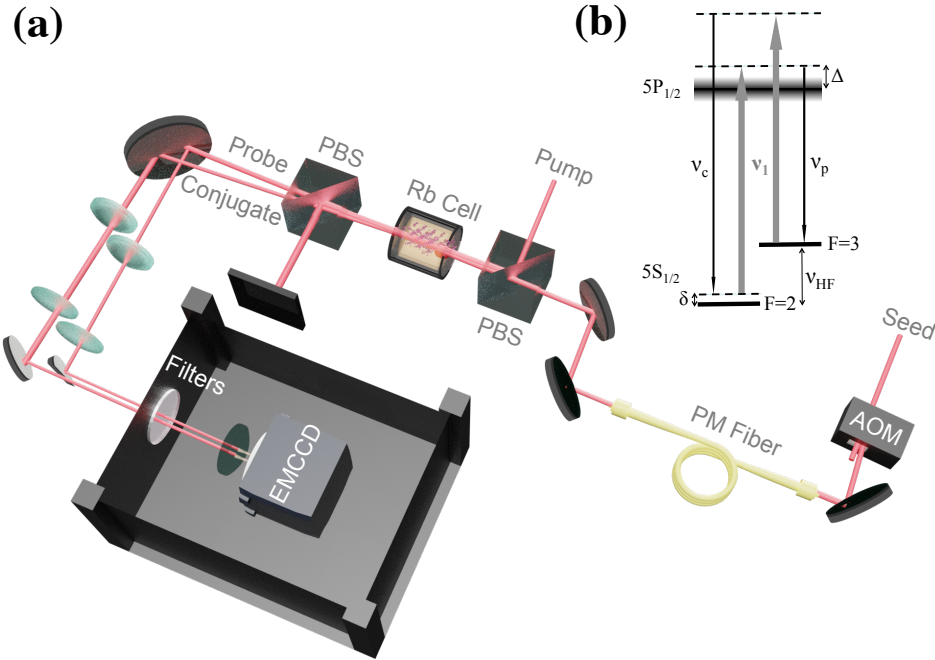


Figure 2.1: (a) Experimental setup in which a seeded ^{85}Rb vapor cell produces strong quantum-correlated twin beams via FWM. The twin beams are separated from the pump by a $2 \times 10^5 : 1$ polarizer and then focused onto the EMCCD camera. The camera is enclosed in a light-proof box with filters mounted to block ambient light. The AOM on the probe beam path is used to pulse the twin beams with $1 \mu\text{s}$ FWHM and duty cycle of $1/12$. PBS: polarizing beam splitter, PM fiber: polarization-maintaining fiber. (b) Level structure of the D1 transition of ^{85}Rb atom. The optical transitions are arranged in a double- Λ configuration, where ν_p , ν_c and ν_1 stand for probe, conjugate and pump frequencies, respectively, fulfilling $\nu_p + \nu_c = 2\nu_1$. The width of the excited state in the level diagram represents the Doppler broadened line. Δ is the one-photon detuning, δ is the two-photon detuning, and ν_{HF} is the hyperfine splitting in the electronic ground state of ^{85}Rb .

2.2 Experimental setup

The squeezed light generated in this work is based on the four-wave mixing (FWM) process in an atomic ^{85}Rb vapor cell [76–82]. The experimental setup and the respective atomic level structure are shown in Fig. 5.2(a) and (b). The medium possesses a large third-order electric susceptibility $\chi^{(3)}$ and is pumped by a strong (~ 500 mW) narrow-band continuous-wave (CW) laser at frequency ν_1 ($\lambda = 795$ nm) with a typical linewidth $\Delta\nu_1 \sim 100$ kHz. Applying an additional weak (~ 10 nW) coherent seed beam at frequency $\nu_p = \nu_1 - (\nu_{HF} + \delta)$, where ν_{HF} and δ are the hyperfine splitting in the electronic ground state of ^{85}Rb and the two-photon detuning respectively in Fig. 5.2(b) (further experimental details can be found in Ref. [83]), two pump photons are converted into a pair of twin photons, namely ‘probe ν_p ’ and ‘conjugate ν_c ’ photons, adhering to the energy conservation $2\nu_1 = \nu_p + \nu_c$ (see the level structure in Fig. 5.2(b)). The resulting ‘bright twin beams’ are strongly quantum-correlated and are also referred to as (seeded) two-mode squeezed light [84].

After the ^{85}Rb vapor cell, the pump and the bright twin beams are separated by a second polarizer, with $\sim 2 \times 10^5 : 1$ extinction ratio for the pump. The twin beams are then focused onto an EMCCD camera (Andor iXon Ultra 897). The EMCCD camera is enclosed in a light-proof box with filters installed at the entrance to block ambient light photons from entering the camera. The acousto-optic modulator (AOM) on the probe beam path is used to pulse the beam with $1 \mu\text{s}$ duration (FWHM) and duty cycle of $1/12$. Since the CW pump beam is present all the time, the conjugate beam is therefore also pulsed as a result of the FWM process. The time sequencing of the pump and the twin beams are shown in Fig. 4.3(a) as the red strap, and the blue and green squares respectively.

In the chapter 1, we have shown that the fluctuation of intensity difference of twin beams is squeezed. Here, we measured the fluctuation of intensity difference of two independent coherent, see Fig.2.4, where noise of coherent-1 is the same level with noise of coherent-2. The subtraction fluctuation of those two independent coherent beams is same with their summation. While Fig.2.3 shows that the subtraction fluctuation of probe and conjugate is below than their summation. The

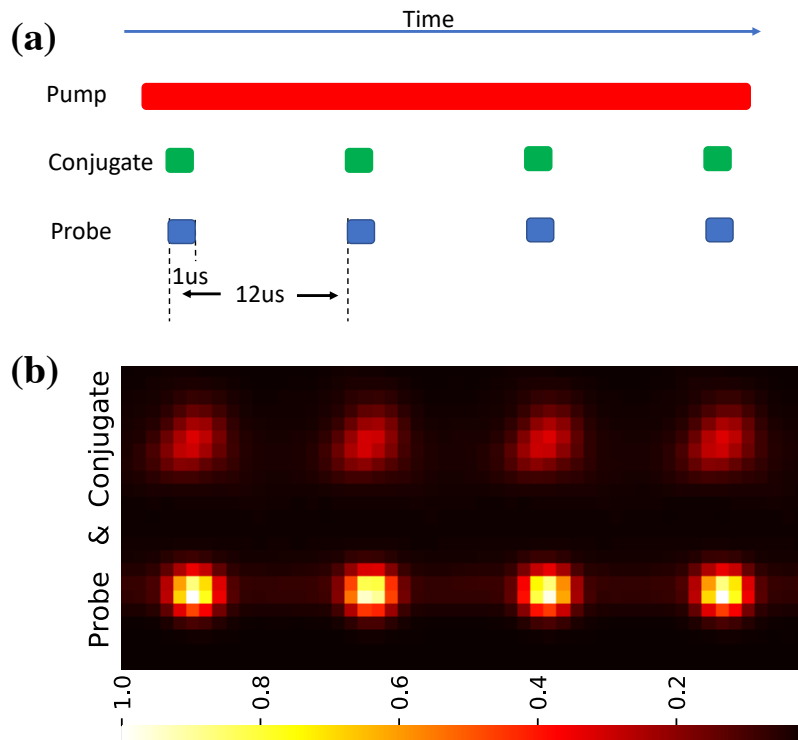


Figure 2.2: (a) Time sequencing of the pump and twin beams. The pulse duration of $1 \mu\text{s}$ and the duty cycle of $1/12$ is realized by pulsing the probe beam with an AOM. The CW pump beam is present all the time. (b) Typical images of the twin beams captured by the EMCCD camera with four consecutive pulses.

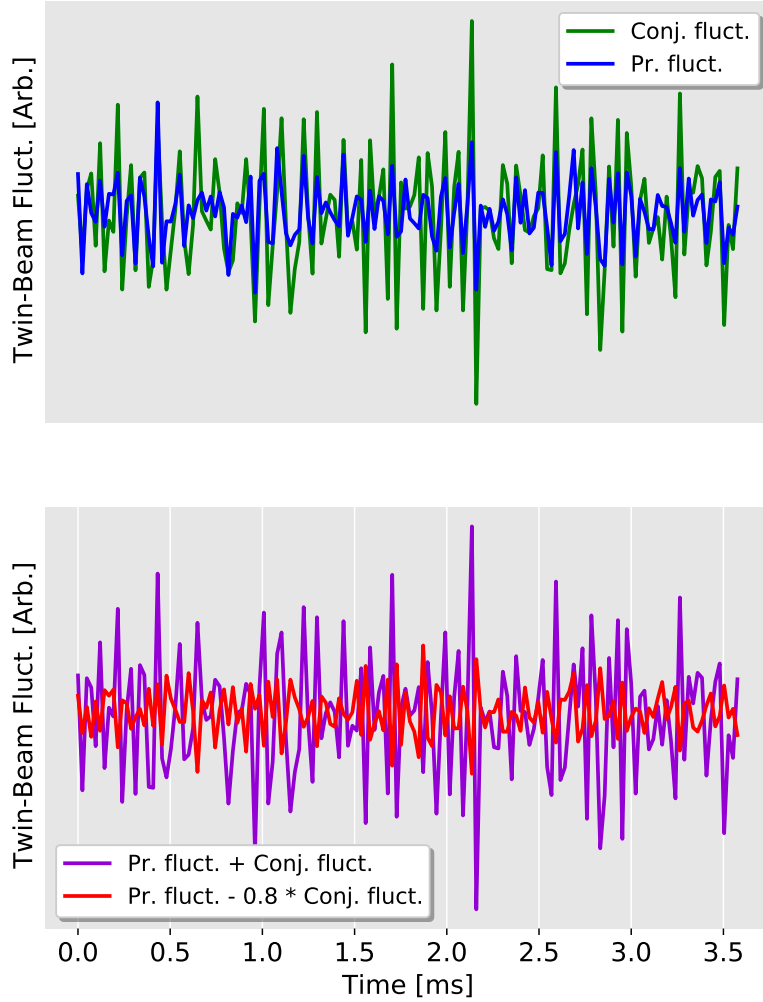


Figure 2.3: Temporal photon counts fluctuations of the probe $N_p(t)$ and conjugate $N_c(t)$ obtained by integrating the photon counts in the cropped regions in fig. 4.3. Clear similarities can be observed between the twin beams. The strong noise reduction in the subtraction as opposed to the summation of the $N_p(t)$ and $N_c(t)$ depicted in showcases strong correlations between them. The factor of 0.8 is for a better different fluctuation reduction.

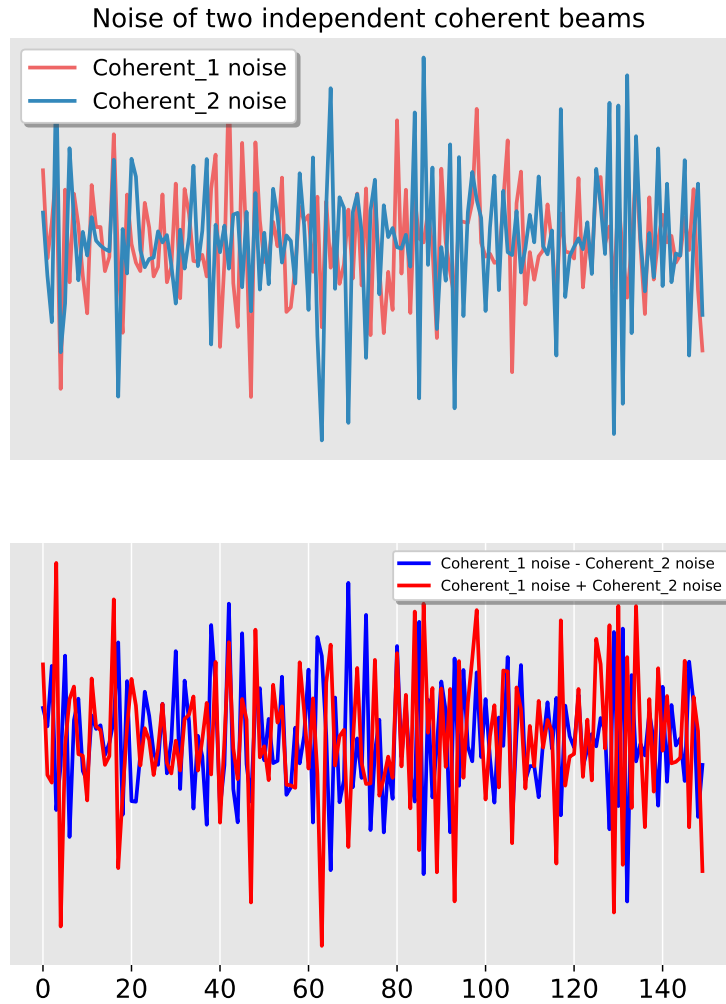


Figure 2.4: Temporal photon counts fluctuations obtained by integrating the photon counts in the cropped regions of two independent coherent beams. The beam size of two coherent beam is same with the size of probe and conjugate beam, and the EMCCD setting is also identical.

strong noise reduction in the subtraction as opposed to the summation of the $N_p(t)$ and $N_c(t)$ depicted in showcases strong correlations between them. This is the first demonstration of squeezed character of twin-beam by EMMCD in time domain. The Intensity-difference noise power spectrum measured by high quantum yield detect for the squeezed twin beams is shown in fig.2.5.

2.3 Results & Analysis

2.3.1 Temporal two-mode squeezing measured by photodiodes

We first measure the two-mode squeezing in a conventional way, i.e., using photodiodes to register intensity fluctuations in the beams of light in the temporal domain. After the second polarizer, we direct the probe and conjugate beams into the two ports of a balanced, amplified photodetector with a transimpedance gain of 10^5 V/A and 94% quantum efficiency at $\lambda = 795$ nm (not shown in Fig. 5.2(a)). The photodetector signals are sent to a radio frequency spectrum analyzer with a resolution bandwidth RBW of 300 kHz and a video frequency bandwidth VBW of 100 Hz. A typical squeezing spectrum is shown in Fig. 2.5 as the blue curve. The standard quantum limit (red curve) of this system is measured by picking off the probe before the cell, splitting it with a 50/50 non-polarizing beam splitter, and directing the resulting beams into the balanced, amplified photodetector. The balanced detection technique subtracts away common-mode noise to better than 25 dB. The balanced photodetector noise level is a measure of the standard quantum limit for the total amount of optical power arriving at the photodetector. The standard quantum limit should be independent of frequency, which is indeed the case within the bandwidth of the detection electronics, which begins to drop down above 3 MHz. We measure more than 6 dB of the two-mode squeezing around the analysis frequency of 1 MHz.

2.3.2 Temporal quantum noise reduction acquired by an EMCCD camera

We acquire the temporal quantum noise reduction of the twin beams through the use of the *kinetic* mode of the EMCCD camera. The EMCCD has 512×512 pixels with each pixel size of $16 \mu\text{m} \times 16 \mu\text{m}$. We focus the twin beams on the camera with an $1/e^2$ beam diameter of $\sim 50 \mu\text{m}$, occupying roughly 3 pixels as shown in Fig. 4.3(b). The temperature of the EMCCD is kept at

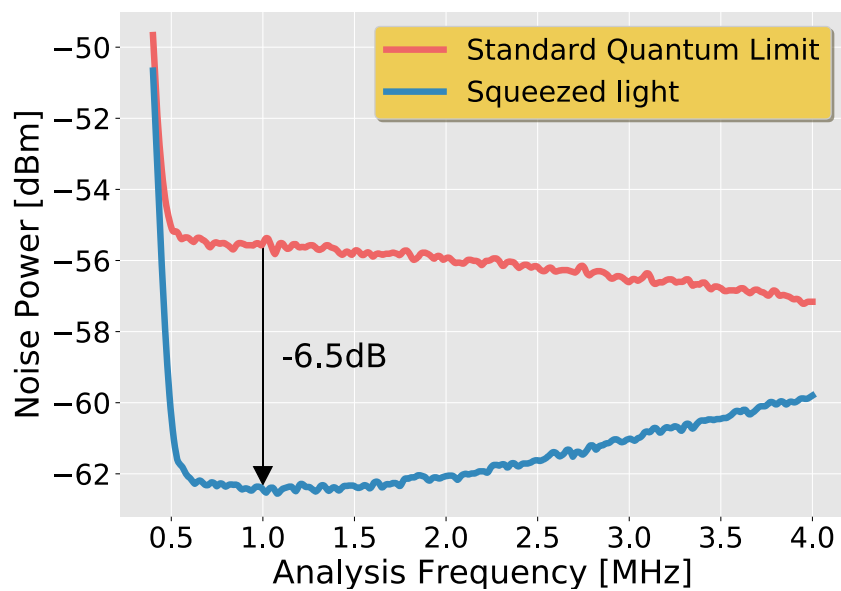


Figure 2.5: Intensity-difference noise power spectrum for the squeezed twin beams (blue line) and for the standard quantum limit (red line), obtained by a balanced photodetector in conjunction with a radio frequency spectrum analyzer (with a resolution and video frequency bandwidth of 300 kHz and 100 Hz, respectively). A two-mode squeezing of 6.5 dB is achieved around the analysis frequency of 1 MHz.

–75°C to curb the thermal noise contributions.

Since the pulse duration is 1 μs and the time interval between two consecutive pulses is 12 μs , thus in order to completely transfer all charges from the camera’s image area to the storage area within one pulse cycle, we can in principle choose to set the speed of vertical pixel shift (i.e., the time taken to vertically shift all pixels one row down) to any value as long as it is faster than 4 μs , given our beam size is merely 3 pixels across. However, the drawback with a fast vertical pixel shift speed is the reduction of charge transfer efficiency, which in turn causes ‘vertical smearing’ (i.e., light is still falling on the image area during the short time taken to transfer the charge from the image area to the storage area). In our case, we found a 0.9 μs vertical pixel shift speed in conjunction with a vertical clock voltage amplitude of 4 (to ensure that extremely high signals can be fully removed during the EMCCD clean cycle) worked best for us.

Another important setting of the EMCCD is the readout rate. It also ought to be fast enough to be within one pulse cycle. However, a faster readout rate always results in a higher readout noise. In our case, we adopt 3 MHz as our readout rate although technically it can be as fast as 17 MHz, but the price one has to pay is 8 fold more readout noise.

For each measurement, we capture 200 kinetic series (i.e., 200 frame sequences), with each frame containing 35 pairs of probe and conjugate images. For the measurement of the quantum noise reduction, we adopt a similar algorithm developed in Refs. [74, 75] but implement it in the temporal domain. In brief we crop a 10×10 pixel region around the maximum-intensity region in each probe and conjugate images, large enough to enclose their respective full beam profiles (see Fig. 4.3(b)), we then are able to obtain the quantities $N_p(t + \delta t)$, $N_p(t)$, $N_c(t + \delta t)$, and $N_c(t)$ representing the integrated photon counts for the *whole* beam profiles of the probe and conjugate beams in two consecutive frames with time interval of δt . For our measurements we characterize the quantum noise reduction by the parameter σ defined by

$$\sigma \equiv \frac{\langle \Delta^2[(N_p(t + \delta t) - N_p(t)) - (N_c(t + \delta t) - N_c(t))] \rangle_t}{\langle N_p(t + \delta t) + N_p(t) + N_c(t + \delta t) + N_c(t) \rangle_t}, \quad (2.1)$$

where the subtractions $N_p(t + \delta t) - N_p(t)$ and $N_c(t + \delta t) - N_c(t)$ are the photon counts in the

cropped regions in two successive probe and conjugate images with time interval of δt . The subtraction of the two successive images leads to the cancellation of the low-frequency portion of the classical noise as well as the Gaussian profiles of the probe and conjugate images [74, 75]. The numerator of Eq. (4.7) represents the temporal variance of the intensity-difference noise between the probe and conjugate pulses. The denominator gives the mean photon counts for the probe and conjugate pulses used for the analysis and represents the shot noise. For coherent state pulses $\sigma = 1$, which corresponds to the shot noise limit, while for thermal light or other classical states $\sigma > 1$. Temporally quantum correlated beams, like the twin beams generated in our experiment, will result in $\sigma < 1$, with a smaller σ corresponding to a larger degree of two-mode squeezing. It is worth mentioning that the parameter σ defined in Refs. [74, 75] characterizes the quantum correlations between *grouped pixels* of the twin-beam images in two consecutive frames.

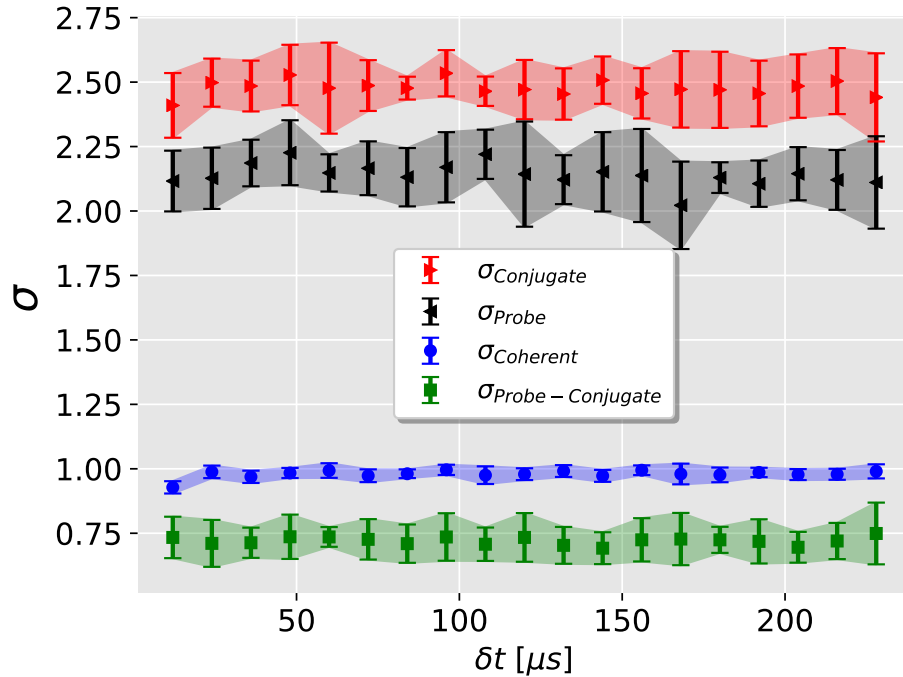


Figure 2.6: The temporal quantum noise reduction characterization σ as a function of the time interval δt between successive images for different beams of light. Green squares: twin beams; blue dots: coherent beams; black triangles: probe beam only; red triangles: conjugate beam only.

In Fig. 2.6, we plot σ as a function of δt for different beams of light. For each δt , we average 5 sets of 200 kinetic series and designate the error bar with one standard deviation. As expected, $\sigma \doteq 0.75 < 1$ for the twin beams (green squares), while $\sigma = 1$ when the twin beams are replaced with two coherent beams (blue dots), and $\sigma > 1$ for the probe beam (black triangles) and conjugate beam (red triangles) individually [85] (calculated as $\sigma_{p,c} = \langle \Delta^2 [N_{p,c}(t + \delta t) - N_{p,c}(t)] \rangle_t / \langle N_{p,c}(t + \delta t) + N_{p,c}(t) \rangle_t$). The notable degradation of the temporal quantum noise reduction measured by the EMCCD camera with respect to the one measured by the balanced photodiodes in Fig. 2.5 can be mainly attributed to a much worse common noise rejection (caused by the significant mismatch between the spatial modes of the twin beams as shown in Fig. 4.3(b)) and a much worse quantum efficiency of the EMCCD at 795 nm (less than 80% as compared to 94% for the photodiodes). We also repeated the experiment with different pulse duty cycles, but they seemed to play a nonessential role on the quantum noise reduction as long as we were in the shot-noise-limited regime, i.e., the σ is still close to unity for coherent beams.

It is worthy to mention that our quantum noise reduction $\sigma \doteq 0.75$ for the twin beams in the temporal domain is similar to the one reported in Refs. [74, 75] in the spatial domain. This is also as expected since when $\delta t = 12 \mu\text{s}$, we recover the ‘full spatial mode’ case in Refs. [74, 75].

2.4 Conclusions

In conclusion, we report a measurement scheme that is capable of acquiring the quantum noise reduction in the temporal domain using an EMCCD camera. We observe $\sim 25\%$ of temporal quantum noise reduction with respect to the shot-noise limit in images captured by the camera. To the best of our knowledge, this is the first experimental showcase that an EMCCD camera can be used to acquire quantum properties of light in the *temporal* domain.

We use FWM in an atomic ^{85}Rb vapor cell to generate the quantum-correlated twin beams of light. Major advantages of this quantum light generation scheme are narrow-band probe and conjugate beams (~ 20 MHz) [82, 86] along with an ultra-high photon-pair flux up to 10^{16} photons/s [76–82], which is a few orders of magnitude higher than the fluxes produced by spontaneous parametric down-converters (SPDCs). Therefore the bright twin beams can be readily applied in

some atom-light interaction based quantum protocols [87]. Moreover, the FWM process offers sufficient gains in a single-pass configuration producing bright quantum-correlated beams of light without a cavity [88]. This makes it possible to preserve the multi-spatial-mode nature of the bright twin beams [89,90] and to observe spatial quantum correlations in the macroscopic regime [74,75]. Our quantum light generation together with the measurement scheme reported here extend the EM-CCD's quantum measurement capability from spatial domain to temporal domain as well. This could make it possible to take advantage of the temporal and spatial quantum properties of light simultaneously. It therefore has the potential to pave the way for many applications in quantum metrology and quantum imaging, which would greatly benefit from the concurrent measurements of the quantum correlations in both the temporal and the spatial domains [91]

3. EXPERIMENTAL STUDY OF DECOHERENCE OF THE TWO-MODE SQUEEZED VACUUM STATE VIA SECOND HARMONIC GENERATION

Decoherence remains one of the most serious challenges to the implementation of quantum technology. It appears as a result of the transformation over time of a quantum superposition state into a classical mixture due to the quantum system interacting with the environment. Since quantum systems are never completely isolated from their environment, therefore decoherence cannot be avoided in realistic situations. Decoherence has been extensively studied, mostly theoretically, since it has many important implications and applications in quantum science and technology, such as in the fields of quantum information processing, quantum communication and quantum computation. Here we report a novel experimental scheme on the study of decoherence of a two-mode squeezed vacuum state via its second harmonic generation signal. One of the most important properties of squeezed light is the nonzero quantum correlation $\langle \hat{a}\hat{b} \rangle$ between two entangled modes a and b , our scheme can directly extract the decoherence of this quantum correlation. This is the first experiment study on the decoherence effect of a squeezed vacuum state without full density matrix tomography.

Given the fact that the most important property of a two-mode squeezed light is the nonzero quantum correlation $\langle \hat{a}\hat{b} \rangle$ between the two entangled modes a and b , our scheme is significant in that it can directly extract the decoherence of this quantum correlation in a controllable and measurable manner. This is the first experimental study on the decoherence effect of a squeezed vacuum state. Our scheme can directly extract the decoherence of the quantum correlation $\langle \hat{a}\hat{b} \rangle$ between two entangled modes a and b , which is the most important property of squeezed light.

3.1 Introduction

Realistic quantum systems are inevitably coupled with their environment. When a quantum system interacts with its environment, it will in general become entangled with a large number of environmental degrees of freedom [92–97]. It is this coupling between a quantum system and its

environment that causes decoherence, sometimes also referred to as environment-induced decoherence [98–103], which remains one of the most serious obstacles to the exploitation of quantum technology [104–108], although some protocols have been proposed [109, 110] and proof-of-principle experiment has been conducted [111] on how the effect of decoherence can be reversed. Such coupling can be generally understood in terms of classical noise [112], such as in the investigations of optical parametric amplification [113, 114] and in the spectral diffusion theory that is widely used in, for instance, optical and magnetic resonance spectroscopy [115, 116]. Stated in general terms, decoherence describes how interactions with the environment influence the statistics of results of future measurements on the quantum system.

Decoherence happens all around us, and in this sense its consequences should be readily observed. There are several experimental areas that have played a key role in the experimental studies of decoherence: atom–photon interactions in a cavity [117], interferometry with mesoscopic molecules [118], superconducting systems such as SQUIDs and Cooper-pair boxes [119], and trapped ions [120]. Recently, quantum nanomechanical systems also yield promising results for experimental tests of decoherence [121]. There are also some experimental investigations using decoherence for testing quantum mechanics [122]. These experiments are not only useful for evaluating the predictions of decoherence models, but also offering guidance for designing quantum devices that are capable of circumventing the detrimental influence of the environment.

Among these prior experimental studies on decoherence, some are of particular interest to us due to the fact that they were conducted in an ‘all-optical’ manner, for instance, Kwiat *et al.* used polarization entangled photon pairs produced by spontaneous parametric down-conversion to search for decoherence-free subspaces [104]; Almeida *et al.* also used polarization entangled photon pairs to demonstrate that quantum entanglement may suddenly disappear although the environment-induced decay is asymptotic [105]. Both experiments employed the sophisticated quantum state tomography [123, 124] to characterize the effect of decoherence. In this paper, we report a novel all-optical experimental scheme for studying the effect of decoherence. Specifically, by measuring the second harmonic generation (SHG) produced by an ultrabright two-mode

squeezed vacuum (TMSV) state, We showcase our ability to study the action of decoherence on a two-mode squeezed vacuum (TMSV) state in a gradual and controlled manner by measuring its second harmonic generation (SHG) signal from a Beta Barium Borate (BBO) crystal. The TMSV state is generated in the continuous-variable regime, hence a full density matrix tomography would not be applicable here. The decoherence is introduced by a neutral density (ND) filter to impose an uniform attenuation to the TMSV state., which is different from the ‘dephasing’ model that has been extensively studied [122]. Our results are significant because the effect of decoherence on a squeezed vacuum state has been rarely investigated experimentally. More essentially, given that the most important property of a two-mode squeezed state is the nonzero quantum correlation $\langle \hat{a}\hat{b} \rangle$ between the two entangled modes a and b , which ultimately determines the squeezing level of the state, our experiment offers a method that can directly extract the decoherence of this quantum correlation.

3.2 Theoretical Analysis

3.2.1 Cauchy-Schwartz inequality violation for the phase-sensitive correlation $\langle \hat{a}\hat{b} \rangle$

It is well known that for quantum fields Cauchy-Schwartz inequalities (CSI) can be violated, because quantum fields can have P -distributions that do not have properties of a classical probability distribution. Such violations have been traditionally studied for intensity correlations like $\langle \hat{a}^\dagger \hat{a} \hat{a}^\dagger \hat{a} \rangle$, $\langle \hat{a}^\dagger \hat{a} \hat{b}^\dagger \hat{b} \rangle$. Here we discuss a different correlation having phase-sensitive information. Let us first consider a and b to be complex random variables, then it is clear that for classical random variables,

$$\langle |ca + db^*|^2 \rangle \geq 0 \quad \forall c, d, \quad (3.1)$$

where c and d are arbitrary complex variables. This inequality for classical complex variables follows from the positivity of classical probability distributions. Equation (3.1) leads to

$$|c|^2 \langle |a|^2 \rangle + |d|^2 \langle |b|^2 \rangle + c^* d \langle a^* b^* \rangle + cd^* \langle ab \rangle \geq 0, \quad (3.2)$$

and hence from the properties of the quadratic forms, it follows that

$$\begin{vmatrix} \langle |a|^2 \rangle & \langle a^* b^* \rangle \\ \langle ab \rangle & \langle |b|^2 \rangle \end{vmatrix} \geq 0. \quad (3.3)$$

The condition (3.3) leads to the CS inequality

$$|\langle ab \rangle|^2 \leq \langle |a|^2 \rangle \langle |b|^2 \rangle. \quad (3.4)$$

On the other hand, if we employ similar argument in the quantum domain using density matrices, then instead of Eq. (3.1), we can get

$$\text{Tr}\{\rho(c^* \hat{a}^\dagger + d^* \hat{b})(c \hat{a} + d \hat{b}^\dagger)\} \geq 0, \quad (3.5)$$

or

$$|c|^2 \langle \hat{a}^\dagger \hat{a} \rangle + |d|^2 \langle \hat{b} \hat{b}^\dagger \rangle + c^* d \langle \hat{a}^\dagger \hat{b}^\dagger \rangle + c d^* \langle \hat{a} \hat{b} \rangle \geq 0, \quad (3.6)$$

which leads to

$$|\langle \hat{a} \hat{b} \rangle|^2 \leq \langle \hat{a}^\dagger \hat{a} \rangle \langle \hat{b} \hat{b}^\dagger \rangle = \langle \hat{a}^\dagger \hat{a} \rangle \langle \hat{b}^\dagger \hat{b} + 1 \rangle. \quad (3.7)$$

On comparing Eq. (3.7) with Eq. (3.4), we can see that quantum fields with nonzero phase-sensitive correlations will always violate the classical inequity (3.4). All this discussion is based on the fact that quantum optical detectors measure the normally ordered correlations. Our experimental scheme is set up in such a way that we are able to directly extract the decoherence of the quantum correlation $\langle \hat{a} \hat{b} \rangle$.

3.2.2 Characterization of decoherence of two-mode squeezed vacuum state via its SHG signal

Let us consider a TMSV state given by $\hat{S}(\xi)|0,0\rangle$, where $\hat{S}(\xi) = e^{\xi\hat{a}^\dagger\hat{b}^\dagger - \xi^*\hat{a}\hat{b}}$ is the two-mode squeezing operator and $\xi = re^{i\theta}$, where r is the squeezing parameter. The mean number of photons for each mode is the same, i.e., $\langle\hat{a}^\dagger\hat{a}\rangle = \langle\hat{b}^\dagger\hat{b}\rangle = \sinh^2 r$, and we let p_0 represent the mean number of photons of the state, then

$$p_0 = \langle\hat{n}\rangle = \langle\hat{a}^\dagger\hat{a} + \hat{b}^\dagger\hat{b}\rangle = 2\sinh^2 r. \quad (3.8)$$

Let ρ be the density matrix of the TMSV state, $\rho = \hat{S}(\xi)|0,0\rangle\langle 0,0|\hat{S}^\dagger(\xi)$. The decoherence of the TMSV state is described by the master equation:

$$\frac{\partial\rho}{\partial t} = -\gamma(\hat{a}^\dagger\hat{a}\rho - 2\hat{a}\rho\hat{a}^\dagger + \rho\hat{a}^\dagger\hat{a}) - \gamma(\hat{b}^\dagger\hat{b}\rho - 2\hat{b}\rho\hat{b}^\dagger + \rho\hat{b}^\dagger\hat{b}), \quad (3.9)$$

where γ gives the decay of the field amplitude. The dynamical equation Eq. (3.9) is solved subject to the initial condition $\rho(t=0) = \hat{S}(\xi)|0,0\rangle\langle 0,0|\hat{S}^\dagger(\xi)$. Instead of presenting a time-dependent solution for the full density matrix, we present the result for the normally-ordered correlations of arbitrary order. It turns out that

$$\langle(\hat{a}^\dagger)^m\hat{a}^n(\hat{b}^\dagger)^p\hat{b}^q\rangle_t = \beta^{(m+n+p+q)/2}\langle(\hat{a}^\dagger)^m\hat{a}^n(\hat{b}^\dagger)^p\hat{b}^q\rangle_0, \quad (3.10)$$

where $\beta = e^{-2\gamma t}$ and $1 - \beta$ represents the absorption of the modes. The subscript '0' denotes $t = 0$. In particular,

$$\begin{aligned} \langle\hat{a}^\dagger\hat{a}\rangle_t &= \beta\langle\hat{a}^\dagger\hat{a}\rangle_0, \quad \langle\hat{b}^\dagger\hat{b}\rangle_t = \beta\langle\hat{b}^\dagger\hat{b}\rangle_0, \\ \langle\hat{a}^\dagger\hat{a}\hat{b}^\dagger\hat{b}\rangle_t &= \beta^2\langle\hat{a}^\dagger\hat{a}\hat{b}^\dagger\hat{b}\rangle_0. \end{aligned} \quad (3.11)$$

The correlation $\langle \hat{a}^\dagger \hat{a} \hat{b}^\dagger \hat{b} \rangle$ for the TMSV state is well known to be given by

$$\begin{aligned} \langle \hat{a}^\dagger \hat{a} \hat{b}^\dagger \hat{b} \rangle &= \langle \hat{a}^\dagger \hat{a} \rangle \langle \hat{b}^\dagger \hat{b} \rangle + |\langle \hat{a} \hat{b} \rangle|^2 \\ &= \sinh^2 r \times \cosh^2 r + \sinh^4 r, \end{aligned} \quad (3.12)$$

the phase-sensitive correlation $|\langle \hat{a} \hat{b} \rangle|$ has the value of $\sinh r \times \cosh r$ and satisfies the equality sign in Eq. (3.7). The decoherence of the intensity-intensity correlation $G_{ab}^{(2)}$ between the two modes is therefore given by

$$G_{ab}^{(2)} = \langle \hat{a}^\dagger \hat{a} \hat{b}^\dagger \hat{b} \rangle_t = \beta^2 (\sinh^2 r \times \cosh^2 r + \sinh^4 r). \quad (3.13)$$

In the next section we outline our procedure for studying the decoherence of the quantum correlation $\langle \hat{a} \hat{b} \rangle$.

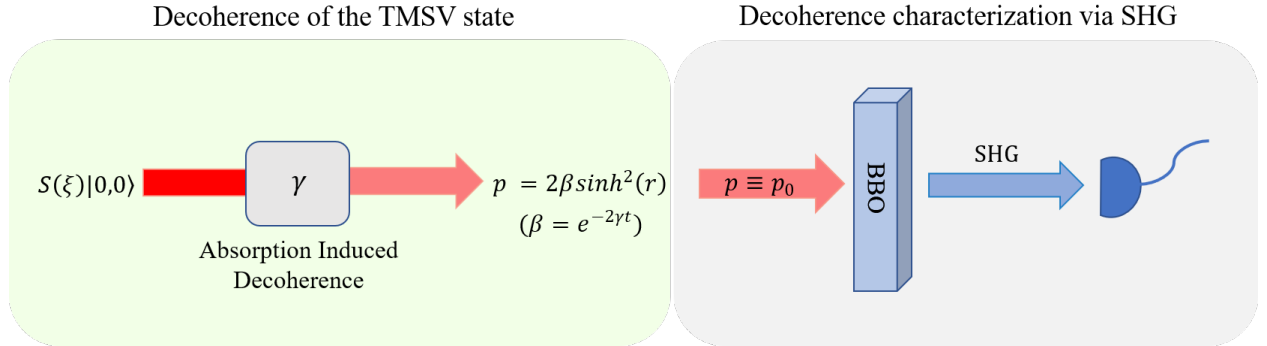


Figure 3.1: Theoretical decoherence characterization of the TMSV state via its SHG signal. To isolate the effect of decoherence on the quantum correlation $\langle \hat{a} \hat{b} \rangle$, experiment is performed by holding power p constant, i.e., $p \equiv p_0$.

3.2.3 Characterization of decoherence of the two-mode squeezed vacuum state via its SHG signal

In this section, we demonstrate that the decoherence of a TMSV state can be characterized via its SHG signal from a BBO crystal. The SHG signal is proportional to the intensity-intensity correlation $G_{ab}^{(2)}$ given by Eq. (3.13). We first note that the squeezing parameter r is proportional to the power P_0 of the pump light that is used to produce the TMSV state via the four-wave mixing (FWM) process (see details in Section III). As shown in Eq. (3.11), the output power

$$\begin{aligned} p_{\text{out}} &= 2\beta \sinh^2 r, \\ r &\equiv \alpha P_0, \end{aligned} \tag{3.14}$$

where α is related to the strength of the FWM process.

While the absorber attenuates the power of the TMSV state (see Fig. ??), we make up for the loss of power by increasing the power of the pump, namely,

$$2\beta \sinh^2 r = 2\beta \sinh^2(\alpha P_0) = 2 \sinh^2(\alpha P'_0) \equiv p_0, \tag{3.15}$$

where p_0 is the fixed power value. Clearly P'_0 depends on the parameter β .

We perform the SHG measurements by changing the absorption (varying β) but holding constant the number of photons in the TMSV beam emerging from the decohering mechanism, i.e., the absorber. Thus when β is changed, then P'_0 is changed appropriately as determined by Eq. (3.15). Therefore, by holding p_0 constant, the intensity-intensity correlation $G_{ab}^{(2)}$ in Eq. (3.13) can be rewritten as

$$G_{ab}^{(2)} = \frac{p_0^2}{2} + \frac{p_0}{2} \times \beta. \tag{3.16}$$

It is important to note that the occurrence of the β term in Eq. (3.16) can be traced back to the presence of the unity in Eq. (3.7).

In the experiment we use a ND filter to impose decoherence, and the transmission coefficient

$\beta = 10^{-\text{ND}}$. Then the relation between the SHG signal induced by the *partially-decoherent* TMSV state and the attenuation ND can be therefore readily obtained:

$$\text{SHG} \propto G_{ab}^{(2)} = \frac{p_0^2}{2} + \frac{p_0}{2} \times 10^{-\text{ND}}. \quad (3.17)$$

It is worth pointing out that for a classical beam of light with power p_0 , its SHG signal is $\propto p_0^2$, thus the linear term $(p_0/2) \times 10^{-\text{ND}}$ in Eq. (3.17) is solely due to the quantum property of the correlation $\langle \hat{a}\hat{b} \rangle$, and it can only be degraded but never vanishes just by imposing absorption to the TMSV state. Another interesting aspect that emerges from Eq. (3.17) is that because of the way we set up the experiment, the decoherence term shows up in the *linear* regime of the power dependence of the SHG signal.

3.3 Experiment and Results

3.3.1 Experimental setup

The setup of our experimental scheme is shown in Fig. 5.2(a). We generate the TMSV state with the FWM process in a ^{85}Rb atomic vapor cell. The vapor cell is kept at 112 °C to maintain enough atom number density for the interaction. The respective ^{85}Rb atomic level structure is shown in Fig. 5.2(b). The atomic medium is pumped by a strong (up to ~ 1.2 W) narrow-band continuous-wave (CW) laser at frequency ν_1 ($\lambda = 795$ nm) with a typical linewidth $\Delta\nu_1 \sim 100$ kHz and $700 \mu\text{m}$ $1/e^2$ radius. The pump laser is blue-tuned by a ‘one-photon detuning Δ ’ of 900 MHz with respect to the ^{85}Rb $5S_{1/2}, F = 2 \rightarrow 5P_{1/2}, D1$ transition. Due to the FWM parametric process, two pump photons are converted into a pair of twin photons, namely ‘probe ν_p ’ and ‘conjugate ν_c ’ photons, adhering to the energy conservation $2\nu_1 = \nu_p + \nu_c$ (see the level structure in Fig. 5.2(b)). These twin photons are separated in frequency by twice of the hyperfine splitting in the electronic ground state of ^{85}Rb , i.e., $\nu_c - \nu_p = 2\nu_{HF}$. The finite length of the atomic vapor cell (12.5 mm) slightly relaxes the longitudinal phase matching condition and allows for a range of angles, which effectively sets the angular acceptance of the FWM process, and produces the TMSV state in a form of ‘light cone’ after the cell. The cross-section of the cone is shown in

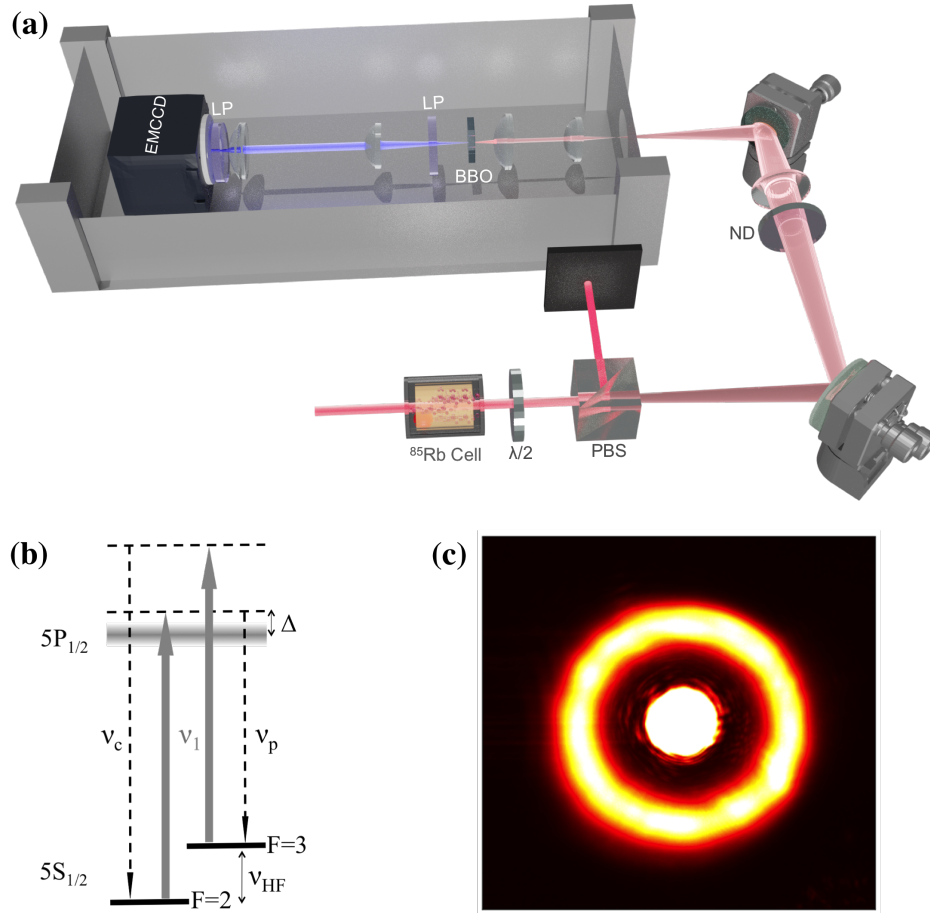


Figure 3.2: (a) Experimental setup in which a CW laser-pumped ^{85}Rb vapor cell produces a TMSV state via the FWM process. The TMSV beam (i.e. the ‘light cone’) is separated from the pump beam by a $\sim 2 \times 10^5 : 1$ polarizing beam splitter after the cell. The SHG signal from the BBO crystal is collected by an EMCCD camera. Two low-pass filters are mounted in front of the camera to eliminate undesired excitation photons. The BBO crystal and the EMCCD camera are enclosed in a light-proofing box to block ambient light. PBS: polarizing beam splitter, ND: neutral density filter, LP: low-pass filter. (b) Level structure of the D1 transition of ^{85}Rb atom. The optical transitions are arranged in a double- Λ configuration, where ν_p , ν_c and ν_1 stand for probe, conjugate and pump frequencies, respectively, fulfilling $\nu_p + \nu_c = 2\nu_1$ and $\nu_c - \nu_p = 2\nu_{HF}$. The width of the excited state in the level diagram represents the Doppler broadened line. Δ is the one-photon detuning. ν_{HF} is the hyperfine splitting in the electronic ground state of ^{85}Rb . (c) Image of the cross-section of the TMSV state, i.e., the ‘light cone’, where the bright central spot is the residual pump beam.

Fig. 5.2(c), where the bright central spot is the residual pump beam not completely filtered out by the PBS at the exit of the cell (See Fig. 5.2(a)). In the experiment, the central spot is blocked by a small black metal disk mounted on an extremely thin wire, so that the integrity of the TMSV state is not affected.

After the cell, the TMSV state is collimated to $\sim 1 \text{ mm } 1/e^2$ radius before focused on a BBO crystal by a 16 mm aspheric lens. The SHG signal is collected by an electron-multiplying charge-coupled-device (EMCCD) camera, in front of which two low-pass filters are mounted to eliminate undesired excitation photons. The decoherence measurement stage including the BBO crystal and the EMCCD camera are enclosed in a light-proofing box to block ambient light. A ND filter is mounted in front of the box to introduce decoherence to the TMSV state.

3.3.2 Results

We first characterize the TMSV beam produced with the FWM process in the ^{85}Rb vapor cell. As we increase the pump power P , the TMSV beam (light cone) power p_{TMSV} should also increase according to Eq. (3.8) since the squeezing parameter r is linearly proportional to the pump power P . In Fig. 3.3 we plot the data along with the theoretical fit, $p_{\text{TMSV}} \propto \sinh^2(\alpha P)$, where α is the proportional constant. The error bars represent statistical uncertainties of one standard deviation. Although there seems to exist a systematic deviation away from the fit, the overall agreement is decent.

We also note that according to Eq. (3.17), when there is no ND filter ($\text{ND} = 0$) the SHG signal follows a polynomial dependence on the TMSV state power p_0 , i.e., $\text{SHG} \propto p_0^2/2 + p_0/2$. In order to verify this polynomial functionality, the measured SHG signals versus p_0 are plotted in Fig. 3.4 as blue dots. They agree very well with a polynomial behavior, represented by the fit function $0.073 \times (p_0^2 + p_0)$. Note that here p_0 has the dimension of $[10^4 \times p_{\text{TMSV}}/\text{W}]$, where p_{TMSV} is the TMSV beam power on the x -axis.

In order to study the effect of decoherence on the TMSV state imposed by an uniform attenuation, the optical density of the ND filter, i.e., the absorption level, is increased while the input beam (i.e., the ‘partially-decoherent’ TMSV beam) power before the BBO crystal is fixed at $80 \mu\text{W}$. This

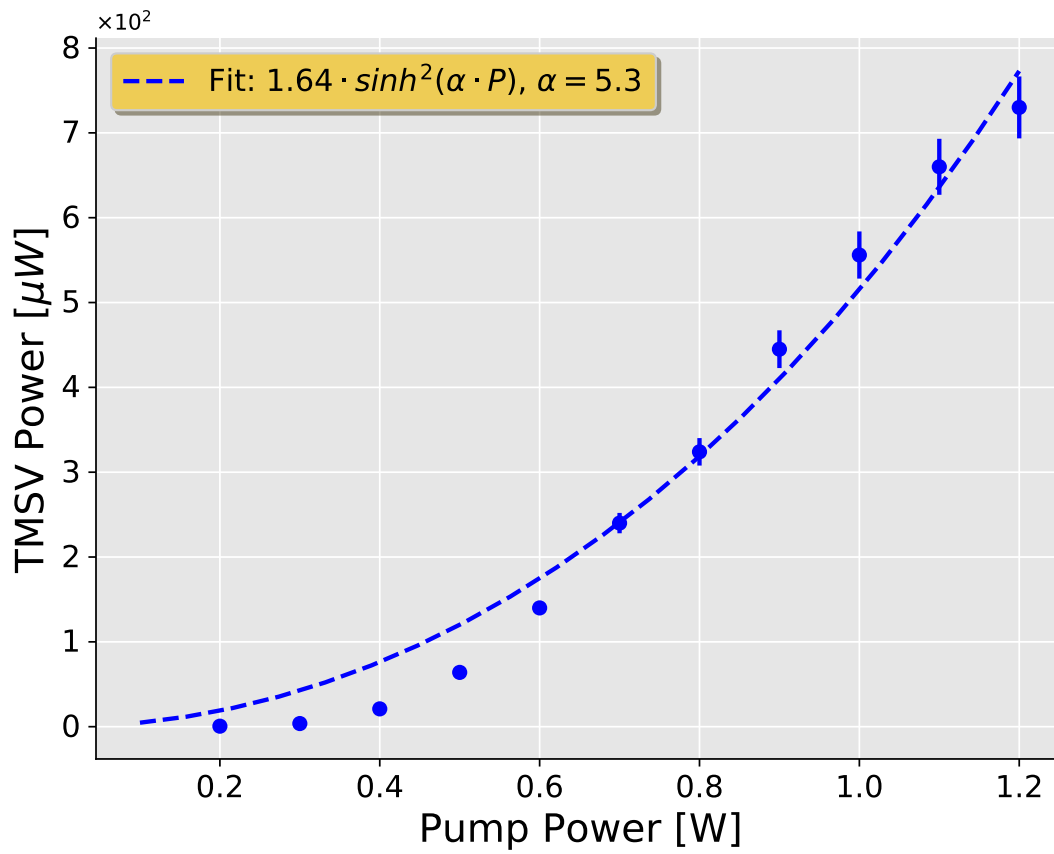


Figure 3.3: TMSV beam (light cone) power as a function of pump power. Dashed line is the theoretical fit according to Eq. (3.8) with $r \equiv \alpha P$, where P is the pump power.

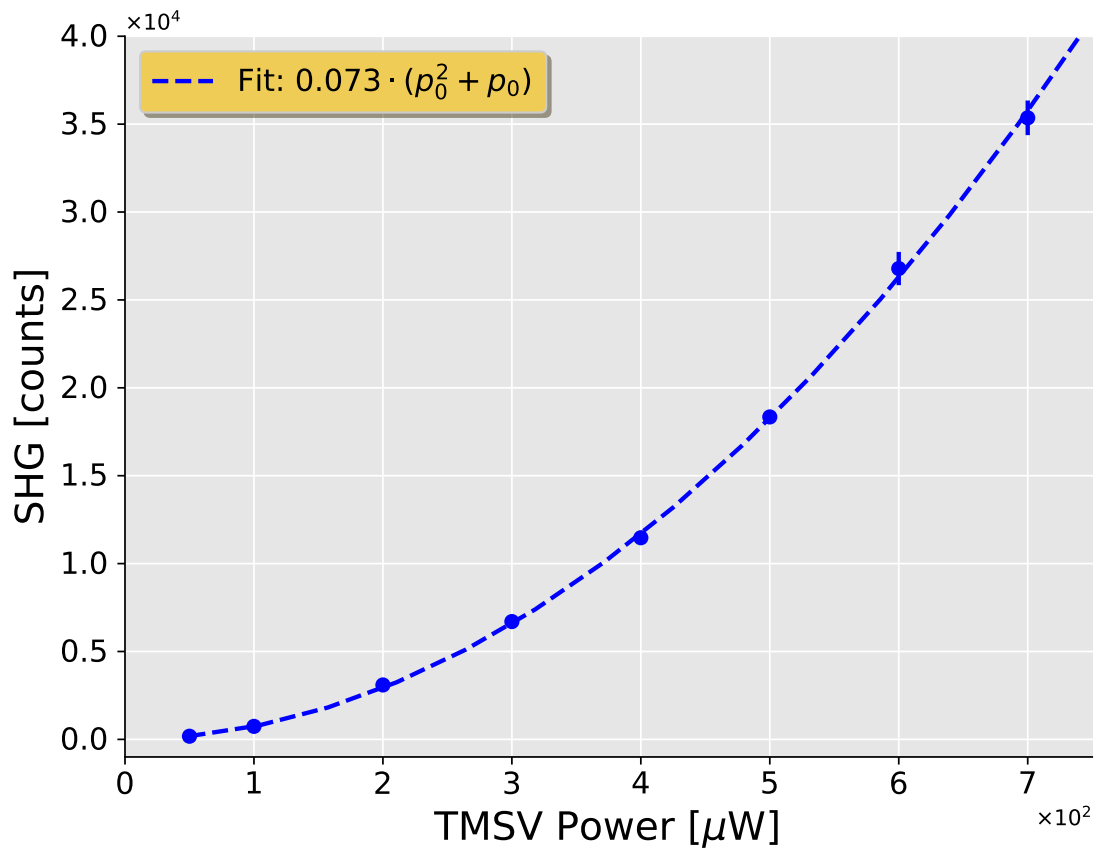


Figure 3.4: SHG signal as a function of the TMSV beam (light cone) power. Dashed line is a polynomial fit according to Eq. (3.17) with $\text{ND} = 0$.

can be done by increasing the pump power appropriately (see Fig. 3.3). In Fig. 3.5, we plot the SHG signal induced by the partially-decoherent TMSV beam as a function of the transmission of the ND filter. Blue dots are the SHG measurements for 80 μW partially-decoheret TMSV beams of light, plotted with y -axis on the left-hand side of the graph. The dashed blue line represents the fit function $(\kappa/2) \times (p_0^2 + p_0 \times 10^{-\text{ND}})$ according to Eq. (3.17) with fitting parameters $\kappa = 583$ and $p_0 = 2.6$. This theoretical fit yields an almost perfect agreement with the experimental observations. As a comparison, we also plot SHG signals induced by 80 μW coherent beams of light with y -axis on the right-hand side of the graph. As shown in Fig. 3.5 with these red dots and as what we expected, they form a flat line due to the fact that statistical properties of coherent light are indifferent to absorption.

Notice that it may not be fair to compare the ‘absolute’ SHG signals induced by the TMSV beam and the coherent beam in Fig. 3.5 because we were not able to make the coherent beam a ‘doughnut’ shape like the TMSV beam, therefore they had different phase-matching conditions at the BBO crystal. Also note that, the first data point in Fig. 3.5 is the SHG signal induced by 80 μW TMSV beam without a ND filter, which is slightly higher than the second data point in Fig. 3.4 induced by 100 μW TMSV beam. We attribute this discrepancy again to different phase-matching conditions (due to slightly different optical alignments) under which these two sets of measurements were taken.

3.4 Conclusions

We demonstrate a novel and unsophisticated all-optical experimental scheme for studying the decoherence effect on a TMSV state. The TMSV state is generated with the FWM process in an atomic ^{85}Rb vapor cell, and the decoherence is characterized through the SHG signal induced by the TMSV state from a BBO crystal. Although squeezed state nowadays has become an extremely versatile tool for precision measurements and for interferometry due to its capability of offering unprecedented measurement sensitivity [83, 108], the decoherence effect of a squeezed state has rarely been investigated experimentally. Our scheme therefore would make a great addition to the research on decoherence of nonclassical states. The significance of our experiment resides

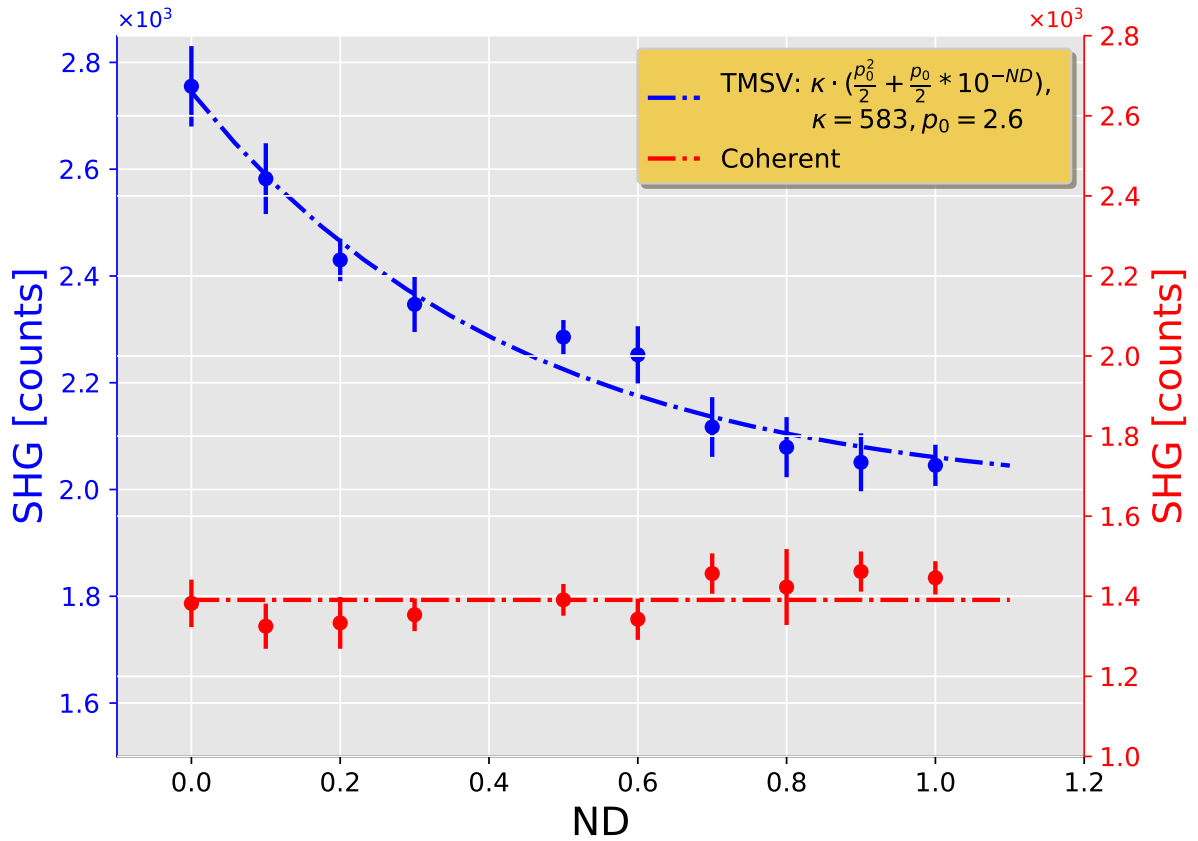


Figure 3.5: SHG signals induced by $80 \mu\text{W}$ partially-decoherent TMSV beams of light (blue dots, left-hand side y -axis) and $80 \mu\text{W}$ coherent beams of light (red dots, right-hand side y -axis) as a function of transmission of ND filters. Dashed blue line is the theoretical fit according to Eq. (3.17).

in the fact that it demonstrates our capability of directly extracting the decoherence of quantum correlation $\langle \hat{a}\hat{b} \rangle$ between two entangled modes a and b , which is the most important property of a two-mode squeezed state. It also showcases the possibility of characterizing the effect of decoherence in a controllable and measurable manner on a quantum state in the continuous-variable regime.

4. OBSERVATION OF QUANTUM ADVANTAGE WITH SQUEEZED LIGHT FOR ABSORPTION MEASUREMENT

Absorption measurement is an exceptionally versatile tool for most applications in science and engineering. For absorption measurements using laser beams of light, the sensitivity is theoretically limited by the shot noise due to the fundamental Poisson distribution of photon number in laser radiation. In practice, the shot-noise limit can only be achieved when all other sources of noise are eliminated. Here, we use bright squeezed light to demonstrate that direct absorption measurement can be performed with sensitivity beyond the shot-noise limit. We present a practically realizable scheme, where the bright squeezed light is generated by the four-wave mixing process in an atomic rubidium vapor cell. This is a direct sub-shot-noise measurement of absorption that requires neither homodyne/lock-in nor logic coincidence detection schemes. More than 1.2 dB quantum advantage for the measurement sensitivity is obtained at faint absorption levels ($\leq 10\%$). The observed quantum advantage when corrected for optical loss would be equivalent to 3 dB. We present detailed theoretical analysis for the expected quantum advantage. Our results are similar to those reported for phase measurements.

4.1 introduction

It has been demonstrated that one can improve the sensitivity and precision of many classical measurement techniques using various quantum states of light [73, 125–138] (For instance, the experimental work reported is a sub-shot-noise measurement of an intensity modulation on one of the quantum-correlated twin beams, and the intensity is modulated by adjusting the transmission of the beam from a liquid-crystal cell). Most prominently, sub-shot-noise detection of changes in optical phase have been demonstrated in interferometers using quantum light [79, 139–141] and have been implemented for gravitational wave detection. Although a straightforward readily attainable approach to achieve desired performances of a classical measurement is to simply increase the photon flux of the probe light to yield a greater signal-to-noise ratio, it has been proven unfeasible

whenever one faces limits on the brightness of the optical probes, for instance, in the case where samples can be altered or damaged by the probe light [135, 142]. It is therefore highly desirable to optimize measurement sensitivity with a fixed amount of input photon flux [135]. It is also important to note that for measurement schemes where the sensitivity itself varies with parameters of the measured sample it is possible for the sensitivity to be degraded, potentially requiring either prior knowledge about the optical sample or the addition of a feedback servo loop to ensure a sub-shot-noise performance [52, 143, 144]. For example, the use of amplitude squeezed light to acquire improved sensitivity with homodyne detection [145, 146] implies the sensitivity itself is dependent on the optical phase introduced by the sample being measured, leading to a random amount of sensitivity that can be above the shot noise limit (SNL).

Since the intensity measurement of an idealized laser fluctuates with a Poisson distribution, it is therefore used to define the shot-noise limit (SNL) in optical measurements, and it can only be reached in classical experiments once all other sources of noise are removed. For a direct measurement of optical transmission, the number of photons that pass through a sample is used to estimate the sample's absorption α , and thus the estimation sensitivity $\Delta\alpha$ is determined by the SNL. One of the most popular approaches that allow for a sub-shot-noise measurement of an unknown sample's transmission is to use quantum-correlated beams of photons [136, 137] (In fact, the 'quantum advantage' reported in Ref. [136] is actually not over the shot-noise limit, but rather an advantage over their 'system limit,' so strictly speaking it is not a 'sub-shot-noise' measurement scheme). In particular, such techniques have been implemented in the context of imaging [72, 73, 147]. For practical applications, the reduction of noise between quantum-correlated beams of photons generated with spontaneous parametric down-conversion (SPDC) [148] or four-wave mixing (FWM) [79] is very attractive since correlations between photon pairs are unaffected by optical phase induced by a measured sample. This technique can be transferred to detecting correlated photons altogether in the same image of a charge-coupled-device (CCD) camera to acquire sub-SNL measurement in the spatial domain [72–75, 132], and most recently in the temporal domain as well [149]. With the inclusion of a spatially absorbing sample, it has been shown that correlated photons can be used

to suppress noise in imaging objects to a degree that out-performs classical measurement using an equally efficient detection [73, 150]. Since absorption measurement is the most versatile tool for many applications in spectroscopy, metrology, chemistry and biology, improving the measurement sensitivity is thus indisputably beneficial to both science and engineering communities.

However, demonstrating an unambiguous real-world sensitivity improvement in a quantum way is not trivial [141]. Therefore, it is still valuable for exemplary experiments to be performed to observe clear quantum advantages, specifically to demonstrate that the sensitivity acquired with the reported data cannot be classically obtained. It is therefore absolutely valuable for experiments to be performed to observe clear quantum advantages that gained by using quantum states of light in absorption measurements.

In this article, we report a practically realizable experimental scheme for direct absorption measurement. We use bright squeezed light as the source to demonstrate clear quantum advantages over the SNL. Unlike many sub-SNL phase measurements requiring uniquely structured local oscillators for effective homodyne detection, like in Ref. [79] for instance, or many sub-SNL absorption measurements requiring either involved detection schemes, like in Ref. [125], or sophisticated estimators, like in Ref. [137], where an unbiased estimator that uses all detected photons that pass through a sample was implemented. A strict requirement for this estimator to be satisfactory is a sufficiently high ($> 90\%$) overall detection quantum efficiency, which would limit the scheme's applicability. In comparison, our experimental scheme is much more straightforward. A FWM atomic vapor cell together with an electron-multiplying charge-coupled-device (EMCCD) camera comprise the bulk of what is needed to acquire a sub-SNL absorption measurement. Information containing absorption of the sample being measured can be readily obtained by simply integrating the images captured by the EMCCD camera, no homodyne/lock-in or logic coincidence is required. Our scheme therefore is very applicable in many circumstances where sub-SNL absorption measurements are highly desirable. We observe more than 1.2 dB quantum advantage for weak absorption levels ($\leq 10\%$), which is significantly higher than the results reported in Ref. [137] (~ 0.7 dB when converted to our definition of quantum advantage) for weak

absorption measurements using entangled photo pairs generated by a type-II spontaneous parametric down-converter. Our advantage is also more than twice of that reported in Ref. [138] where a single-mode amplitude squeezed light generated with an optical phase-sensitive amplifier is used. We also provide in this article a theoretical model to analyze and gain insights into the experimental observations.

4.2 Theoretical analysis of the quantum advantage for measurement sensitivity

Our bright squeezed light is generated with the FWM process in an atomic ^{85}Rb vapor cell [76–82]. The atomic medium possesses a large third-order electric susceptibility $\chi^{(3)}$, and when appropriately chosen laser light ‘seeds’ the medium, ‘twin beams’, also known as the ‘probe’ and ‘conjugate’ beams, are produced. The theoretical modeling of the bright twin beams generation in the FWM process is complex, as in the experiment one deals with the probe and conjugate beams of finite bandwidth. In fact, the bandwidth of the twin beams in our scheme is merely ~ 20 MHz [82, 86], which is much narrower compared to what one generates with SPDCs. Therefore, we can recover many of the aspects of our observations in terms of a theoretical model based on an equivalent *single-mode* description of the probe and conjugate beams [80]. In brief, we use the single-mode approximation and designate \hat{a} and \hat{b} as the mode operators for the probe and conjugate beams respectively, the final operators after detection can therefore be expressed as

$$\hat{a}_f = \sqrt{\eta_p} \{ \sqrt{1-\alpha} [(\cosh r)\hat{a} + e^{i\theta}(\sinh r)\hat{b}^\dagger] + i\sqrt{\alpha}\hat{\nu}_\alpha \} + i\sqrt{1-\eta_p}\hat{\nu}_p, \quad (4.1)$$

$$\hat{b}_f^\dagger = \sqrt{\eta_c} [(\cosh r)\hat{b}^\dagger + e^{-i\theta}(\sinh r)\hat{a}] - i\sqrt{1-\eta_c}\hat{\nu}_c^\dagger,$$

where r is the squeezing parameter of the FWM, θ is the relative phase between the twin beams (approximately, $\theta \cong 2\pi \times 2\nu_{HF} \times L/c$, where $2\nu_{HF}$ is the frequency difference between the twin beams and ν_{HF} is the hyperfine splitting in the electronic ground state of ^{85}Rb shown in Fig. 5.2(b), L is the vapor cell length and c is the speed of light), $1 - \eta_p$ and $1 - \eta_c$ are the optical losses including imperfect detection quantum efficiencies in the probe and conjugate beam

paths respectively, α is the absorption we are interested in measuring, and $\hat{\nu}_p$, $\hat{\nu}_c$ and $\hat{\nu}_\alpha$ are the vacuum/noise operators. When a coherent state $|\beta\rangle$, $\beta = |\beta|e^{i\phi}$, where ϕ is the input phase, seeds mode a , and only vacuum fluctuations $|0\rangle$ seed mode b , then the input state can be written as $|\beta, 0, 0, 0, 0\rangle$, where the third, fourth and fifth zeros are the inputs for the vacuum/noise operators $\hat{\nu}_p$, $\hat{\nu}_c$ and $\hat{\nu}_\alpha$ respectively. Although not trivial, it is fairly straightforward to calculate the number operators $\hat{N}_a = \hat{a}_f^\dagger \hat{a}_f$ and $\hat{N}_b = \hat{b}_f^\dagger \hat{b}_f$ for the probe and conjugate beams after detection. Since the sample is placed in the probe beam, and the conjugate beam is used as a reference, we adopt the photon counts difference $\langle \hat{S}_\alpha \rangle = \langle \hat{N}_a - \hat{N}_b \rangle$ as our measurement signal. Note that this double-beam approach is commonly implemented in imaging and spectroscopy applications involving weak absorption [72, 73], because it enables the cancellation of classical super-Poissonian noise and provides a direct measurement of the absorption by instantaneous comparison with the unperturbed reference beam. The measurement sensitivity,

$$\Delta\alpha = \frac{\sqrt{\langle \Delta^2 \hat{S}_\alpha \rangle}}{|\partial_\alpha \langle \hat{S}_\alpha \rangle|}, \quad (4.2)$$

can then be readily obtained. In this article we define the quantum advantage as the ratio of the sensitivity enabled by the squeezed light, $\Delta\alpha_{\text{sqz}}$, to the one acquired from the coherent light, $\Delta\alpha_{\text{snl}}$, with the same amount of average photon numbers $\langle N_a \rangle$ and $\langle N_b \rangle$ as the bright twin beams:

$$\text{Quantum Advantage [dB]} = 10 \times \log_{10} \frac{\Delta\alpha_{\text{sqz}}}{\Delta\alpha_{\text{snl}}}. \quad (4.3)$$

In Fig. 4.1 we plot the theoretical quantum advantage for absorption $\alpha = 5\%$ as a function of optical transmission in the probe beam path η_p and conjugate beam path η_c . The squeezing parameter $r = 1.1$, which is calculated from the two-mode squeezing of 6.5 dB measured by near-perfect photodiodes (see Fig. 5.2(c) and the ‘‘Methods’’ section for details of the squeezing measurement) [80]. It is clear noticeable from the graph that if one could manage to curb the optical loss in both beam paths to be within 10 %, more than 3 dB quantum advantage for the measurement sensitivity would be readily achievable.

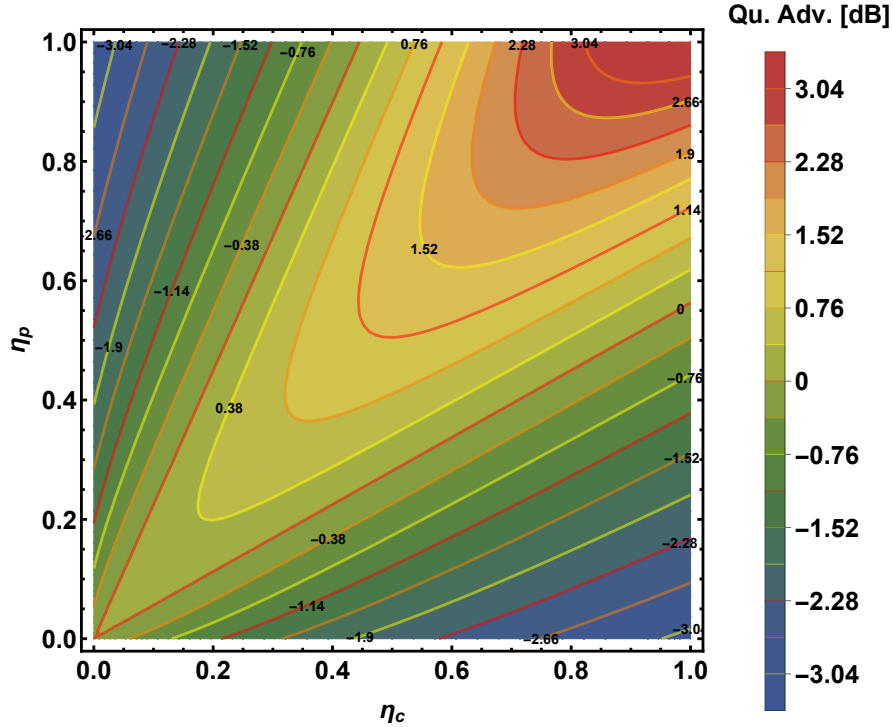


Figure 4.1: Theoretical prediction for the quantum advantage (Qu. Adv.) for absorption $\alpha = 5\%$ as a function of optical transmission in the probe beam path η_p and conjugate beam path η_c . The squeezing parameter $r = 1.1$ corresponds to 6.5 dB two-mode squeezing.

4.3 Experimental demonstration of the quantum advantage

In this article, we report an experimental scheme for a direct absorption measurement using bright squeezed light as the probe to demonstrate clear quantum advantage over the SNL. The bright squeezed light is generated with the FWM process in an atomic ^{85}Rb vapor cell [76–82].

The experimental setup and the respective ^{85}Rb atomic level structure are shown in Fig. 5.2(a) and (b). The atomic medium is pumped by a strong (~ 500 mW) narrow-band continuous-wave (CW) laser at frequency ν_1 ($\lambda = 795$ nm) with a typical linewidth $\Delta\nu_1 \sim 100$ kHz. Applying an additional weak (~ 10 nW) coherent seed beam at frequency $\nu_p = \nu_1 - (\nu_{HF} + \delta)$, where ν_{HF} and δ are the hyperfine splitting in the electronic ground state of ^{85}Rb and the two-photon

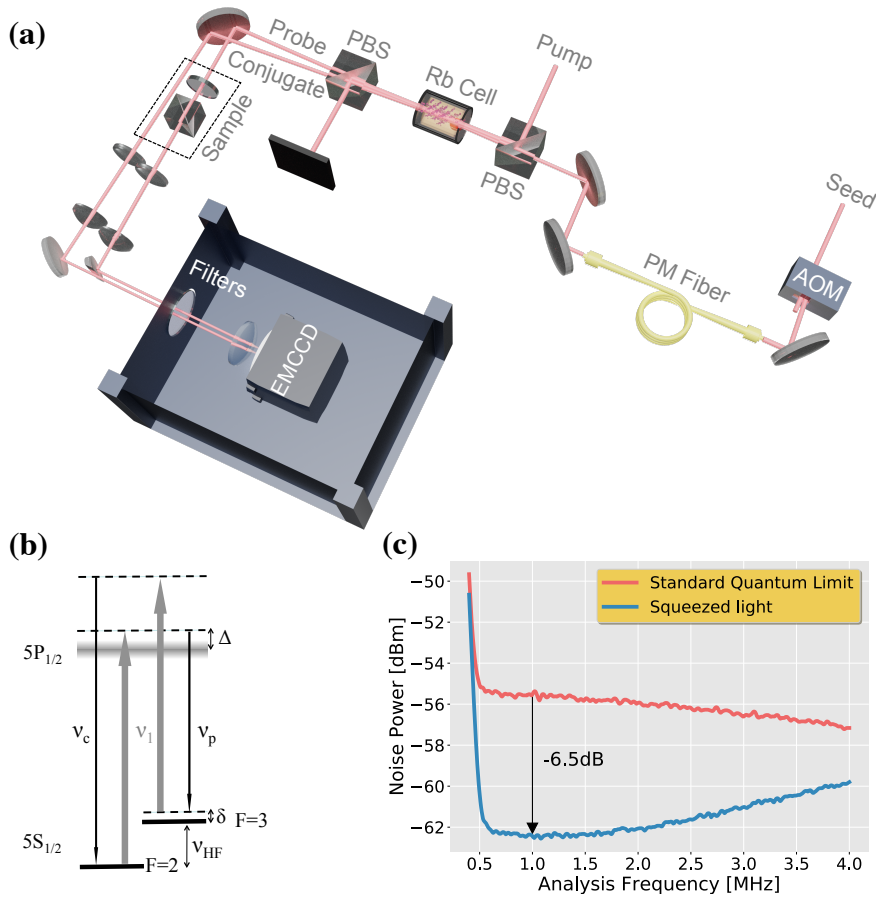


Figure 4.2: (a) Experimental setup in which a seeded ^{85}Rb vapor cell produces strong quantum-correlated twin beams via FWM. The twin beams are separated from the pump by a $\sim 2 \times 10^5 : 1$ polarizer after the cell. The probe beam passes through an absorption ‘sample’ (i.e., a combination of a $\lambda/2$ plate and a PBS) while the conjugate beam serves as a reference, before they are focused onto an EMCCD camera. The camera is enclosed in a light-proof box with filters mounted to block ambient light. The AOM in the probe beam path is used to pulse the twin beams with $2 \mu\text{s}$ FWHM and duty cycle of $1/12$. PBS: polarizing beam splitter, PM fiber: polarization-maintaining fiber. (b) Level structure of the D1 transition of ^{85}Rb atom. The optical transitions are arranged in a double- Λ configuration, where ν_p , ν_c and ν_1 stand for probe, conjugate and pump frequencies, respectively, fulfilling $\nu_p + \nu_c = 2\nu_1$. The width of the excited state in the level diagram represents the Doppler broadened line. Δ is the one-photon detuning, δ is the two-photon detuning, and ν_{HF} is the hyperfine splitting in the electronic ground state of ^{85}Rb . (c) Measured intensity-difference noise power spectrum for the squeezed twin beams (blue line) and for the SNL (red line), obtained with a radio frequency spectrum analyzer (with resolution and video bandwidth of 300 kHz and 100 Hz, respectively). A squeezing of 6.5 dB is achieved.

detuning respectively in Fig. 5.2(b) (further experimental details can be found in the “Methods” section), two pump photons are converted into a pair of twin photons, namely ‘probe ν_p ’ and ‘conjugate ν_c ’ photons, adhering to the energy conservation $2\nu_1 = \nu_p + \nu_c$ (see the level structure in Fig. 5.2(b)). The resulting bright twin beams are strongly quantum-correlated and are also referred to as bright two-mode squeezed light [84]. As can be seen from Fig. 5.2(c), the twin beams exhibit a intensity-difference squeezing of 6.5 dB measured by balanced photodiodes, which is indicative of strong quantum correlations [84] (see the “Methods” section for further details on the squeezing measurement).

After the ^{85}Rb vapor cell, the pump and the bright twin beams are separated by a second polarizer, with $\sim 2 \times 10^5 : 1$ extinction ratio for the pump. The probe beam transverses through a combination of a $\lambda/2$ plate and a PBS, acting as an absorption sample, while the conjugate beam serves as a reference. The twin beams are then focused onto an EMCCD camera (Andor iXon Ultra 897). The EMCCD camera is enclosed in a light-proof box with filters installed at the entrance to block ambient light photons from entering the camera. The acousto-optic modulator (AOM) in the probe beam path is used to pulse the beam with $2 \mu\text{s}$ duration (FWHM) and duty cycle of $1/12$. Since the CW pump beam is present all the time, the conjugate beam is therefore also pulsed as a result of the FWM process. The time sequencing of the pump and the twin beams are shown in Fig. 4.3(a) as the red strap, and the blue and green squares respectively.

We first measure the two-mode squeezing in a conventional way, i.e., using photodiodes to register intensity fluctuations in the beams of light in the temporal domain. After the second polarizer, we direct the probe and conjugate beams into the two ports of a balanced, amplified photodetector with a transimpedance gain of 10^5 V/A and 94% quantum efficiency at $\lambda = 795 \text{ nm}$ (not shown in Fig. 5.2(a)). The photodetector signals are sent to a radio frequency spectrum analyzer with a resolution bandwidth RBW of 300 kHz and a video frequency bandwidth VBW of 100 Hz. A typical squeezing spectrum is shown in Fig. 2.5 as the blue curve. The standard quantum limit (red curve) of this system is measured by picking off the probe before the cell, splitting it with a 50/50 non-polarizing beam splitter, and directing the resulting beams into the balanced, amplified

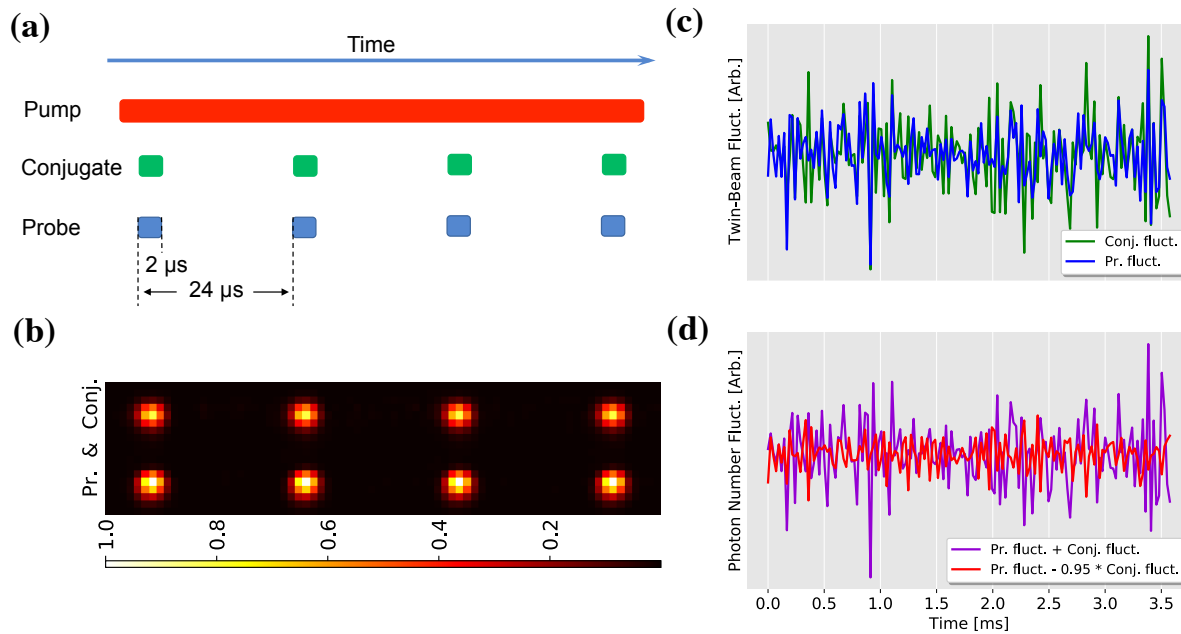


Figure 4.3: (a) Time sequencing of the pump and twin beams. The pulse duration of $2 \mu\text{s}$ and duty cycle of $1/12$ is realized by pulsing the probe beam with an AOM. The CW pump beam is present all the time. (b) Typical images of the twin beams with absorption $\alpha = 3 \%$ captured by the EMCCD camera. This subfigure is the ‘real life’ version of subfigure (a). It is an image of four consecutive pulses with the pulse width and duty cycle shown in subfigure (a). (c) Temporal photon counts fluctuations of the probe $N_p(t)$ and conjugate $N_c(t)$ obtained by integrating the photon counts in the cropped regions in (b). Clear similarities can be observed between the twin beams. (d) The strong noise reduction in the subtraction as opposed to the summation of the $N_p(t)$ and $N_c(t)$ depicted in (c) showcases strong correlations between them.

photodetector. The balanced detection technique subtracts away common-mode noise to better than 25 dB. The balanced photodetector noise level is a measure of the standard quantum limit for the total amount of optical power arriving at the photodetector. The standard quantum limit should be independent of frequency, which is indeed the case within the bandwidth of the detection electronics, which begins to drop down above 3 MHz. We measure more than 6 dB of the two-mode squeezing around the analysis frequency of 1 MHz.

We acquire the temporal behavior of the bright twin beams through the use of the *kinetic* mode of the EMCCD camera. The EMCCD has 512×512 pixels with each pixel size of $16 \mu\text{m} \times 16 \mu\text{m}$. We focus the twin beams on the camera with an $1/e^2$ beam diameter of $\sim 50 \mu\text{m}$, occupying roughly 3 pixels as shown in Fig. 4.3(b). The temperature of the EMCCD is kept low ($< -65^\circ\text{C}$) to curb the thermal noise contributions. The rest of the EMCCD camera settings can be found in the “Methods” section.

Since the pulse duration is $2 \mu\text{s}$ and the time interval between two consecutive pulses is $24 \mu\text{s}$, thus in order to completely transfer all charges from the camera’s image area to the storage area within one pulse cycle, we can in principle choose to set the speed of vertical pixel shift (i.e., the time taken to vertically shift all pixels one row down) to any value as long as it is faster than $4 \mu\text{s}$, given our beam size is merely 3 pixels across. However, the drawback with a fast vertical pixel shift speed is the reduction of charge transfer efficiency, which in turn causes ‘vertical smearing’ (i.e., light is still falling on the image area during the short time taken to transfer the charge from the image area to the storage area). In our case, we found a $0.9 \mu\text{s}$ vertical pixel shift speed in conjunction with a vertical clock voltage amplitude of 4 (to ensure that extremely high signals can be fully removed during the EMCCD clean cycle) worked best for us.

Another important setting of the EMCCD is the readout rate. It also ought to be fast enough to be within one pulse cycle. However, a faster readout rate always results in a higher readout noise. In our case, we adopt 3 MHz as our readout rate although technically it can be as fast as 17 MHz, but the price one has to pay is 8 fold more readout noise.

4.4 Results and Analysis

For each absorption α (acquired by changing the angle of the $\lambda/2$ plate), we capture 200 kinetic series, i.e., 200 frame sequences, with each frame having 35 pairs of probe and conjugate images containing the desired absorption information. We then crop a 10×10 pixel region around the maximum-intensity area in each probe and conjugate images, large enough to enclose their respective full beam profiles (see Fig. 4.3(b)), we thus can obtain the average total number of photons in the probe beam \bar{N}_p and in the conjugate beam \bar{N}_c by integrating photon counts in the cropped regions.

The measurement signal S_α is defined as the photon number difference between the probe and conjugate beams:

$$S_\alpha \equiv \bar{N}_p - \bar{N}_c = (1 - \alpha)\bar{N}_{p0} - \bar{N}_c, \quad (4.4)$$

where \bar{N}_{p0} and \bar{N}_p are the average numbers of photons in the probe beam before and after the faint absorber respectively, and \bar{N}_c is the average number of photons in the conjugate beam. Factoring out α , we have

$$\alpha = -\frac{1}{\bar{N}_{p0}}S_\alpha + \frac{S_0}{\bar{N}_{p0}}, \quad (4.5)$$

where $S_0 \equiv \bar{N}_{p0} - \bar{N}_c$ is the photon number difference of the twin beams without the presence of the absorber, which can be treated as a characteristic of the quantum light source itself.

Also, the relation between the uncertainties of absorption α and the measurement signal S_α can be derived from the error propagation formula (see Eq. (4.2)):

$$\Delta\alpha = \frac{\Delta S_\alpha}{|\partial_\alpha S_\alpha|} = \frac{1}{\bar{N}_{p0}}\Delta S_\alpha, \quad (4.6)$$

where $|\partial_\alpha S_\alpha| = \bar{N}_{p0}$ is obtained from Eq. (4.4). Therefore following Eqs. (4.5) and (4.6), the absorption α and its sensitivity $\Delta\alpha$ can be readily obtained from the measurements of S_α and

ΔS_α .

In Fig. 4.4, we plot the actual absorption α as a function of the measurement signal S_α . The inset in Fig. 4.4 is a zoom-in view of the first four data points to illustrate the sizes of uncertainties of these two quantities, i.e., ΔS_α on the x -axis and $\Delta\alpha$ on the y -axis. In the experiment, we observe 1.3 ± 0.2 dB quantum advantage in terms of ΔS_α when comparing to shot-noise limited classical measurements for faint absorption levels (see Fig. 4.6). Due to the fact that $\Delta\alpha \propto \Delta S_\alpha$ with $1/\bar{N}_{p0}$ be the proportionality constant (see Eq. (4.6)), this greater than 1 dB quantum advantage should also translate to $\Delta\alpha$ when compared to its shot-noise limited classical counterparts.

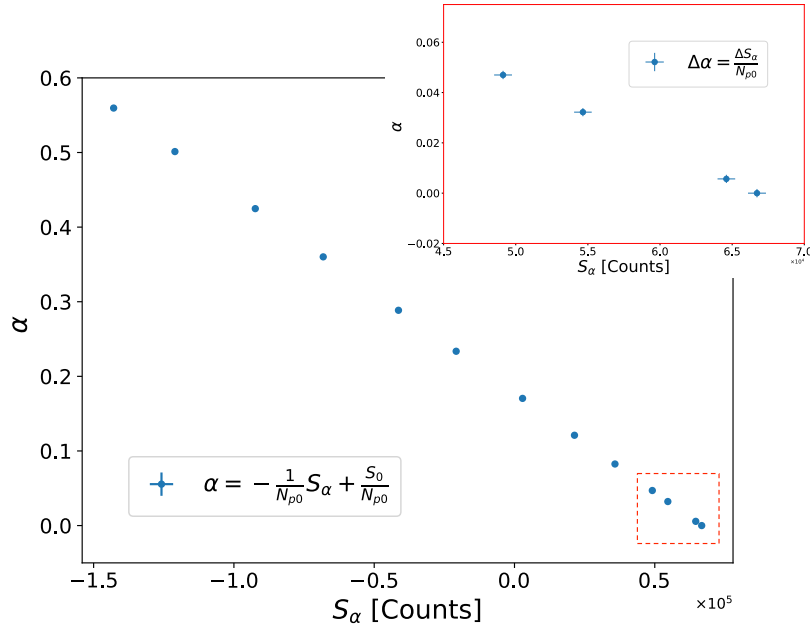


Figure 4.4: Actual absorption α as a function of the measurement signal S_α defined in Eq. (4.4). The inset is a zoom-in view of the first four data points to illustrate the sizes of x and y uncertainties.

For measurements of the quantum noise reduction between the bright twin beams, we adopt an algorithm originally developed in the spatial domain [74, 75] but re-deriving it in the temporal domain. As shown in Fig. 4.3(c), the temporal photon counts fluctuations of the probe beam $N_p(t)$

and conjugate beam $N_c(t)$ are acquired by integrating photon counts in the cropped 10×10 pixel regions for 7000 pairs of twin-beam images during 170 ms. In brief we crop a 10×10 pixel region around the maximum-intensity area in each probe and conjugate images, large enough to enclose their respective full beam profiles (see Fig. 4.3(b)), we then are able to obtain the temporal photon counts fluctuations of the probe $N_p(t)$ and conjugate $N_c(t)$ as shown in Fig. 4.3(c) by integrating the photon counts in the cropped regions. As expected, strong correlations between the photon counts fluctuations of the bright twin beams can be observed in Fig. 4.3(c) and manifested in Fig. 4.3(d) through the subtraction and addition of these two modes. The quantum noise reduction characterization, σ , in the temporal domain reads

$$\sigma \equiv \frac{\langle \Delta^2[(N_p(t + \delta t) - N_p(t)) - \eta(N_c(t + \delta t) - N_c(t))] \rangle_t}{\langle N_p(t + \delta t) + N_p(t) + \eta N_c(t + \delta t) + \eta N_c(t) \rangle_t}, \quad (4.7)$$

where $N_p(t + \delta t) - N_p(t)$ and $N_c(t + \delta t) - N_c(t)$ are the subtractions of photon counts in the cropped regions in two successive probe and conjugate images with time interval of $\delta t = 24 \mu\text{s}$. Since intensities of the twin beams are inherently imbalanced due to the seed power and different transmissions through the vapor cell [80], a scaling factor $\eta = 0.95$, which is obtained by taking the ratio between the conjugate and probe photon counts in the analysis regions without the presence of the absorption sample, is applied to the conjugate mode to rescale its photon count before the two modes are subtracted. The scaling factor effectively eliminates the DC portions of the Gaussian profiles of the probe and conjugate images. The subtraction of the two successive images leads to the cancellation of the low-frequency portion of the classical noise as well as the individual common Gaussian profiles of the probe and conjugate images [74, 75]. The numerator of Eq. (4.7) represents the temporal variance of the intensity-difference noise between the probe and conjugate pulses. The denominator gives the mean photon counts for the probe and conjugate pulses used for the analysis and represents the shot noise. For coherent state pulses $\sigma = 1$, which corresponds to the SNL, while for thermal light or other classical states $\sigma > 1$. Temporally quantum-correlated beams, like the bright twin beams generated in our experiment, will result in $\sigma < 1$, with a smaller

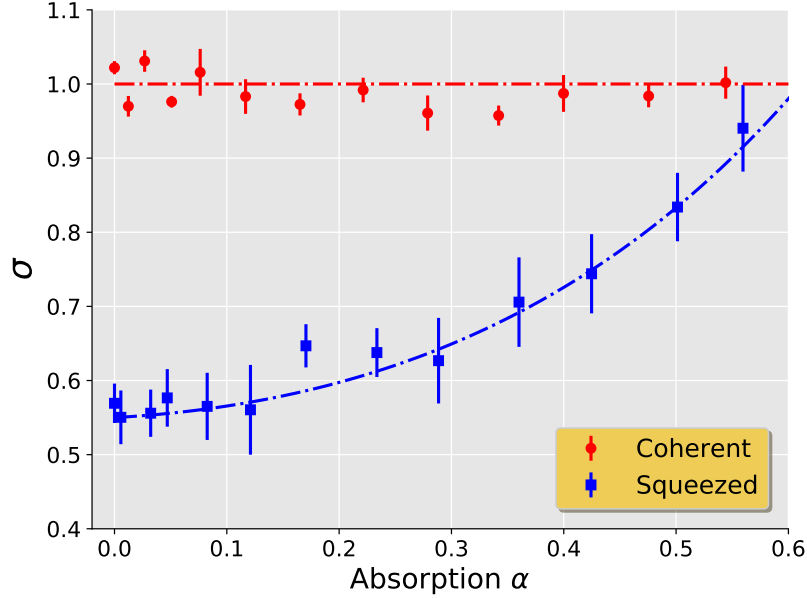


Figure 4.5: Temporal quantum noise reduction σ as a function of absorption α for the bright squeezed light (blue squares) and coherent light (red dots). Dashed blue line is the theoretical prediction with $\eta_p = 0.61$, $\eta_c = 0.63$ and $r = 1.1$.

σ corresponding to a larger degree of quantum correlations (i.e., two-mode squeezing).

In Fig. 4.5, we plot σ as a function of absorption α for the squeezed light together with coherent light. For each α , we average 5 sets of 200 kinetic series and designate the error bar with one standard deviation. As expected, $\sigma < 1$ for the squeezed light (blue squares), while $\sigma \cong 1$ when the bright twin beams are replaced with two coherent beams (red dots). The notable degradation of the temporal quantum noise reduction measured by the EMCCD camera with respect to the one measured by balanced photodiodes in Fig. 5.2(c) can be mainly attributed to a much worse common noise rejection (caused by the mismatch between the spatial modes of the twin beams as shown in Fig. 4.3(b)) and a much worse quantum efficiency of the EMCCD at 795 nm (merely 70 % as opposed to at least 94 % for photodiodes). We also repeated the experiment with different pulse duty cycles (i.e., δt in Eq. (4.7)), but they seemed to play a nonessential role on the quantum noise reduction as long as we were in the shot-noise-limited regime, i.e., σ is still close to unity for

coherent beams.

From Eqs. (4.2) and (4.3) we can easily arrive at

$$\text{Quantum Advantage [dB]} = 10 \times \log_{10} \frac{\Delta\alpha_{\text{sqz}}}{\Delta\alpha_{\text{snl}}} = 10 \times \log_{10} \sqrt{\frac{\langle \Delta^2 \hat{N}_\alpha \rangle_{\text{snl}}}{\langle \Delta^2 \hat{N}_\alpha \rangle_{\text{sqz}}}} = 10 \times \log_{10} \sqrt{\frac{1}{\sigma}}. \quad (4.8)$$

We thus can use the same data depicted in Fig. 4.5 to plot the quantum advantage versus absorption α . The results are shown in Fig. 4.6. Theoretical predictions for the temporal quantum noise reduction characterization σ and the quantum advantage as a function of absorption α are plotted as dashed blue lines in Figs. 4.5 and 4.6, where excellent agreements between experiment and theory can be seen. At those faint absorption levels ($\alpha \leq 10\%$) in Fig. 4.6, the observed quantum advantage can be more than 1.2 dB, although *total* optical losses (including the transmission loss imposed by optics and imperfect detection quantum efficiency imposed by the EMCCD camera) in the paths of the twin beams are significant - nearly 39 % in the probe path and nearly 37 % in the conjugate path. This is mainly due to a relatively low quantum efficiency of the EMCCD camera at 795 nm ($\sim 70\%$) and imperfect transmission of the band pass filters ($\sim 94\%$) mounted in front of the light-proof box. If we were able to overcome this main obstacle of the experiment by employing a much more efficient camera, we would have a much higher quantum advantage as implied by the theoretical curves in Fig. 4.1.

It is worth mentioning that taking measurements using photodetectors would yield better results due to photodiodes' much higher quantum efficiency. However, the main drawback of using photodetectors is their much higher power requirement. For an EMCCD camera, a few nW input power is more than enough to yield a clear signal-to-noise ratio, however, for a photodetector to provide sufficient signal clearance from its electronic noise floor, the input power has to be in the range of tens of μW . For example in our experiment, in order to have a signal noise power that is 10 dB above the electronic noise floor, we have to shine a coherent beam of light of at least 50 μW to

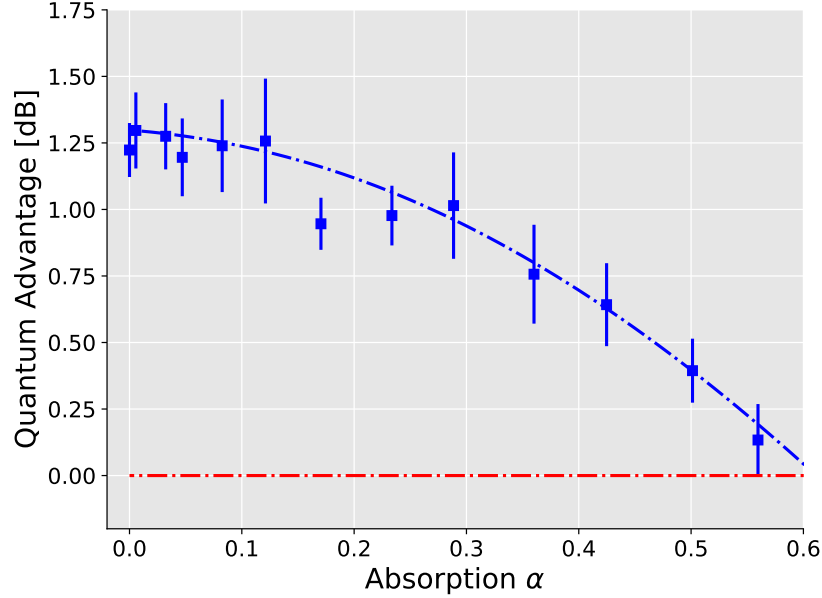


Figure 4.6: Quantum advantage as a function of absorption α . Dashed blue line is the theoretical prediction with $\eta_p = 0.61$, $\eta_c = 0.63$ and $r = 1.1$. The quantum advantage is only significant (> 1 dB) for small values of α ($< 20\%$), and for $\alpha > 60\%$ there is no quantum advantage.

the photodetector (given our squeezing level of 6.5 dB, that implies a merely 3.5 dB clearance from the electronic noise floor for $50 \mu\text{W}$ squeezed light). One of the most important implementations of our experimental scheme is to characterize biological samples without imposing light-induced damages, a much higher input light power would hence defeat this purpose.

4.5 Discussion

Overall, our experiment realizes a practical scheme that allows the SNL in the direct absorption measurement to be overcome. We demonstrate that by using the bright squeezed light more than 1.2 dB quantum advantage is achieved for the measurement sensitivity at faint absorption levels ($\leq 10\%$). We thus experimentally demonstrate the advantage of quantum light for measurements on open systems. We also theoretically demonstrate that more quantum advantage (> 3 dB) is very likely attainable by means of a proper optical loss management. We use FWM in an atomic

^{85}Rb vapor cell to generate the quantum-correlated twin beams of light. It is also the first experiment that uses quantum light generated with FWM instead of SPDC to demonstrate a sub-shot-noise absorption measurement. Major advantages of this FWM-based quantum light generation scheme include an ultra-high photon-pair flux up to 10^{16} photons/s, which is a few orders of magnitude higher than the fluxes produced by SPDCs [151–153], and narrow-band probe and conjugate beams (~ 20 MHz) [82, 86], which can be readily integrated into quantum networks through coupling with micro-resonators/cavities. Also, although the small bandwidth feature of the twin beams is not used in the experiment, we do take advantage of it by making a ‘single-mode’ approximation for the twin beams in the theoretical analysis. The fact that our experimental results agree very well with the theory based on the ‘single-mode’ approximation confirms the importance of the narrow band feature of the twin beams. Moreover, the FWM process offers sufficient gains in a single-pass configuration producing bright quantum-correlated beams of light without a cavity, making it possible to preserve the multi-spatial-mode nature of the bright twin beams [89, 90]. Our quantum light generation together with the direct absorption measurement scheme reported here can be therefore greatly beneficial to many applications involving characterizing chemical and biological samples, where the sub-SNL absorption measurements are highly desirable [154, 155].

4.6 Methods

Experimental details for the bright squeezed light generation

In this work an external cavity diode laser and a tapered amplifier (a combo system manufactured by Toptica Photonics with item number TA Pro 795) is used as the laser source with a typical linewidth of 100 kHz ($5 \mu\text{s}$), to generate a strong ($\sim 400 - 800$ mW) pump beam near the D1 line of Rb (795 nm). A weak seed beam is diverted from the pump and ~ 3 GHz red-detuned by double-passing an 1.5 GHz acousto-optic modulator (Brimrose TEF-1500-100-795 driven by a RF synthesizer manufactured by Hewlett-Packard with item number 8642B). This results in a very good relative phase stability of the seed with respect to the pump. The pump and seed beams are

combined in a Glan-Taylor polarizer and directed at an angle of 0.3° to each other into a 12.5 mm long vapor cell filled with isotopically pure ^{85}Rb (Precision Glassblowing TG-ABRB-I85-Q). The pump and seed beams are collimated with waists at the position of the cell center of $700\ \mu\text{m}$ and $400\ \mu\text{m}$ $1/e^2$ radius, respectively. The cell, with no magnetic shielding, is heated to $112\ ^\circ\text{C}$. The windows of the cell are antireflection coated on both faces, resulting in a transmission for the seed beam of $\sim 98\ \%$ per window at room temperature.

After the cell, the pump and the twin beams (‘probe’ and ‘conjugate’) are separated by a second polarizer, with $\sim 2 \times 10^5 : 1$ extinction ratio for the pump. The pump at frequency ν_1 is blue-tuned by a ‘one-photon detuning Δ ’ of 900 MHz with respect to the ^{85}Rb $5S_{1/2}, F = 2 \rightarrow 5P_{1/2}$, D1 transition (see Δ depicted in Fig. 5.2(b)). The seed at frequency ν_p is red-detuned from the pump by $(3036\ \text{MHz} + \delta)$, where δ is the ‘two-photon detuning’ and typically a few MHz (see δ depicted in Fig. 5.2(b)), which can be adjusted by changing the radio frequency that drives the 1.5 GHz AOM. These detunings result in an intensity gain on the seed of 3.5, and the resulting beam is referred to as the ‘probe’ beam. The gain is accompanied by the generation of a ‘conjugate’ beam at frequency ν_c , blue-detuned from the pump by $(3036\ \text{MHz} + \delta)$. It has the same polarization as the probe beam, and propagates at the pump-seed angle on the other side of the pump so that it satisfies the phase-matching condition.

4.6.1 Squeezing measurement

To measure the squeezing between the twin beams, after the second polarizer the probe and conjugate beams are directed into the two ports of a balanced, amplified photodetector with a transimpedance gain of $10^5\ \text{V/A}$ and at least 94% quantum efficiency at $\lambda = 795\ \text{nm}$. The photodetector signals are sent to a radio frequency spectrum analyzer with a resolution bandwidth RBW of 300 kHz and a video bandwidth VBW of 100 Hz.

A typical squeezing spectrum is shown in Fig. 5.2(c). The standard quantum limit (blue curve) of this system is measured by picking off the probe before the cell, splitting it with a 50/50 non-polarizing beam splitter, and directing the resulting beams into the balanced, amplified photode-

detector. The balanced detection technique subtracts away common-mode noise to better than 25 dB. The balanced photodetector noise level is a measure of the standard quantum limit for the total amount of optical power arriving at the photodetector. The standard quantum limit should be independent of frequency, which is indeed the case within the bandwidth of the detection electronics, which begins to drop down above 3 MHz.

4.6.2 EMCCD camera settings

Since our pulse duration is $2 \mu\text{s}$ and the time interval between two consecutive pulses is $24 \mu\text{s}$, thus in order to completely transfer all charges from the camera's image area to the storage area within one pulse cycle, we can in principle choose to set the speed of vertical pixel shift (i.e., the time taken to vertically shift all pixels one row down) to any value as long as it is faster than $4 \mu\text{s}$, given our beam size is merely 3 pixels across. However, the drawback with a fast vertical pixel shift speed is the reduction of charge transfer efficiency, which in turn causes 'vertical smearing' (i.e., light is still falling on the image area during the short time taken to transfer the charge from the image area to the storage area). In our case, we found a $0.9 \mu\text{s}$ vertical pixel shift speed in conjunction with a vertical clock voltage amplitude of 4 (to ensure that extremely high signals can be fully removed during the EMCCD clean cycle) worked best for us.

Another important setting of the EMCCD is the readout rate. It also ought to be fast enough to be within one pulse cycle. However, a faster readout rate always results in a higher readout noise. In our case, we adopt 3 MHz as our readout rate although technically it can be as fast as 17 MHz, but the price one has to pay is 8-fold more readout noise.

5. SQUEEZED LIGHT INDUCED TWO-PHOTON ABSORPTION FLUORESCENCE OF FLUORESCEIN BIOMARKERS *

Two-photon absorption (TPA) fluorescence of biomarkers has been decisive in advancing the fields of biosensing and deep-tissue *in vivo* imaging of live specimens. However, due to the extremely small TPA cross section and the quadratic dependence on the input photon flux, extremely high peak-intensity pulsed lasers are imperative, which can result in significant photo- and thermal damage to biological specimen. Previous works on entangled TPA (ETPA) with spontaneous parametric down-conversion (SPDC) light sources found a linear dependence on the input photon-pair flux, but are limited by low optical powers, along with a very broad spectrum. We report that by using a high-flux two-mode squeezed light source for TPA, a fluorescence enhancement of ~ 47 is achieved in fluorescein biomarkers as compared to classical TPA with CW excitation. Moreover, a polynomial behavior of the TPA rate is observed in the DCM laser dye.

In a two-photon process, those two photons of the initial radiation get annihilated to generate the non-linear effect. Thus, the generated field via two-photon process scales as the normal ordered 2^{nd} order moment of the input photon number, which is the second order correlation $G^{(2)}$. We will have a short theoretical discussion on two-photon absorption processing based on second-order perturbation.

5.1 Second-order perturbation theory for two-photon process

Here, our consideration is in the dipole approximation, and the quadratic effects in the vector potential of the field is ignored. So, the Hamiltonian of atom and field interaction is given by [157],

*Part of this chapter is reprinted from Ref. [156] (Tian Li, Fu Li, Charles Altuzarra, Anton Classen and Girish S. Agarwal, "Squeezed light induced two-photon absorption fluorescence of fluorescein biomarkers", Appl. Phys. Lett. 116, 254001 (2020)) with permission from AIP Publishing.

$$H(t) = \frac{e}{mc} \hat{p}(t) \cdot \hat{A}(t) \quad (5.1)$$

where $\hat{p}(t)$ is the momentum operator of the valence electron, and $\hat{A}(t)$ is the vector potential of the field. The vector has two frequencies, positive one and negative one, which read

$$\hat{A}(t) = \hat{a}(t) + \hat{a}^\dagger(t) \quad (5.2)$$

with $\hat{a}(t) = \sqrt{\frac{\hbar c^2}{2V}} \sum w_k^{-1/2} \hat{\epsilon}_k \hat{a}_k e^{-i w_k t}$. The \hat{a}_k , w_k and $\hat{\epsilon}_k$ are the annihilation operator, frequency and polarization vector, respectively, for the mode specified by the index k .

The time evolution of the state of the system of atom and field in the interaction picture given by the relation

$$U'(t) = 1 + \frac{1}{i\hbar} \int_0^t dt' H_I(t') \quad (5.3)$$

$$- \frac{1}{\hbar^2} \int_0^t \int_0^t dt_1 dt_2 \theta(t_1 - t_2) H_I(t_1) H_I(t_2), \quad (5.4)$$

where $U'(t)$ is the unitary time-development operator, and θ is the step function.

Let assume that atom is initially in its ground state $|g\rangle$, and field is initially in state $|\psi\rangle_i$. Thus, the probability that the atom has been excited to a given final state $|e\rangle$ at time t is

$$P(t) = \sum_{\varphi} \left| \langle \varphi | \langle e | U'(t) | g \rangle | \psi \rangle_i \right|^2 \quad (5.5)$$

The probability of two-photon absorption can be written as

$$\begin{aligned}
P_2(t) &= \sum_{\varphi} \left| \int_0^t \int_0^t dt_1 dt_2 \langle \varphi | \langle e | \hat{p}(t_1) \hat{p}(t_2) \hat{a}(t_1) \hat{a}(t_2) | g \rangle | \psi \rangle_i \right|^2 \\
&= \sum_{\varphi} \left| \int_0^t \int_0^t dt_1 dt_2 \langle \varphi | \hat{a}(t_1) \hat{a}(t_2) | \psi \rangle_i \varsigma(t_1, t_2) \right|^2 \\
&= \int_0^t \int_0^t \int_0^t \int_0^t dt'_1 dt'_2 dt_1 dt_2 \langle \psi |_i \hat{a}^\dagger(t'_1) \hat{a}^\dagger(t'_2) \hat{a}(t_1) \hat{a}(t_2) | \psi \rangle_i \varsigma(t_1, t_2) \varsigma^*(t'_1, t'_2) \\
&= \int_0^t \int_0^t \int_0^t \int_0^t dt'_1 dt'_2 dt_1 dt_2 \varsigma(t_1, t_2) \varsigma^*(t'_1, t'_2) G^{(2)}(t'_1, t'_2; t_1, t_2)
\end{aligned}$$

where atom related part $\varsigma(t_1, t_2)$ is

$$\varsigma(t_1, t_2) = \theta(t_1 - t_2) \left(\frac{e}{\hbar m c} \right)^2 \sum_j p_{ej} p_{jg} e^{-i(w_j - w_f)t_1 + i w_2 t_2} \quad (5.6)$$

and second correlation $G^{(2)}(t'_1, t'_2; t_1, t_2)$, which related to the incident photon, is written as

$$G^{(2)}(t'_1, t'_2; t_1, t_2) = \langle \hat{a}^\dagger(t'_1) \hat{a}^\dagger(t'_2) \hat{a}(t_1) \hat{a}(t_2) \rangle \quad (5.7)$$

Let R to be absorption rate, which is proportional to total interaction time. Thus, R is

$$P_2(t) = R \cdot t. \quad (5.8)$$

Finally, the absorption rate can be rewritten as [157]

$$R = 2 |g(w)|^2 \int_{-\infty}^{+\infty} dt e^{2i w_0 t - \Gamma |t|} G^{(2)}(-t, -t; t, t) \quad (5.9)$$

where

$$\theta(t) = \frac{i}{2\pi} \int dw \frac{e^{-iwt}}{w + i\epsilon},$$

$$\varsigma(t_1, t_2) = \frac{i}{2\pi} \int dw g(w) e^{-i(w_j - w_f)t_1 + iw_2 t_2},$$

$$g(w) = \left(\frac{e}{\hbar m c} \right)^2 \sum_j p_{ej} p_{jg} \frac{1}{w - w_j + i\epsilon}.$$

For a short-lived atom, the atomic lifetime is much shorter than any of the coherence times characteristic of the squeezed light. The P_2 (probability of two-photon absorption) will be approximately given by [158]

$$R = 2 |g|^2 G^{(2)}(0) \frac{\Gamma/2}{(\Gamma/2)^2 + (2w - w_0)^2} \quad (5.10)$$

where Γ is the width of the upper atomic level, w_0 is the atom frequency, g is a coupling constant, w is the laser frequency. The absorption rate depends on intensity fluctuations only, as given by $G^{(2)}(0)$, which is the correlation function with all its arguments equal.

For OPO light source, consider an ideal squeezed state consisting of a coherent component of intensity I_c and a Squeezed-vacuum part of intensity I_{sqz} , its second order correlation is

$$G^{(2)}(0) = I_c^2 + I_c \left[4I_{sqz} \pm (4I_{sqz}^2 + 2\gamma I_{sqz})^{1/2} \right] + 3I_{sqz}^2 + \frac{1}{2}\gamma I_{sqz} \quad (5.11)$$

where γ is the cavity decay, the plus and minus signs hold for phase and amplitude squeezed light, respectively.

For pure squeezed vacuum, $I_c = 0$, we have

$$G^{(2)}(0) = 3I_{sqz}^2 + \frac{1}{2}\gamma I_{sqz} \quad (5.12)$$

It grows as I_{sqz} for weak fields, which means that two-photon absorption rate is linearly with the field intensity for weak fields.

Long-lived atom two photon absorption

For a long-lived atom, it's two photon absorption rate is the full integral of E.q.(5.9) [158]

$$\begin{aligned}
G^{(2)}(-t, -t; t, t) = & I_c^2 e^{-4iwt} \langle e^{-2i[\phi_c(t) - \phi_c(-t)]} \rangle \\
& - I_c e^{-2iwt} \langle e^{2i\phi_c(-t)} \hat{a}_{sqz}(t) \hat{a}_{sqz}(t) \rangle + \langle e^{-2i\phi_c(t)} \hat{a}_{sqz}^\dagger(-t) \hat{a}_{sqz}^\dagger(-t) \rangle \\
& + 2I_c e^{-2iwt} \langle e^{-i[\phi_c(t) - \phi_c(-t)]} \hat{a}_{sqz}^\dagger(-t) \hat{a}_{sqz}(t) \rangle \\
& + \langle \hat{a}_{sqz}^\dagger(t) \hat{a}_{sqz}^\dagger(t) \hat{a}_{sqz}(-t) \hat{a}_{sqz}(-t) \rangle
\end{aligned}$$

and

$$R = 2 |g|^2 \left[I_c \pm (I_{sqz}^2 + \gamma I_{sqz}/2)^{1/2} \right] \frac{\Gamma/2}{(\Gamma/2)^2 + (2w - w_0)} + \dots, \quad (5.13)$$

where ϕ_c is the phase of coherent light component.

Here, the absorption spectra for coherent light, light with squeezed-phase and light with squeezed-amplitude are compared. We know that the squeezed-amplitude light has best two-photon absorption rate, and squeezed-phase light has most weak two-photon absorption rate.

We will demonstrated experimentally that squeezed-amplitude light has enhancement of ~ 47 in fluorescein biomarkers as compared to classical coherent light.

Two-photon absorption (TPA) microscopy (with near-infrared illumination) is the method of choice for *in vivo* imaging of tissues down to millimeter depths [159]. It bears several advantages including intrinsic high 3-D resolution due to significant TPA occurring only in close vicinity to the focal volume, reduced out-of focus bleaching, highly reduced autofluorescence, and the capability of nearly aberration-free deep-tissue focusing along with reduced absorption [160–163], such as reduced out-of-focus photobleaching, less autofluorescence, deeper tissue penetration and in-

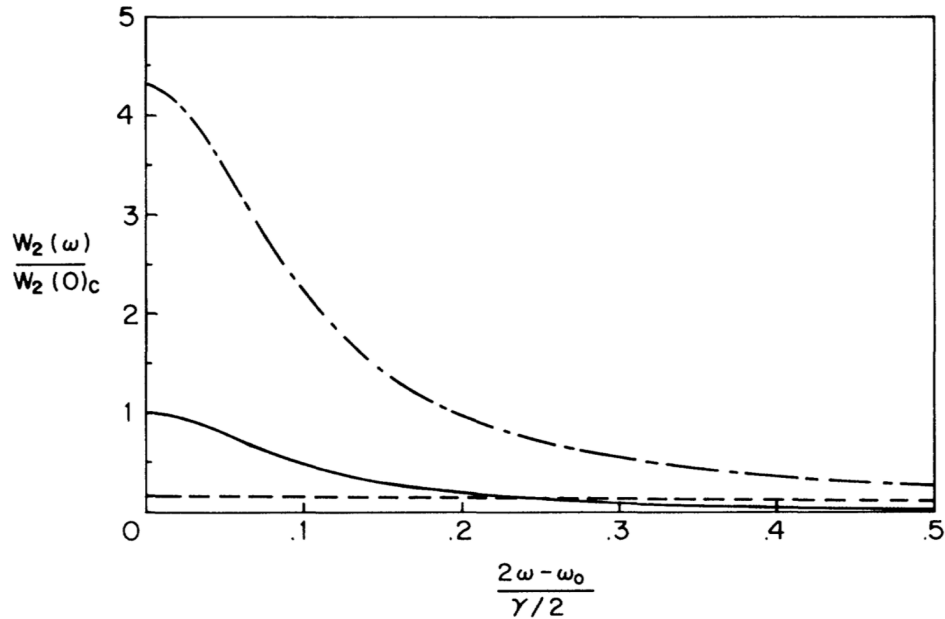


Figure 5.1: Absorption spectra for coherent light (solid line), light with squeezed-phase fluctuations (dashed line), and light with squeezed-amplitude fluctuations (dash-dotted line) [158]. The parameters chosen are $\Gamma = 0.1\gamma$, $2\epsilon/\gamma = 0.2$, and $I_c = 5 * I_{sqz}$.

trinsically high 3-dimensional resolution. Unfortunately, classical TPA is an extremely inefficient process with absorption cross sections δ_r on the order of $10^{-48} \text{ cm}^4 \cdot \text{s}/\text{photon}$ [164]. Therefore, TPA sensing and imaging generally requires the use of high-intensity pulsed lasers, to insure the near-simultaneous presence of two photons to induce the process [165, 166]. However, since the excitation pulse peak power is typically 10^5 times the average power, samples are prone to endure significant photo- and thermal damage [135, 142]. According to Xu *et al.* [165], the alternative of using CW as opposed to pulsed sources is problematic because a factor of 10^2 to 10^3 times more average power is required to yield the same amount of fluorescence signal as for pulsed excitations. However, since for a pulsed excitation the power *in each pulse* is typically 10^5 (in the order of $1/f\tau$, where f is the pulse repetition rate and τ is the excitation pulse width) times more than its average power, the energy in each pulse is still 10^2 to 10^3 times more than that of a CW excitation to acquire the same amount of fluorescence signal. Thus using a CW excitation can therefore

significantly reduce the risk of photodamaging, such as phototoxicity and photobleaching of the sample [135, 167], but unfortunately this option yields very little fluorescence.

In parallel, using the unique quantum energy-time entanglement characteristics of photon pairs generated by spontaneous parametric down-conversion (SPDC), the entangled TPA (ETPA) rate can be vastly enhanced [152, 153, 164, 168], with the absorption cross section σ_e for ETPA in the range of $10^{-18} - 10^{-22} \text{ cm}^2$. Most notably, the linear dependence of ETPA on the input photon-pair flux, which was first predicted by Gea-Banacloche [169] and Javanainen and Gould [170], was also verified experimentally ETPA shows a linear dependence on the input photon-pair flux [152, 153, 164, 168, 171, 172]. It is a major advantage over the quadratic dependence of classical TPA as the need for high intensity excitation becomes obsolete. However, most current ETPA implementations with biological specimen are limited by a low flux of $\sim 10^7$ photon pairs/s [152, 153, 164, 168], equivalent to only ~ 10 pW for near-infrared wavelengths, which is unviable for bioimaging and biosensing. This is mostly due to loss of correlation and difficulty of tuning biphoton wavelength in the nonlinear crystals. the low conversion efficiencies of the nonlinear crystals used to generate the entangled photon pairs. It has also been shown that ETPA is unique in that it follows a linear behavior, unlike the quadratic behavior specific to classical TPA. It is also worth mentioning that a much more efficient photon pair flux generation has been demonstrated by Jechow *et al.* using a type-0 quasi-phase-matched periodically-poled-lithium-niobate waveguide crystal Their photon-pair flux can be as high as $\sim 10^{11}$ photon pairs/s.

On the other hand, by using quantum-correlated photon pairs, the two-photon absorption rate can be vastly enhanced since the absorption process depends linearly rather than quadratically on the input photon-flux density [171–173]. Proof-of-principle experiments have already demonstrated the linear behavior with energy-time entangled photon pairs produced from spontaneous parametric down-conversion (SPDC) in a Barium Borate (BBO) crystal [153, 164, 168, 168]. Some fundamental experimental limitations include very low input entangled photon pair flux in the order of 10^7 photons/s, and very wide excitation linewidths. Moreover, none of the molecules would be particularly useful as fluorescent biomarkers in the two-photon absorption microscopy [160].

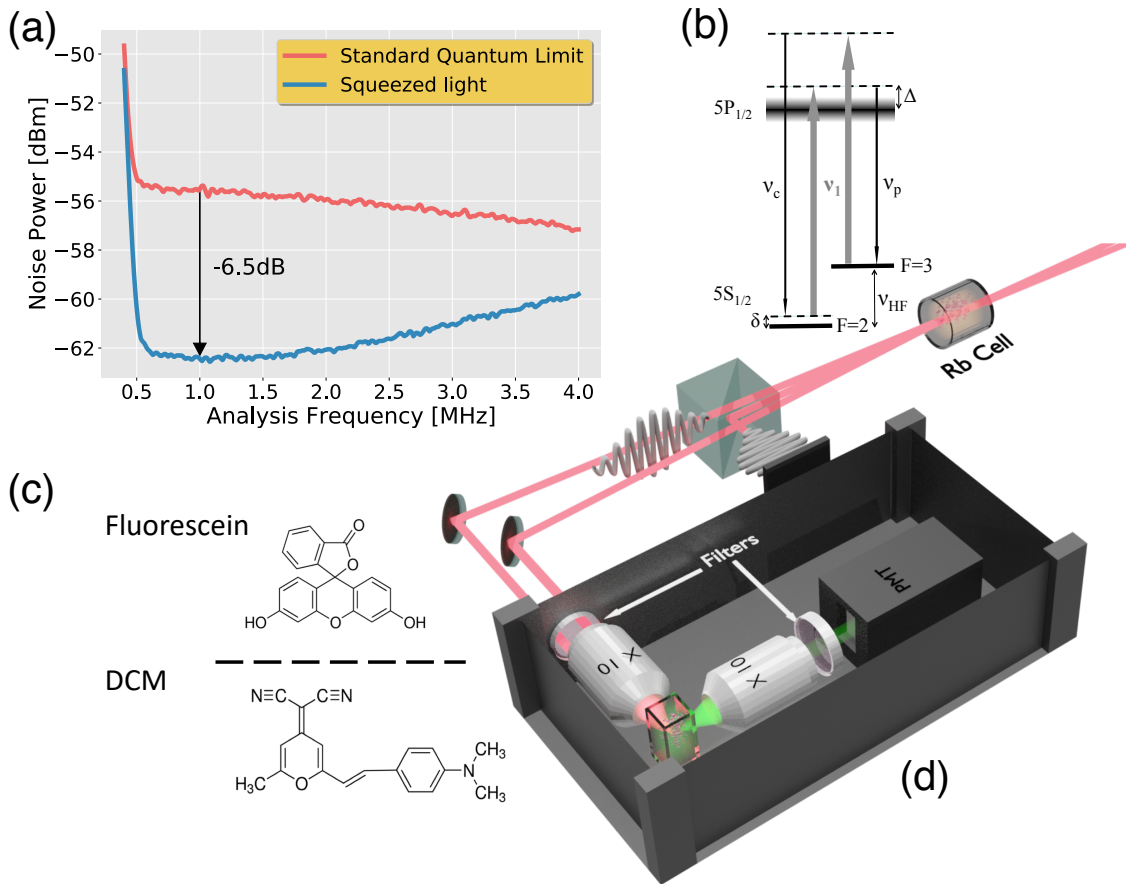


Figure 5.2: (a) Squeezed-light TPA setup in which a seeded ^{85}Rb cell produces strong quantum-correlated twin beams via FWM. The twin beams are focused onto the sample with a $10\times$ objective. Fluorescence is collected at an angle of 90° with a second $10\times$ objective and fed into a photomultiplier tube (PMT). Two short-pass filters in front of the PMT exclude stray pump photons. The setup is enclosed in a light-proof box. (b) Level structure of the D1 transition of ^{85}Rb atoms. The optical transitions are arranged in a double- Λ configuration, where ν_p , ν_c and ν_1 stand for probe, conjugate and pump frequencies, respectively, fulfilling $\nu_p + \nu_c = 2\nu_1$. The width of the excited state in the level diagram represents the Doppler broadened line. Δ is the one-photon detuning, δ is the two-photon detuning, and ν_{HF} is the hyperfine splitting in the electronic ground state of ^{85}Rb . (c) Measured intensity-difference noise power spectrum for the squeezed twin beams (blue line) and for the standard quantum limit (red line), obtained with a radio frequency spectrum analyzer (with a resolution and video bandwidth of 300 kHz and 100 Hz, respectively). A squeezing of 6.5 dB is achieved. (d) Molecular structures of DCM and fluorescein.

In this work, we utilize a different quantum light source that is based on the four-wave mixing (FWM) process in an atomic ^{85}Rb vapor cell [76–82]. The setup and the respective atomic level structure are shown in Fig. 5.2(a) and (b). The medium possesses a large third-order electric susceptibility $\chi^{(3)}$ and is pumped by a strong narrow-band continuous-wave (CW) laser at frequency ν_1 ($\lambda = 795$ nm) with a typical linewidth $\Delta\nu_1 \sim 100$ kHz. Applying an additional coherent CW seed beam at frequency $\nu_p = \nu_1 - (\nu_{HF} + \delta)$, where ν_{HF} and δ are the hyperfine splitting in the electronic ground state of ^{85}Rb and the two-photon detuning respectively in Fig. 5.2(b) (see the Supplementary Material for further experimental details), two pump photons are converted into a pair of twin photons, namely ‘probe ν_p ’ and ‘conjugate ν_c ’ photons, adhering to the energy conservation $2\nu_1 = \nu_p + \nu_c$ (see the level structure in Fig. 5.2(b)). The resulting “twin beams” are strongly quantum-correlated and are also referred to as (seeded) two-mode squeezed light [84]. Major advantages are narrow-band probe and conjugate beams (~ 20 MHz) [82, 86] along with a freely adjustable photon-pair flux between 10^{13} to 10^{16} photons/s [76, 77, 79–82], which is a few orders of magnitude higher than for SPDC. Also, since FWM in atomic vapors is an nonlinear parametric process based on ground-state coherences, in which the main advantage arises from small two-photon detunings from real states whereas in nonlinear crystals there is no real state to which the signal or idler photon is close, the generation of quantum correlations with FWM in atomic vapors can be therefore very efficient. As can be seen from Fig. 5.2(c), the twin beams exhibit a intensity-difference squeezing of 6.5 dB, which is indicative of strong quantum correlations [84] (see the Supplementary Material for further details of the squeezing measurement).

As can be seen from Fig. 5.2(a), the entangled photon pair flux of the source exhibits a strong intensity-difference squeezing of -6.5 dB, which is indicative of strong quantum correlations between the twin beams. Due to the much higher production of photon pairs in the squeezed light source and differently from the entirety of ETPA experiments governed by a low photon pair flux, we further report that the relationship between input power and fluorescence intensity with squeezed light follows a nonlinear behavior.

5.2 Experiment

In this study we analyze and compare classical TPA and squeezed-light induced TPA (SL-TPA) fluorescence rates in fluorescein and DCM (see the Supplementary Material for samples preparation). Fluorescein is one of the most frequently used biomarkers for bioimaging and biosensing [174]. Its small size is very convenient for *in vivo* imaging applications, although its relatively small classical TPA cross section generates low amounts of fluorescence [165, 166]. The SL-TPA setup is depicted in Fig. 5.2(a). A 10 \times objective (Thorlabs RMS10X) focuses the near-infrared excitation light onto a solution of fluorophores. Following TPA, fluorescence is collected by a second 10 \times objective (Thorlabs RMS10X) at an angle of 90 $^\circ$ and guided to a photo-multiplier tube (PMT) (Thorlabs PMTSS in conjugation with a PMT transimpedance amplifier Thorlabs TIA60). Two optical low-pass filters (Thorlabs FESH0750) exclude stray pump photons. The measured PMT voltage outputs (see inset in Fig. 5.3) are converted into fluorescence rates of arbitrary units (since the PMT's response to an input photon is an inverse voltage pulse, adding all the inverse voltages in a given time window can therefore give us a quantity that is proportional to the input photon flux up to a conversion factor, see the Supplementary Material for further data acquisition details). For classical TPA measurements only the coherent pump beam is focussed into the microscope objective, with the same focus spot size at the sample. Utilized powers for the twin beams were ranging from 30 μ W to the maximum of 8 mW, and thus comparable with the average optical power of the twin beams. In addition, all measurements conducted with squeezed light are compared with measurements conducted with a continuous-wave (CW) laser of the same intensity, which in this work the classical coherent light source.

Measured classical TPA fluorescence rates for fluorescein, as a function of the input power, are shown by the red diamonds in Fig. 5.3, with error bars denoting one standard deviation. The observed quadratic power law relationship agrees well with the established literature for classical TPA, where the fluorescence signal is proportional to the square of excitation light intensity [175]. Fluorescence rates induced by SL-TPA of 8 mW optical power (3.5 mW + 1.0 mW probe and seed; 3.5 mW conjugate) and 4 mW optical power (1.75 mW + 0.5 mW probe and seed; 1.75 mW con-

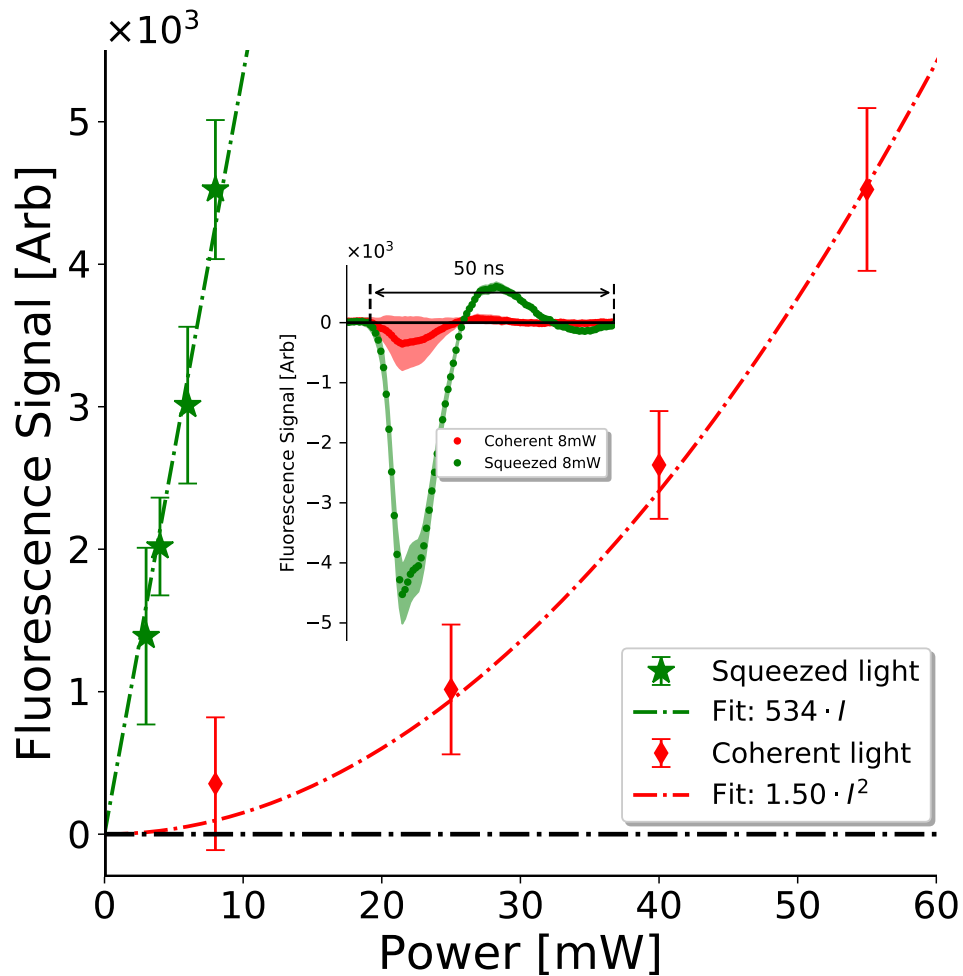


Figure 5.3: Fluorescence rates versus excitation power. The red diamonds and the red (dash-dotted) line show the measured values for the coherent excitation and the respective quadratic fit. The green stars are the rates for SL-TPA induced by the twin-beam excitations, and the green (dash-dotted) line is the respective linear fit. Error bars denoting one standard deviation, and enhancement of a factor of ~ 50 with squeezed light at 8 mW. The fluorescence signal from 4 mW of squeezed light excitation is also shown. Inset: raw voltage output from the PMT for coherent light (red) and squeezed light (green) excitations of 8 mW optical power. The shaded area for each curve represents one standard deviation.

jugate) together with 6 mW optical power (2.6 mW + 0.8 mW probe and seed; 2.6 mW conjugate) and 3 mW optical power (1.3 mW + 0.4 mW probe and seed; 1.3 mW conjugate) are depicted by the green stars (although the 3 mW and 6 mW data points were taken on a different day, the trend is similar). Due to experimental constraints, 8 mW is the maximal power we are able to acquire for the squeezed light. The measured coherent rates are fitted by the quadratic function $R(I) = I^2 \times 1.5 \text{ mW}^{-2}$ (dash-dotted red line), which represents the benchmark of the true fluorescence rate as a function of the input power. It can be observed from the figure that the signal for 8 mW of coherent excitation deviates strongest from the fit. This fact can be attributed to background noise (e.g., electronic dark counts and spurious counts from stray ambient light) and the overall low signal to noise ratio (SNR) of the measurement (characterized by a standard deviation encompassing negative values). Following the fitted curve, the fluorescence rate for 8 mW coherent excitation is thus merely 9.6×10^1 [a.u.]. For SL-TPA of 8 mW excitation power the fluorescence rate is $\sim 4.46 \times 10^3$ [a.u.]. This value corresponds to a striking ~ 46.5 -fold enhancement over the coherent excitation. Vice versa, increasing the coherent excitation power seven-fold to ~ 55 mW, and thus the classical TPA rate by ~ 47.3 -fold, the measured rates for 8 mW SL-TPA and 55 mW classical TPA match, thus confirming the previous statement. Subtracting the contribution from the 1 mW coherent seed beam power it can be argued that the measured SL-TPA enhancement is around ~ 60 -fold over 7 mW coherent excitation. Note that the seed is uncorrelated to the quantum correlated photon pairs and that the 1 mW of coherent seed excitation itself will induce negligible classical TPA rates. However, when fluorescein is excited with 8 mW of squeezed light, the fluorescence signal (represented by the green star) is enhanced by a factor of ~ 50 as compared to the true value of TPA fluorescence with 8 mW of coherent excitation. More importantly, the measured fluorescence rate for 4 mW SL-TPA is $\sim 2.02 \times 10^3$ [a.u.]. Subtracting the respective optical power of the seed beam, we end up with the input flux ratio $7/3.5 = 2.00$ which matches the measured ratio $4.46/2.02 = 2.21$ well (within the calculated uncertainties). This is also true for the SL-TPA of 6 mW and 3 mW, which is indicative of the linear dependence on the input photon-pair flux that is expected for fluorescein in this regime. Quadratic terms thus do not seem to contribute here.

More importantly, matching the fluorescence signal from 8 mW of squeezed light with the CW laser requires at least a power of 55 mW, thus approximately 7 times more intensity.

TPA is highly sensitive to the near-instantaneous arrival of two photons at the sample, in particular with respect to the virtual state lifetime of the intermediate states used for the electronic transition from the ground to the final state [153, 172]. In ETPA this is quantified by the entanglement time T_e [153, 164, 176]. Adjusting T_e should change the measured SL-TPA enhancement. Hence, an investigation of the effect of relative temporal delay between the entangled photon pairs is conducted. The ETPA cross section σ_e is inversely proportional to T_e and thus the mean group velocity delay between the entangled photon pairs. In the FWM process of the atomic ^{85}Rb vapor, the group delay between the entangled pairs can be adjusted by changing the two-photon detuning δ of the double- Λ configuration in Fig. 5.2(b) [86]. The red, green and blue bars in Fig. 5.4 show the fluorescence rates induced by 8 mW SL-TPA for the values $\delta = -10$ MHz, -5 MHz and 0 MHz, respectively. For each δ value the same relative intensity-difference squeezing of 6.5 dB (see Fig. 5.2(c)) is maintained, such that the results are not affected by different entanglement levels. For $\delta = -5$ MHz a relatively small delay is achieved [86]. Degraded fluorescence rates for $\delta = -10$ MHz and $\delta = 0$ MHz confirm that the SL-TPA enhancement is degraded when the relative delay between the photon pairs is tuned away from its optimal value. Further experimental details on how to change the two-photon detuning δ can be found in the Supplementary Material.

5.2.1 DCM in DMSO

In general, the ETPA rate R_e as a function of the input photon-pair flux density ϕ is expected to follow the functional behavior $R_e(\phi) = \sigma_e\phi + \delta_r\phi^2$, where σ_e and δ_r are the cross sections for ETPA and classical TPA respectively and are determined by the electronic level structure of the system undergoing TPA [171, 172, 177]. Both values can be determined experimentally, or calculated theoretically via second-order perturbation theory for a sufficiently simple system [172]. As previously established, the coincident arrival and absorption of an entangled photon pair leads to the linear dependence $R_e(\phi) = \sigma_e\phi$ provided ϕ is sufficiently small [153, 164, 168]. For sufficiently high photon-pair fluxes, TPA can be induced by uncorrelated photons from different pairs as well.

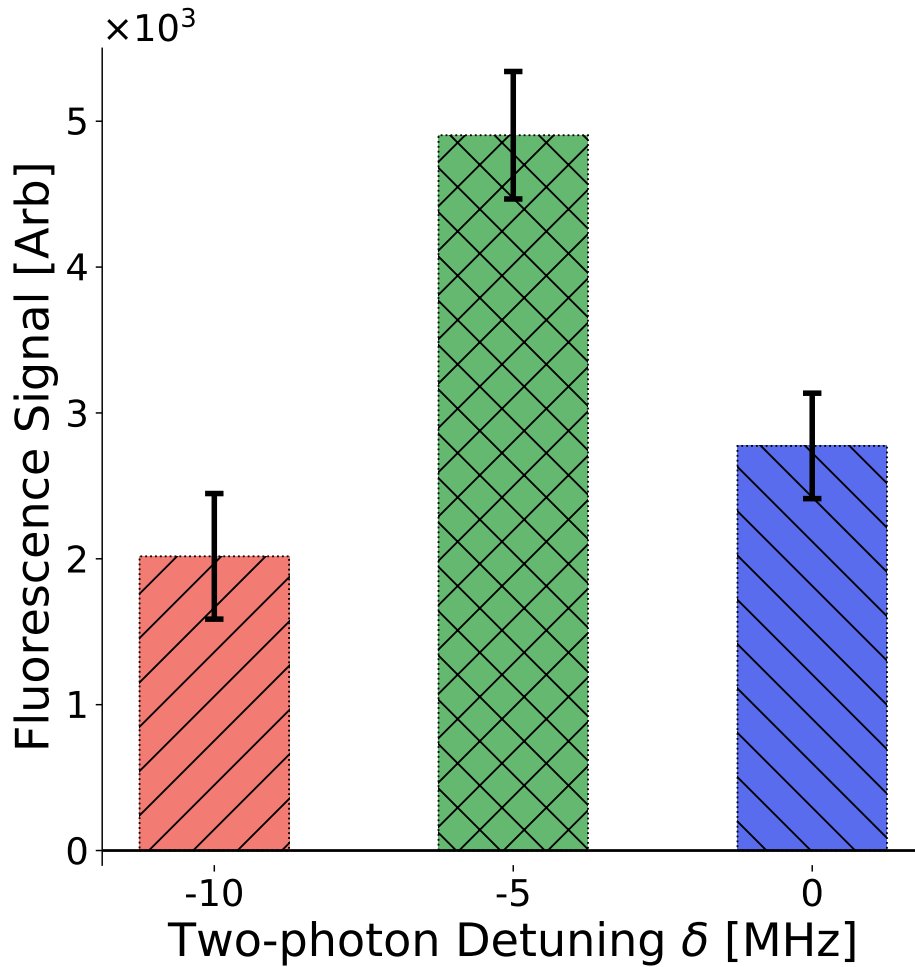


Figure 5.4: Fluorescence rates for 8 mW SL-TPA with three different two-photon detunings δ , shown in the atomic level structure in Fig. 5.2(b) as δ . Red, green and blue bars are for $\delta = -10$ MHz, -5 MHz and 0 MHz, respectively. This figure demonstrates degraded SL-TPA enhancements as a function of the relative arrival times of the entangled photon pairs.

The respective rate is equivalent to the classical TPA rate $\delta_r\phi^2$. Parity between both contributions is reached at the critical flux $\phi_c = \sigma_e/\delta_r$. So far as we know, ETPA experiments with biomarkers and low photon-pair fluxes observed only the linear dependence [153, 164, 168].

With means of investigating SL-TPA with high and freely adjustable optical powers, we investigated its functional behavior in DCM laser dye (see the Supplementary Material for its preparation). In addition, with means of validating the observation of TPA in our optical apparatus, a characterization of the nonlinearity is conducted by obtaining results with different coherent light excitation powers for DCM dyes (see Supplementary Material for its preparation). DCM dyes are known for strong TPA around 800 nm excitation wavelength, and along with a milli molar suspension, optical powers in the μW regime are sufficient to induce enough TPA fluorescence [178, 179]. The measured coherent TPA rates shown as red squares in Fig. 5.5, agree well with a quadratic behavior, represented by the fit function $R(I) = I^2 \times 0.304 \mu\text{W}^{-2}$. Logically, like in the case of fluorescein, this investigation should yield a quadratic coherent excitation power to fluorescence signal relationship as well. Indeed, as can be observed from Fig. 5.5 with red squares, the fit is undeniably quadratic. For SL-TPA in DCM, on the other hand, we observed a non-linear behavior of the functional form $R(I) = I \times 7.9 \mu\text{W}^{-1} + I^2 \times 0.59 \mu\text{W}^{-2}$. More importantly though, when the DCM dyes are excited with different powers of squeezed light, the excitation power to fluorescence signal relationship has a nonlinear behavior. Indeed, ETPA can be accompanied by nonentangled photons or random classical two-photon absorption effects [180]. Therefore, the overall two-photon absorption rate, R_e , can be expressed [171–173, 177] as the summation of the linear ETPA rate and the quadratic classical TPA rate, $R_e = \sigma_e\phi + \delta_r\phi^2$, where σ_e is the entangled two-photon absorption cross section, δ_r is the classical two-photon absorption cross section, and ϕ is the input photon flux density of photon pairs. When the input photon flux is low, the linear term dominates [153, 164, 168], while both contributions are significant when the input flux is high. The polynomial behavior of SL-TPA in Fig. 5.5 implies that the photon-pair flux is already high enough to observe both linear and quadratic contributions. In fact, given the fit values, parity is already reached at $I_c = 7.9 \mu\text{W}^{-1}/0.304 \mu\text{W}^{-2} = 26.0 \mu\text{W}$ for the DCM solution.

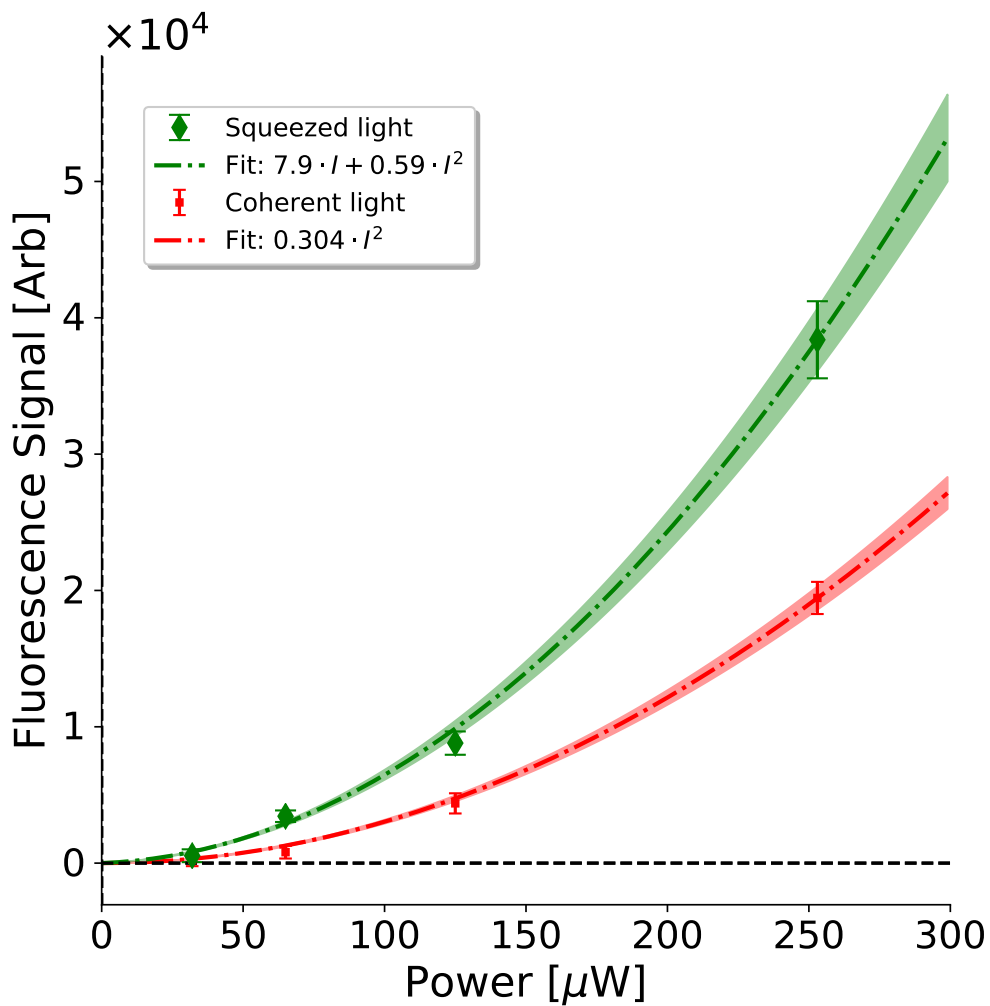


Figure 5.5: Fluorescence signal of DCM versus excitation power of coherent light (red) and squeezed light (green). Coherent light fitting curve obeys a quadratic behavior, while squeezed light fitting curve shows a polynomial behavior, indicating a high input of entangled photon-pair flux.

It is worthy to point out that the DCM laser dye solution requires much lower excitation powers than the fluorescein solution to produce appreciable TPA fluorescence rates, most probably due to a larger classical TPA cross section δ_r . In Fig. 5.5, the DCM signal at 130 μW coherent excitation ($\sim 0.45 \times 10^4$ a.u.) roughly equals the fluorescein signal at 55 mW coherent excitation ($\sim 4.43 \times 10^3$ a.u.). Taking into account the concentration of the two solutions (see the Supplementary Material for details of samples preparation) we estimate the classical TPA cross section δ_r of DCM is roughly 1800 times larger than that of fluorescein. However, the ETPA cross section σ_e of DCM is actually smaller than that of fluorescein, as demonstrated by the relatively small SL-TPA enhancements. Extrapolation of the fit curves in Fig. 5.3 would yield $I_c = 562 \text{ mW}^{-1}/1.5 \text{ mW}^{-2} = 3.75 \times 10^5 \mu\text{W}$, which is $\sim 1.4 \times 10^4$ higher than for DCM. The difference can be attributed to different electronic level structures of these two organic molecules [164].

As can be seen from Figs. 5.3(a) and 5.5, the fluorescence signal induced by 130 μW of coherent light from DCM is greater than that induced by 8 mW of coherent light from fluorescein. However, the entangled two-photon absorption cross section σ_e of DCM is actually smaller than that of fluorescein, as demonstrated by the fluorescence enhancements. This inconsistency can be attributed to different electronic level structures of these two organic molecules [164].

5.3 Raw data and post-processing

In our experiment, a Thorlabs' PMM02 photomultiplier tube (PMT) that has a fast response times and high sensitivity, was used to measure the fluorescence signal. it can convert the nA- or μA -scale current output by the anode to a voltage in the mV or V range, respectively. The fluorescence signal is such weak signal, and is below the noise of scientific Complementary metal–oxide–semiconductor (sCMOS).

PMTs provides a sensitive and high-gain current output that is proportional to the incident light, see Fig.5.6. The PMT has a photocathode, 8 - 14 secondary emitting electrodes called dynodes, and a collection electrode called an anode. Photon is incidents on the photocathode, and an electron is released with photoelectric effect. This first step released electron will be accelerated under a

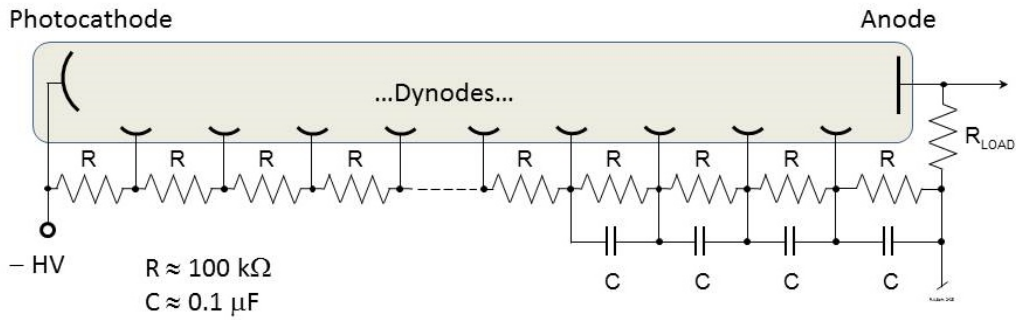


Figure 5.6: Typical photomultiplier voltage divider circuit using negative high voltage, image from wikipedia website.

high voltage influence, and toward the dynode and crash into it, releasing second step electrons. This processing provides electron gain of 3-5. Typically, the potential is 100-200 V higher than the previous one. After several amplifications, the electrons are collected by the anode and a current pulse is output. The output will a voltage signal, which is generated by connecting to a low load resistance across the anode and ground.

The PMT raw data cannot be used to indicate fluorescence intensity, directly. The level and number of down-side peaks reflect the fluorescence intensity. So, we have to pick out those peaks via data analysis method. The post-processed PMT voltage raw data of fluorescence signal is shown in Fig.5.8. The fluorescence signal(red curve) is well separated from the background signal(black curve).

As we discussed, a sCOMS cannot used to measure such weak fluorescence signal. The fluorescence signal measurement is based on the sensitive and high-gain of PMT with post-processing. Thus, the whole detection scheme must be put into a light proof box. Otherwise, any environment light will ruin the detection part.

5.4 Conclusions

In conclusion, this work investigates two-photon absorption fluorescence rates in fluorescein biomarkers and in DCM laser dye, induced by a coherent CW excitation light and by the bright two-

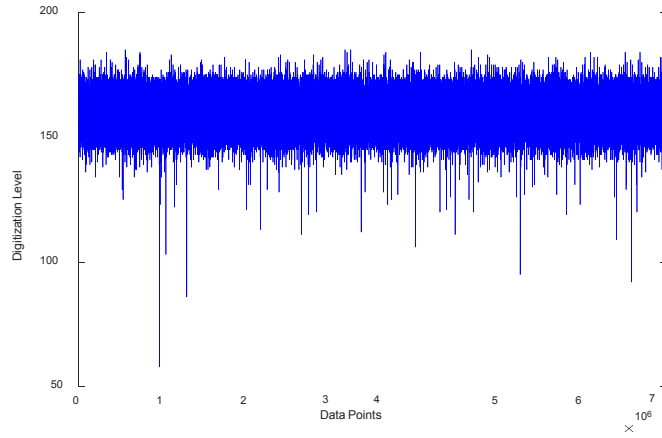


Figure 5.7: The PMT voltage raw data of fluorescence signal from DCM. The time-step of two continue data point is 0.25 ns, and 7×10^6 points are collected by a oscilloscope.

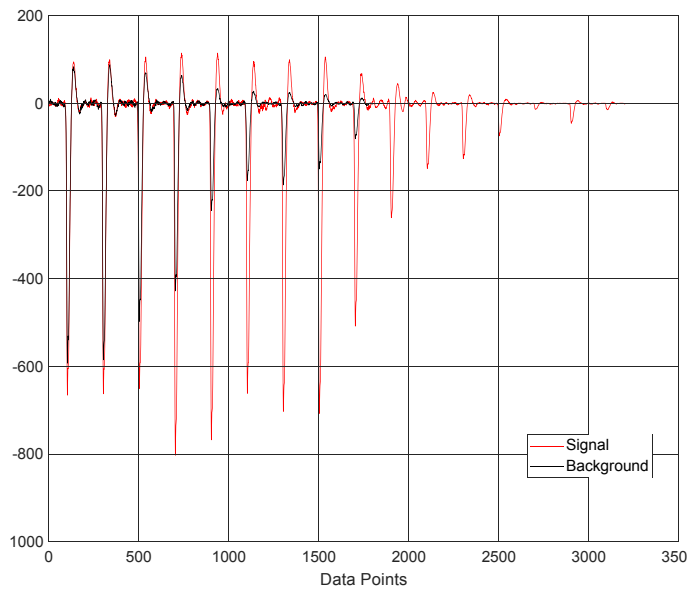


Figure 5.8: The post-processed PMT voltage raw data of fluorescence signal from DCM.

mode squeezed light. For the coherent CW excitation both fluorophores show the well-expected quadratic dependence on the input photon flux. The experimental results for fluorescein with SL-TPA, however, demonstrate a linear dependence on the input optical power, along with a ~ 47 -fold TPA fluorescence enhancement for 8 mW squeezed light compared to 8 mW coherent light. This can be attributed to the predominant occurrence of entangled two-photon absorption of quantum-correlated photon pairs. From extrapolation it can be concluded that parity between classical and entangled TPA contributions would only be reached at 375 mW optical power [also transform into flux via photon energy and the focus area]. In addition, and differently from previous works using quantum states of light for TPA in fluorophores, we report that SL-TPA in DCM laser dye is governed by a polynomial behavior, which can be entirely attributed to its far greater entangled photon-pair flux, as compared to using SPDC sources. Thus, this work demonstrates that our FWM based bright two-mode squeezed light source can achieve ultra-low intensity TPA for biosensing and bioimaging, and thus bear the potential to open up entirely new avenues for *in vivo* deep tissue studies of biological specimens via TPA.

6. BEYOND SUB-RAYLEIGH IMAGING VIA HIGH ORDER CORRELATION OF SPECKLE ILLUMINATION *

Second order intensity correlations of speckle illumination are extensively used in imaging applications that require going beyond the Rayleigh limit. The theoretical analysis shows that significantly improved imaging can be extracted from the study of increasingly higher order intensity cumulants. We provide experimental evidence by demonstrating resolution beyond what is achievable by second order correlations. We present results up to 25th order. We also show an increased visibility of cumulant correlations compared to moment correlations. Our findings clearly suggest the benefits of using higher order intensity cumulants in other disciplines like astronomy and biology.

6.1 Introduction

Speckles in optics are well known and have various applications. Typically, speckles are produced in the scattering of a coherent beam of light by a random medium [182–188]. The propagation difference of partially coherent beams and coherent lasers through a random medium has been successfully explained by Dogariu et. al [189–191]. The medium scatters a coherent beam in various directions with randomly varying phases. The scattering medium under fairly general conditions produces fields that can be modeled as Gaussian fields. The characteristics of the medium can be extracted from the spatial and temporal coherence of the medium. The spatial coherence information is in turn obtained from the intensity-intensity correlations [192–194]. Such studies provide a wealth of information on the medium [195]. Speckled illumination is produced using a rotating ground glass [196] and has been shown to beat the diffraction limit [197–201]. Second order intensity correlations beat the diffraction limit by a factor of $\sqrt{2}$. Most studies on beating the diffraction limit use second order intensity correlations. Also the super-resolution optical

*Part of this chapter is reprinted from Ref. [181] (Fu Li, Charles Altuzarra, Tian Li, M. O. Scully and G. S. Agarwal, “Beyond sub-Rayleigh imaging via high order correlation of speckle illumination”, *Journal of Optics* 21, 115604 (2019)) with permission from IOP Publishing.

fluctuation imaging (SOFI) technique based on cumulant correlations, is limited to samples with particular intrinsic blinking characteristics [202]. Differently, in this work, super-resolution does not rely on the object's blinking characteristics, but instead intensity fluctuations from the speckled light source are used with high order correlations, which results in super-resolution imaging beyond the Rayleigh limit. Several other theoretical works have investigated the uses of higher order correlations [203–205].

In this letter we experimentally demonstrate higher order correlations for imaging applications by using speckle illumination, and analyze the reliability of high order correlations, which consolidates the potential for applications. We first present a theoretical analysis based on the cumulants of the measured intensity distributions and show that such cumulants can beat the diffraction limit by a factor of \sqrt{n} . We then present experimental confirmation. Our results with speckle light underline two advancements: 1) the improvement in resolution generated by moment correlation orders $N > 2$, and 2) the superior resolution offered by cumulants as compared to moments. In addition, our experiment determines that speckle illumination is also valid for non-fluorescent samples, which is very important for label free bio-imaging.

6.2 Theoretical Basis

As illustrated in figure.1, the experimental setup uses a continuous wave laser of 785nm in wavelength (Omicron LuxX-785) incident on a rotating ground glass to generate a speckle pattern. This source is used to illuminate a micro-fabricated mask object (Toppan Digidat), notably four holes milled in a chromium layer deposited on glass, for which their diameter l_0 equals their separation of $l = 25\mu m$. An aperture limited by an adjustable iris and an $f = 150mm$ imaging lens (L), produce an image with a magnification factor $M = d'/d = 1$ with $d' = d = 300mm$, where d' and d are the mask object distance and image distance from the lens, respectively. Here the image is mapped on a 1280x1024 pixels' CMOS camera (Thorlabs DCC3240N), whose pixel area is 5.3 μm x 5.3 μm .

In our setup, the electric field generated from the ground glass propagates to a transmission

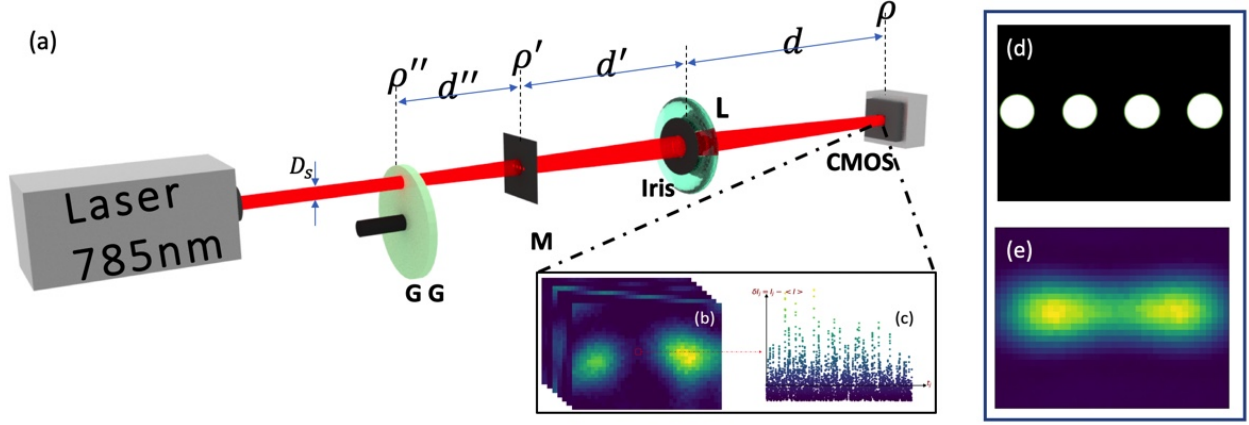


Figure 6.1: Color online. The experimental setup. (a) The laser incident on a rotating ground glass (GG) generates speckled light. The light transmitting through the mask (M) and iris is collected by the camera (CMOS) with a lens (L) $f=150\text{mm}$. Here, distance $d' = d = 300\text{mm}$. (b) Several image frames are recorded to compute the high order correlation images. (c) A pixel's temporal intensity fluctuation. (d) The mask object, notably four dots. (e) Laser illumination intensity (Int.) imaging without Ground Glass (GG), for which the image of the four dots is blurred since the Rayleigh limit is twice the distance of the dot separation.

mask with the transmission coefficient $t(\vec{\rho}'_i)$, where $\vec{\rho}'_i$ is a position on the mask object plane. For the transmitted electric field, the intensity fluctuation correlation, which is crucial to surpass the Rayleigh limit, is described by [201, 206]

$$\begin{aligned} \langle \delta I(\vec{\rho}'_1) \delta I(\vec{\rho}'_2) \rangle &= |G^{(1)}(\vec{\rho}'_1, \vec{\rho}'_2)|^2 \\ &\propto |t(\vec{\rho}'_1)|^2 |t(\vec{\rho}'_2)|^2 e^{-\frac{(\vec{\rho}'_1 - \vec{\rho}'_2)^2}{l_c^2}}, \end{aligned} \quad (6.1)$$

with intensity fluctuation $\delta I(\vec{\rho}'_i) = I(\vec{\rho}'_i) - \langle I(\vec{\rho}'_i) \rangle$ and a coherence length $l_c \propto \lambda d'' / D_s$. Here, $G^{(1)}(\vec{\rho}'_1, \vec{\rho}'_2) = \langle E^*(\vec{\rho}'_1) E(\vec{\rho}'_2) \rangle$ is the first order correlation [182]. The electric field generated from the ground glass propagates to the mask, the transmission part of electric field at the $\vec{\rho}'$ plane is given by $E(\vec{\rho}') = t(\vec{\rho}') \int G(\vec{\rho}' - \vec{\rho}'', d'') E(\vec{\rho}'') d\vec{\rho}''$, where

$$G(\vec{\rho}' - \vec{\rho}'', d'') = \frac{e^{ikd''}}{i\lambda d''} e^{\frac{i\pi}{\lambda d''}(\vec{\rho}' - \vec{\rho}'')^2}$$

is the Fresnel propagator. With the assumption of $\langle E(\vec{\rho}'_1) E(\vec{\rho}'_2) \rangle \sim \delta(\vec{\rho}'_1 - \vec{\rho}'_2)$ at the

ground glass plane, $G^{(1)}(\vec{\rho}'_1, \vec{\rho}'_2) \propto t^*(\vec{\rho}'_1) t(\vec{\rho}'_2) e^{-\frac{(\vec{\rho}'_1 - \vec{\rho}'_2)^2}{l^2}}$ is obtained, see Appendix 6.6.

Thus, when the mask's hole separation is approximately equal to or larger than the coherent length (l_c), the holes contribute independently and randomly, $\langle \delta I(\vec{\rho}'_i) \delta I(\vec{\rho}'_j) \rangle_{i \neq j} \simeq 0$, see Eqn.(6.1). The holes are imaged onto the camera, whose intensity $I(\vec{\rho})$ at $\vec{\rho}$ position is formulated by

$$I(\vec{\rho}) = \sum_{i=1,2,3,4} h_i I_i, \quad (6.2)$$

where $h_i = h(\vec{\rho} - \vec{\rho}_i)$ is the point-spread function (PSF) of the imaging system and $I_i = I(\vec{\rho}'_i)$, and the summation is over all points in the holes. The width of the PSF gives the Rayleigh limit of an imaging system, which blurs out any point-like object to an Airy disk. Instead of using intensity imaging, we use cumulants to demonstrate super-resolution.

The quantity $I(\vec{\rho})$ is a statistically fluctuating quantity. We evaluate cumulant generating function $K(\beta)$ of $I(\vec{\rho})$

$$\begin{aligned} K(\beta) &= \ln \langle \exp(\beta I(\vec{\rho})) \rangle \\ &= \sum_i \ln \langle \exp(\beta h_i I_i) \rangle, \end{aligned} \quad (6.3)$$

where I_i is the statistical independence of the variables. We can rewrite Eqn.(6.3) in terms of the cumulants κ_n of $I(\vec{\rho})$ and κ_{in} of $I(\vec{\rho}'_i)$,

$$\kappa_n(\vec{\rho}) = \sum_i (h(\vec{\rho} - \vec{\rho}'_i))^n \kappa_{in}. \quad (6.4)$$

Note that there are no cross terms in Eqn.(6.4). In contrast, the n^{th} order moment is given by

$$m_n = \langle (I)^n \rangle = \left\langle \left(\sum_i h_i I_i \right)^n \right\rangle. \quad (6.5)$$

m_n is composed of contributions from terms which are products of the PSF like $h_i h_j$ with ($i \neq j$). For example, the 4^{th} order moment is

$$m_4 = \sum_i h_i^4 \langle (I_i)^4 \rangle + \sum_{i \neq j} h_i^2 h_j^2 \langle (I_i)^2 (I_j)^2 \rangle. \quad (6.6)$$

‘Noisy’ terms like the last term in Eqn.(6.6) do not appear in κ_4 , therefore, imaging based on higher order cumulants κ_n are much more effective than images based on m_n .

In comparison with the intensity imaging given by $I(\vec{\rho}) = \sum_{i=1,2,3,4} h_i I_i$, Eq.(6.4) suggests that the n^{th} order cumulant can yield imaging resolution improvement by a factor $\sim \sqrt{n}$, due to its narrowed effective PSF $h_{eff} = h^n$. By extension, with respect to a $G^{(2)}$ image [198, 199], an improvement by a factor of $\sim \sqrt{n/2}$ can be achieved. To simplify the calculation, the cumulant formulas are expressed by the central moment form, see 6.7.

$$\kappa_n = \mu_n - \sum_{i=1}^{n-1} \binom{n-1}{i} \kappa_{n-i} \mu_i, \quad (6.7)$$

where $\mu_n = \langle (I - \langle I \rangle)^n \rangle$ is the central moment.

We next present experimental results based on κ_n and m_n .

6.3 Experimental Results

In our work, as opposed to previous works in speckle imaging [198, 199], we render the image completely indistinguishable by minimizing the aperture of the pinhole. The reason for excessively blurring the image is to demonstrate the power of this method that uses correlation orders of a factor 10 higher than what has been demonstrated so far experimentally with speckle light. Indeed though, our technique has an important requirement, each hole must be independently fluctuating in intensity. In our experiment, this condition is satisfied by engineering the speckles of the light source in relation to the object’s structures. Thus, the coherence length of the source (i.e., the distance between speckles) needs to match the distance between the micro-structured holes on the object.

In this section, our discussion starts with the generation of the speckle light source, which is a key point for understanding this experiment. Independent intensity fluctuations manifest them-

selves and are characterized by $g^{(2)}(\vec{\rho}'_1, \vec{\rho}'_2) \propto \langle \delta I(\vec{\rho}'_1) \delta I(\vec{\rho}'_2) \rangle$, where δI is the intensity fluctuation at the target object plan. Thus, the measurement of the camera without the target object was produced, as shown in figure.6.2 (a). These images were then used to calculate the coherence length, plotted in figure.6.2 (b). In fact, based on the relation $l_c \propto \lambda d''/D_s$, speckle pattern of different coherence lengths can be obtained, namely by changing the beam size D_s .

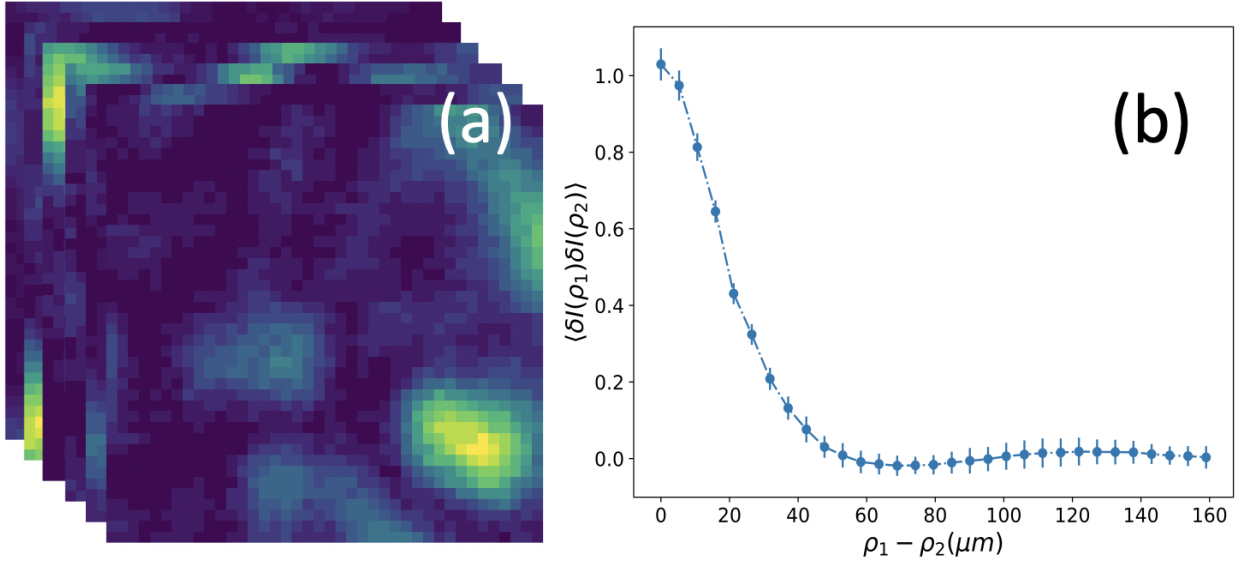


Figure 6.2: Color online. The speckle pattern coherence length $l_c \propto 24\mu\text{m}$. The target object is removed, and multi-frames images are measured, see (a). The correlations of the intensity fluctuation $\langle \delta I(\rho'_1) \delta I(\rho'_2) \rangle$ are calculated, see (b)

In our experiment, the coherence length is $24\mu\text{m}$, which approximately equals to the separation $25\mu\text{m}$. By obtaining the intensity fluctuation at each pixel and post-processing them, as illustrated in figure.6.1 (b),(c), moment-generated images were produced in demonstrating that this technique provides resolution beyond the Rayleigh limit. This is shown, first and foremost, by completely blurring the image, which is done here by adjusting the aperture of the iris to a diameter of 5.75mm . This size provides a Rayleigh limit of $\delta x = 0.61\lambda M/NA = 50\mu\text{m}$, which is two times the mask's hole separation of $l = 25\mu\text{m}$. Thusly, it comes as no surprise that the laser illumination intensity image without Ground Glass (GG), portrayed in figure.6.1 (e), yields only two peaks, and the

average intensity of the speckle illumination image yields a completely blurred image as shown in figure.6.3 (a). Based on our theory, a factor of $\sqrt{2}$ improvement of second order central moment is less than the ratio of 50/25, so the second order central moment also cannot resolve the mask object, see figure. 6.3 (b). In contrast, the 12th order central moment μ_{12} , the 20th order central moment μ_{20} and the 25th order central moment μ_{25} in figure. 6.3 (d), (e) and (f) respectively, result in a well-defined mask object. In fact, the Rayleigh limit is so large that only higher orders provide a definable image. Indeed, the difference in contrast is ascertained in figure.6.3 (g). In this figure, the normalized photon counts are plotted in the horizontal direction, for two rows of pixels. As expected, a higher order moment provides a higher visibility image, and the four dots' feature is recovered where intensity imaging yields a completely blurred image with no contrast.

An imaging technique is unreliable if the results are not reproducible with high confidence. Indeed, the practicality of an imaging technique is qualified by the performance and reliability, which in mathematical language translates to high visibility $(I_{max} - I_{min})/(I_{max} + I_{min})$ and low standard deviation, respectively. Without loss of generality, we fix I_{max} to be the second peak and the I_{min} to be the second valley. For our setup, due to the randomness of the speckle illumination, it is clear that a large number of frames are required to compute a well-defined mask image.

From figure.6.3 (h), we observe that visibility and standard deviation behave differently as a function of frame number. In fact, as the number of frames increases, average values for visibilities increase and standard deviations decrease. The data was recorded for 5000, 10 000, 20 000, and 50 000 frames for moments from the 2nd to the 25th orders. We conducted the experiment 10 times with 5000 frames, i.e. N=5000. Then, the visibilities were calculated by retrieving the average intensity for the same two central rows. We observed that the lowest degree of practicality is generated from 5000 frames, for which its 20th orders visibility and standard deviation read 0.69 ± 0.17 . Indeed, this low frame number yields the lowest visibility values and, as compared to the other frame numbers, much larger error bars. Thus, using 5000 frames fails to qualify as a practical imaging technique. In contrast, using 50 000 frames yields highly improved characteristics both for visibility and standard deviation. As compared to the values obtained with 5000 frames at the

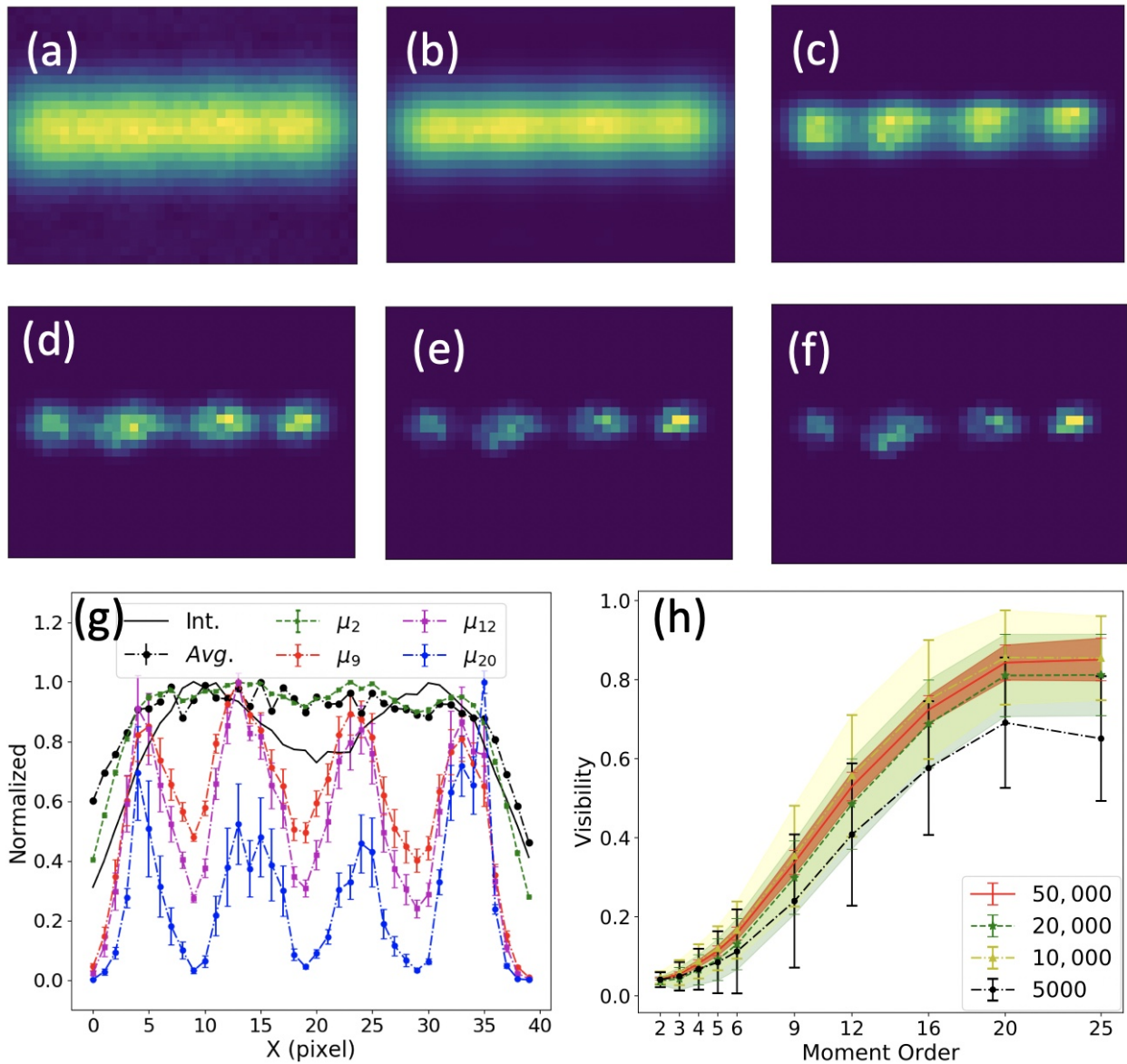


Figure 6.3: Color online. Comparison of traditional intensity imaging and high order moment imaging. (a) The average intensity (Avg.) imaging of speckle illumination, and the images reconstructed by the 2nd, 9th, 12th, 20th and 25th order central moment (b, c, d, e, f). (g) The contrast comparison from images of different orders by summing two rows of pixels that are centered with the holes. (h) The visibility and standard deviation as a function of the moment orders computed by using the different frame numbers.

20th order, 50 000 frames produce a visibility improvement of 22% with a 4-fold decrease in the standard deviation, which reads (0.84 ± 0.04) .

Moreover, 10 000 and 20 000 frames have acceptable values that certainly converge to the 50 000 frame values, thus we anticipate that increasing the frame number will probably not improve the visibility and only slightly improve the standard deviation. Due to noise, such as the dark counts of the CCD, there are limitations in correlation order for the post-processing of the image. For instance, by using 5000 frames the highest visibility is at the 20th order. Eventhough higher orders should give better resolution, the 25th order is insufficient due to noise. To achieve a resolution that goes beyond the sub-Rayleigh limit, a large number of frames are required, which is not a problem for a static object but is a limitation for a rapidly varying object. For a real time or in vivo experiment, very fast cameras can be used, like for instance a SPAD camera that can do more than 250 000 frames per second [207]. In addition, in our current work the data processing for high order correlations is highly paralleled, which means that computation time can be dramatically suppressed with a powerful GPU card.

As previously mentioned, central moments beyond the 3rd order suffer cross-terms that worsen the resolution. Those cross-terms can effectively be eliminated by using nonlinear combinations of lower order moments. In this manner, cumulants display a significant improvement in surpassing the Rayleigh limit as compared to central moments. This can be observed in the image in figure.6.4 (b), (c), whereby the moment and cumulant post-processing of the 6th order is compared. The difference in contrast is highlighted in figure.6.4 (d), as can be observed by taking two rows of pixels that are centered with the holes. Indeed though, the 6th order central moment μ_6 shows much improvements but not as compared to the 6th cumulant κ_6 , which reads more than a two-fold improvement with respect to the moment of same order. The cumulant is computed based the nonlinear combination of moments, so the error bars increase minimally.

In addition, central moments and cumulants are compared by plotting their respective visibilities for 50,000 frames as a function of orders. μ_n and κ_n are plotted from the 2nd to 6th orders with their error bars. As illustrated in figure.6.4 (e), the average of the second and third orders are the

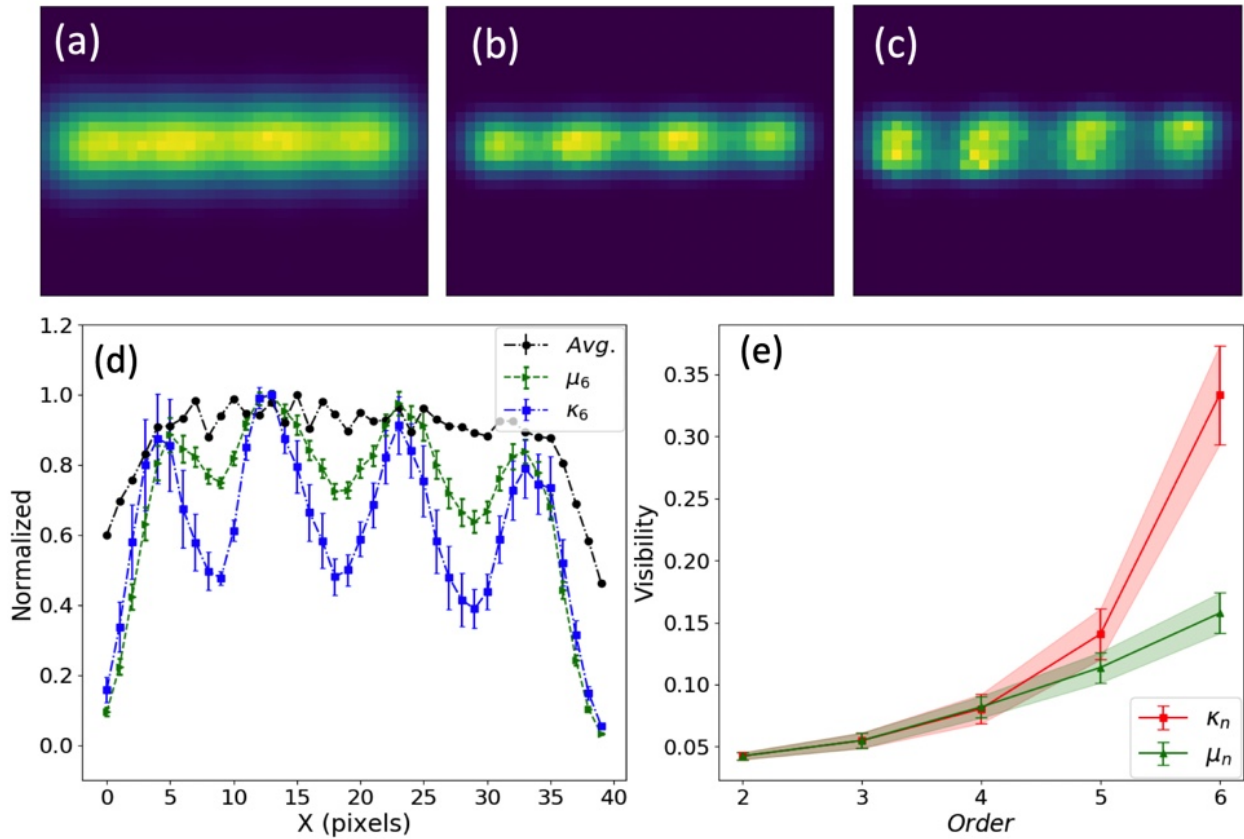


Figure 6.4: Color online. Comparison of cumulant and moment imaging. (a) The 2^{nd} order central moment μ_2 image. Since the ratio of the Rayleigh limit to dots separation is $50/25 = 2$, which is larger than the resolution improvement $\sqrt{2}$ that μ_2 yields, the image is blurred. (b, c) for 6^{th} order moment and cumulant image, respectively. (d) The contrast comparison of different order images by taking two rows of pixels that are centered with the holes, and (e) the visibility and standard deviation of moment versus cumulant with 50 000 frames.

same for central moments and cumulants, which can be explained mathematically since $\mu_n = \kappa_n$ for $n = 2, 3$. The 4th order central moment and cumulant result in very similar visibilities, since the cross-terms only contribute minimally to noise. In fact, a large difference in visibility is only observable at the 6th order cumulant, where κ_6 yields approximately the same visibility as the 9th order central moment with an average visibility of ~ 0.3 , as can be seen in figure.6.3 (d).

6.4 Bio-imaging via correlation

The correlation algorithm also be used in bio-imaging, which will be demonstrated in further discussion. As we know that the scattered light from a random medium will produce a speckle pattern, which is a random process and can only be described statistically. The bright spot results from the constructive interference of scattered light, while dark spots satisfy destructive condition, see Fig.6.5. When these random particles moves, the speckle pattern their produced changes with time, which we call time-varying speckle.

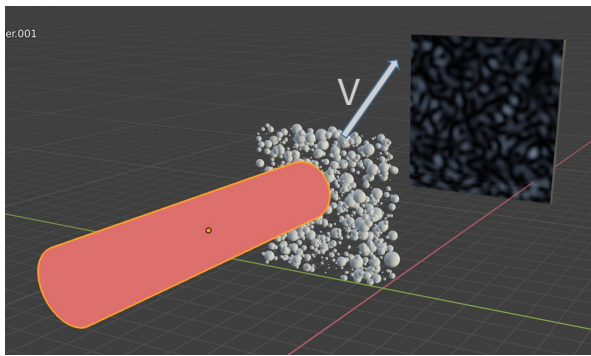
We could imaging, for a directional fluid moving, the time varying speckle also moves with medium moving direction. The speed of speckle pattern changing dependents on the velocity of medium moving, which means that the high order correlation of speckle pattern could provide the information on medium moving direction and speed, see Fig.6.5(b).

Next, we will demonstrate that the correlation can provide the water moving in a bio-sample. The sample is shown in Fig.6.6, where (a) is imaging in cell level and (b) is its flower and leaf image. Then, we build microscopy for bio-imaging, and its speckle pattern shows the water flow direction and intensity.

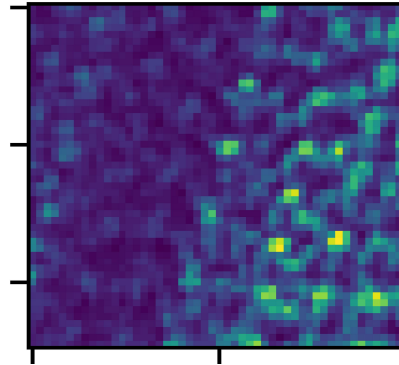
Comparing with conventional microscopy imaging, the second order correlation imaging of time varying speckle pattern, which clearly shows t the water moving region and moving intensity, see Fig.6.7(a). The Fig.6.7(b) is zoom in result of Fig.6.7(a).

6.5 Conclusion

By using speckle illumination with high order correlations, we demonstrate an imaging scheme that goes beyond the sub-Rayleigh limit. We show that the object's true features can be recovered

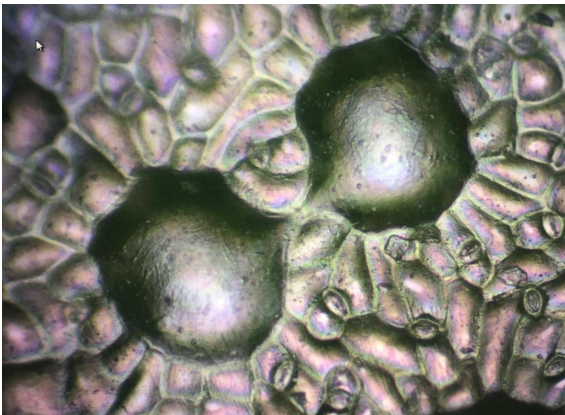


(a)



(b)

Figure 6.5: (a) A laser beam illuminates on a random medium which move at velocity V with direction labeled, and a time varying speckle pattern is generated as result of interference of scattered light. The result of 6th order cumulant imaging (b).



(a)



(b)

Figure 6.6: (a) The conventional microscopy leaf cell imaging with white illumination, and cell image is a stable imaging. The flower and leaf image (b).

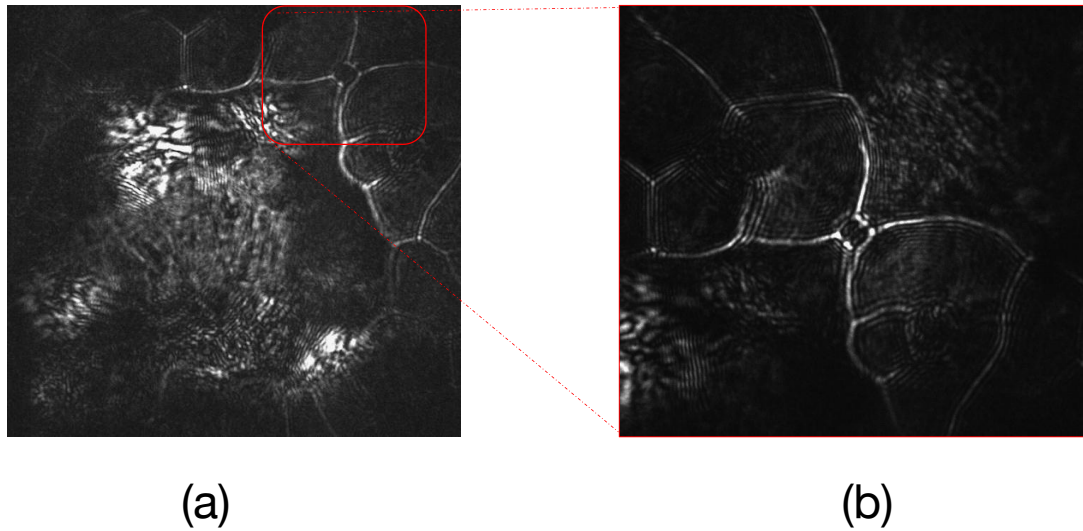


Figure 6.7: The second order correlation imaging of time varying speckle pattern, which clearly shows the water moving region and moving intensity (a), and its zoom imaging result (b).

where a traditional diffraction-limited imaging method yields a completely blurred image. This is done by correlating photon counts at each pixel with two post-processing functions: moments and cumulants. The order moment $n = 20$ gives the highest contrast/visibility of 0.84 ± 0.04 . In addition, and more importantly, we explore using cumulants, which, as demonstrated, show much more improvement as compared to moments starting at the 5^{th} order. An interesting extension of this method would be in the imaging of gray objects. Our results clearly show the capability of higher order intensity cumulants in super-resolution applications where speckles are used. This method widens the possibilities for high order correlation imaging specifically for uses in bio-imaging and astronomy. In biomedical optics, one of standard imaging methods is laser speckle contrast imaging (LSCI), which is based on the 2^{nd} order correlation [208–212]. With the support of the results presented in our work, this high order correlation method could provide a competitive edge with LSCI. Moreover, speckle imaging has achieved high resolution to identify twin stars with far less cost in time and means, which motivates speckle imaging applications in astronomy [213].

6.6 Correlation calculation

Based on the experiment setup figure1(a), after the scattering, the random electric field at the $\vec{\rho}''$, which is the ground glass plane, is described by: $\langle E(\vec{\rho}_1'') E(\vec{\rho}_2'') \rangle = w(\vec{\rho}_1'') \delta(\vec{\rho}_1'' - \vec{\rho}_2'')$, where $\langle \dots \rangle$ denotes time averaging. The electric field generated from the ground glass propagates to the mask and the transmission part of electric field at the $\vec{\rho}'$ plane is given by $E(\vec{\rho}') = t(\vec{\rho}') \int G(\vec{\rho}' - \vec{\rho}'', d'') E(\vec{\rho}'') d\vec{\rho}''$, where $G(\vec{\rho}' - \vec{\rho}'', d'') = \frac{e^{ikd''}}{i\lambda d''} e^{\frac{i\pi}{\lambda d''}(\vec{\rho}' - \vec{\rho}'')^2}$ [18, 21] is the Fresnel propagator, and $t(\vec{\rho}')$ is the transmission coefficient of the mask object.

So, the first order correlation function of the transmitted field immediately after mask is given by

$$\begin{aligned}
& G^{(1)}(\vec{\rho}'_1, \vec{\rho}'_2) \\
&= \langle E^*(\vec{\rho}'_1) E(\vec{\rho}'_2) \rangle \\
&= \left\langle \int \int t^*(\vec{\rho}'_1) G^*(\vec{\rho}'_1 - \vec{\rho}''_1, d'') t(\vec{\rho}'_2) G(\vec{\rho}'_2 - \vec{\rho}''_2, d'') \right. \\
&\quad \left. E^*(\vec{\rho}''_1) E(\vec{\rho}''_2) d\vec{\rho}''_1 d\vec{\rho}''_2 \right\rangle \\
&= t^*(\vec{\rho}'_1) t(\vec{\rho}'_2) \int G^*(\vec{\rho}'_1 - \vec{\rho}''_1, d'') G(\vec{\rho}'_2 - \vec{\rho}''_2, d'') w(\vec{\rho}''_1) d\vec{\rho}''_1 \\
&= \frac{t^*(\vec{\rho}'_1) t(\vec{\rho}'_2)}{(\lambda d'')^2} \int e^{\frac{-i\pi}{\lambda d''}(\vec{\rho}'_1 - \vec{\rho}''_1)^2} e^{\frac{i\pi}{\lambda d''}(\vec{\rho}'_2 - \vec{\rho}''_2)^2} w(\vec{\rho}''_1) d\vec{\rho}''_1 \tag{6.8} \\
&= \frac{t^*(\vec{\rho}'_1) t(\vec{\rho}'_2)}{(\lambda d'')^2} e^{\frac{-i\pi}{\lambda d''}(\vec{\rho}'_1 - \vec{\rho}'_2)^2} \int e^{\frac{2i\pi}{\lambda d''}(\vec{\rho}'_1 - \vec{\rho}'_2) \cdot \vec{\rho}''_1} w(\vec{\rho}''_1) d\vec{\rho}''_1 \\
&= \frac{t^*(\vec{\rho}'_1) t(\vec{\rho}'_2)}{(\lambda d'')^2} e^{\frac{-i\pi}{\lambda d''}(\vec{\rho}'_1 - \vec{\rho}'_2)^2} w \int_0^{D_s/2} e^{\frac{2i\pi}{\lambda d''}(\vec{\rho}'_1 - \vec{\rho}'_2) \cdot \vec{\rho}''_1} d\vec{\rho}''_1 \\
&= \frac{t^*(\vec{\rho}'_1) t(\vec{\rho}'_2)}{(\lambda d'')^2} 2\pi D_s w e^{\frac{-i\pi}{\lambda d''}(\vec{\rho}'_1 - \vec{\rho}'_2)^2} \text{somb} \left(\frac{2\pi D_s}{\lambda d''} \left| \vec{\rho}'_1 - \vec{\rho}'_2 \right| \right) \\
&\propto t^*(\vec{\rho}'_1) t(\vec{\rho}'_2) e^{-\left(\frac{\lambda d''}{\pi D_s}\right)^2 (\vec{\rho}'_1 - \vec{\rho}'_2)^2}
\end{aligned}$$

where $\text{somb}(x) = 2J_1(x)/x$, D_s is the diameter of laser beam. Here $e^{\frac{-i\pi}{\lambda d''}(\vec{\rho}'_1 - \vec{\rho}'_2)^2}$ is only a phase factor and can be neglected. Thus, the intensity fluctuation correlation can be simplified as

$$\begin{aligned}
& \langle \delta I(\vec{\rho}'_1) \delta I(\vec{\rho}'_2) \rangle \\
&= \langle (I(\vec{\rho}'_1) - \langle I(\vec{\rho}'_1) \rangle) (I(\vec{\rho}'_2) - \langle I(\vec{\rho}'_2) \rangle) \rangle \\
&= \langle E^*(\vec{\rho}'_1) E(\vec{\rho}'_1) E^*(\vec{\rho}'_2) E(\vec{\rho}'_2) \rangle - \langle I(\vec{\rho}'_1) I(\vec{\rho}'_2) \rangle \\
&= \langle E^*(\vec{\rho}'_1) E(\vec{\rho}'_2) \rangle^2 \\
&\propto |t(\vec{\rho}'_1)|^2 |t(\vec{\rho}'_2)|^2 e^{-\frac{(\vec{\rho}'_1 - \vec{\rho}'_2)^2}{l_c^2}}.
\end{aligned} \tag{6.9}$$

with the coherent length $l_c = \frac{\lambda d''}{\sqrt{2\pi D_S}}$.

6.7 The cumulant formulas

To simplify the calculation, the cumulant formulas are expressed in the moment form. The n_{th} order moment image is defined by

$$\mu_n \equiv M^{(n)}(0) = \left\langle \left(\sum_i h_i \delta I_i \right)^n \right\rangle, \tag{6.10}$$

where $M^{(n)}(\beta) = \langle e^{\beta \delta I(\vec{\rho})} \rangle = \langle e^{\beta \sum_i h_i \delta I_i} \rangle$ is the moment-generating function. The definition of cumulant is given by

$$\kappa_n \equiv K^{(n)}(0), \tag{6.11}$$

where $K^{(n)}(\beta) = \ln \langle e^{\beta \delta I(\vec{\rho})} \rangle = \ln \langle e^{\beta \sum_i h_i \delta I_i} \rangle$ is the cumulant-generating function.

The moment-generating function can be written as $M(\beta) = \exp(K(\beta))$. Taking n^{th} order derivative with respect to β , it reads

$$M^{(n)}(\beta) = \sum_{i=0}^{n-1} \binom{n-1}{i} K^{(n-i)}(\beta) M^{(i)}(\beta). \tag{6.12}$$

Let $\beta = 0$, Eq.(B3) gives

$$\begin{aligned}\mu_n &= \sum_{i=0}^{n-1} \binom{n-1}{i} \kappa_{n-i} \mu_i \\ &= \kappa_n + \sum_{i=1}^{n-1} \binom{n-1}{i} \kappa_{n-i} \mu_i,\end{aligned}\tag{6.13}$$

rewriting gives the recursive relation that

$$\kappa_n = \mu_n - \sum_{i=1}^{n-1} \binom{n-1}{i} \kappa_{n-i} \mu_i.\tag{6.14}$$

The fluctuation intensity sample gives the central moments with $\mu_1 = 0$. Drop all terms in which μ_1 appears, the first six order cumulants in form of moment are listed below:

$$\begin{aligned}\kappa_1 &= \mu_1 \\ \kappa_2 &= \mu_2 \\ \kappa_3 &= \mu_3 \\ \kappa_4 &= \mu_4 - 3\mu_2^2 \\ \kappa_5 &= \mu_5 - 10\mu_3\mu_2 \\ \kappa_6 &= \mu_6 - 15\mu_4\mu_2 - 10\mu_3^2 + 30\mu_2^3.\end{aligned}\tag{6.15}$$

7. CONCLUDING REMARKS

In the later chapter, I would like to highlight the main results that demonstrated from the re-searches presented in this thesis. At last, an outlook of some possible and interesting investigations will be discussed, which can be implemented in our lab.

7.1 Summary of results

The work presented in this thesis mainly studies quantum applications by using a quantum light source: twin-beam squeezed state. This quantum light source is created through the 4WM process in ^{85}Rb vapor, and its noise is 6.5 dB lower than the shot noise limit.

The first investigation is to demonstrated the quantumness of the twin-beam squeezed state. we report a measurement scheme that is capable of acquiring the quantum noise reduction in the temporal domain using an EMCCD camera. We observe $\sim 25\%$ of temporal quantum noise reduction with respect to the shot-noise limit in images captured by the camera. To the best of our knowledge, this is the first experimental showcase that an EMCCD camera can be used to acquire quantum properties of light in the temporal domain.

Then the decoherence effect of a squeezed state has been investigated experimentally, because that squeezed state nowadays has become an extremely versatile tool for precision measurements and for interferometry due to its capability of offering unprecedented measurement sensitivity. We demonstrate a novel and unsophisticated all-optical experimental scheme for studying the decoherence effect on a TMSV state. The significance of our experiment resides in the fact that it demonstrates our capability of directly extracting the decoherence of quantum correlation $\langle \hat{a}\hat{b} \rangle$ between two entangled modes a and b, which is the most important property of a two-mode squeezed state.

The first quantum advantage demonstration with the twin-beam squeezed state is to achieve absorption sensitivity measurement that beyond the shot-noise limit, which is due to the fundamental Poisson distribution of photon number of laser radiation. It is the first experiment that uses

quantum light generated with 4WM instead of SPDC to demonstrate a sub-shot-noise absorption measurement. The fact that our experimental results agree very well with the theory based on the ‘single-mode’ approximation confirms the importance of the narrow band feature of the twin beams. Moreover, the 4WM process offers sufficient gains in a single-pass configuration producing bright quantum-correlated beams of light without a cavity, making it possible to preserve the multi-spatial-mode nature of the bright twin beams.

The second experiment to show the quantum advantage of the twin-beam squeezed state is TPA fluorescence. For the coherent CW excitation both fluorophores show the well-expected quadratic dependence on the input photon flux. The experimental results for fluorescein with SL-TPA, however, demonstrate a linear dependence on the input optical power, along with a ~ 47 -fold TPA fluorescence enhancement. This can be attributed to the predominant occurrence of entangled two-photon absorption of quantum-correlated photon pairs.

At last, we demonstrated an imaging scheme that goes beyond the sub-Rayleigh limit by using speckle illumination with high order correlations. We show that the object’s true features can be recovered where a traditional diffraction-limited imaging method yields a completely blurred image. In addition, and more importantly, we explore using cumulants, which, as demonstrated, show much more improvement as compared to moments. Our results clearly show the capability of higher order intensity cumulants in super-resolution applications where speckles are used. This method widens the possibilities for high order correlation imaging specifically for uses in bio-imaging and astronomy.

7.2 Outlook

Besides the works we have demonstrated in the thesis, there are some ideas of the future research investigations that may provide interesting physics. Here, we will discuss the utility of quantum source in Brillouin light scattering.

7.2.1 Stimulated Brillouin scattering

Brillouin light scattering spectroscopy is based on the interaction of light with traveling density fluctuations (phonons), where an incident photon is converted into a scattered photon with slightly lower or higher energy, usually propagating in the backward direction. The spectrum of the Brillouin scattered light gives access to the mechanical properties of the sample, and has been widely used for studying condensed matter systems, whose material properties in the GHz frequency range, such as in biological samples. Thus, Brillouin scattering spectroscopy in biological systems has attracted increasing interest as a non-contact, label-free and high-resolution fashion detection method.

A conventional stimulated Brillouin scattering(SBS) setup is shown in Fig.7.1, where sample is illuminated by a strong pump field to enhance the signal.

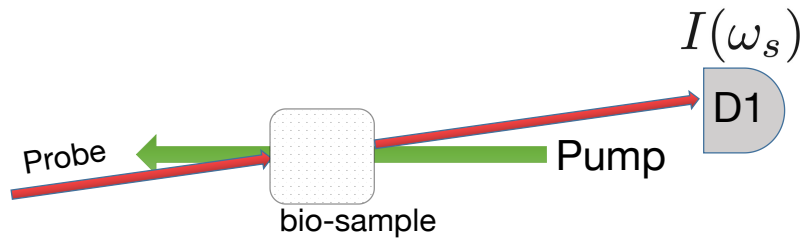


Figure 7.1: Stimulated Brillouin scattering(SBS) setup, where sample is illuminated by a strong pump field to enhance the signal.

Here, a possible research is quantum-enhanced stimulated Brillouin scattering (SBS) measurement with our twin-beam squeezed state to achieve a sensitivity that imply not available through

classical optical methods. The proposed experimental setup for this ultra-sensitive SBS spectroscopy scheme is depicted in Fig. 7.2. A conventional SBS spectroscopy is set up in one of the output beams of the 4WM. The SBS spectroscopy is composed of a strong pump beam and a weak probe (Stokes) beam, which are a few GHz separated and crossed at a small angle on the sample (the angle has to match the Brillouin frequency shift). The other output again acts as a reference beam. Due to the strong quantum correlations between the two output beams, the measurement noise in the SBS spectroscopy path would be largely suppressed by the reference path, yielding a SBS measurement better than any classical approaches.

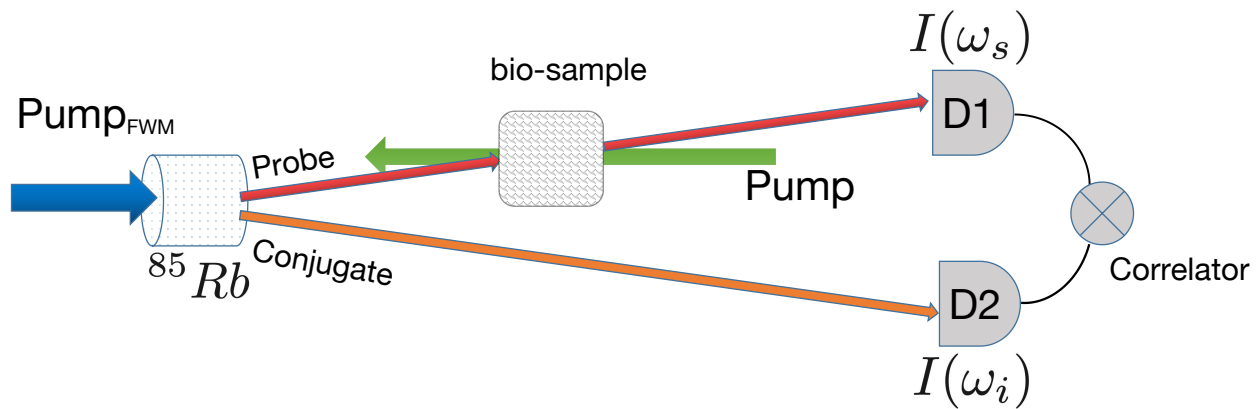


Figure 7.2: Stimulated Brillouin scattering(SBS) setup with squeezed light, where sample is illuminated by a strong pump beam and a probe beam. The correlation detection between the output of probe beam and conjugate beam will suppress the noise, therefore, gives us better result than any classical approaches.

REFERENCES

- [1] M. Dowran, A. Kumar, B. J. Lawrie, R. C. Pooser, and A. M. Marino, “Quantum-enhanced plasmonic sensing,” *Optica*, vol. 5, no. 5, pp. 628–633, 2018.
- [2] L. Cao, J. Qi, J. Du, and J. Jing, “Experimental generation of quadruple quantum-correlated beams from hot rubidium vapor by cascaded four-wave mixing using spatial multiplexing,” *Physical Review A*, vol. 95, no. 2, p. 023803, 2017.
- [3] B. E. Anderson, P. Gupta, B. L. Schmittberger, T. Horrom, C. Hermann-Avigliano, K. M. Jones, and P. D. Lett, “Phase sensing beyond the standard quantum limit with a variation on the su (1, 1) interferometer,” *Optica*, vol. 4, no. 7, pp. 752–756, 2017.
- [4] R. C. Pooser and B. Lawrie, “Ultrasensitive measurement of microcantilever displacement below the shot-noise limit,” *Optica*, vol. 2, no. 5, pp. 393–399, 2015.
- [5] N. Samantaray, I. Ruo-Berchera, A. Meda, and M. Genovese, “Realization of the first sub-shot-noise wide field microscope,” *Light: Science & Applications*, vol. 6, no. 7, pp. e17005–e17005, 2017.
- [6] M. A. Taylor, J. Janousek, V. Daria, J. Knittel, B. Hage, H.-A. Bachor, and W. P. Bowen, “Biological measurement beyond the quantum limit,” *Nature Photonics*, vol. 7, no. 3, pp. 229–233, 2013.
- [7] N. Treps, U. Andersen, B. Buchler, P. K. Lam, A. Maitre, H.-A. Bachor, and C. Fabre, “Surpassing the standard quantum limit for optical imaging using nonclassical multimode light,” *Physical review letters*, vol. 88, no. 20, p. 203601, 2002.
- [8] E. Polzik, J. Carri, and H. Kimble, “Spectroscopy with squeezed light,” *Physical review letters*, vol. 68, no. 20, p. 3020, 1992.
- [9] P. Grangier, R. Slusher, B. Yurke, and A. LaPorta, “Squeezed-light-enhanced polarization interferometer,” *Physical review letters*, vol. 59, no. 19, p. 2153, 1987.

- [10] W. N. Plick, J. P. Dowling, and G. S. Agarwal, “Coherent-light-boosted, sub-shot noise, quantum interferometry,” *New Journal of Physics*, vol. 12, no. 8, p. 083014, 2010.
- [11] A. Kolkiran and G. Agarwal, “Heisenberg limited sagnac interferometry,” *Optics express*, vol. 15, no. 11, pp. 6798–6808, 2007.
- [12] A. Kolkiran and G. Agarwal, “Quantum interferometry using coherent beam stimulated parametric down-conversion,” *Optics express*, vol. 16, no. 9, pp. 6479–6485, 2008.
- [13] R. L. Abrams and R. C. Lind, “Degenerate four-wave mixing in absorbing media,” *Optics letters*, vol. 2, no. 4, pp. 94–96, 1978.
- [14] J. Reintjes, *Nonlinear optical parametric processes in liquids and gases*. Elsevier, 2012.
- [15] N. Bloembergen, “Conservation laws in nonlinear optics,” *JOSA*, vol. 70, no. 12, pp. 1429–1436, 1980.
- [16] R. Slusher, L. Hollberg, B. Yurke, J. Mertz, and J. Valley, “Squeezed states in optical cavities: A spontaneous-emission-noise limit,” *Physical Review A*, vol. 31, no. 5, p. 3512, 1985.
- [17] M. W. Maeda, P. Kumar, and J. H. Shapiro, “Observation of squeezed noise produced by forward four-wave mixing in sodium vapor,” *Optics letters*, vol. 12, no. 3, pp. 161–163, 1987.
- [18] M. Hsu, G. Hétet, A. Peng, C. Harb, H.-A. Bachor, M. Johnsson, J. Hope, P. K. Lam, A. Dantan, J. Cviklinski, *et al.*, “Effect of atomic noise on optical squeezing via polarization self-rotation in a thermal vapor cell,” *Physical Review A*, vol. 73, no. 2, p. 023806, 2006.
- [19] D. Hope, H.-A. Bachor, P. Manson, D. McClelland, and P. Fisk, “Observation of quadrature squeezing in a cavity-atom system,” *Physical Review A*, vol. 46, no. 3, p. R1181, 1992.
- [20] J. Ries, B. Brezger, and A. Lvovsky, “Experimental vacuum squeezing in rubidium vapor via self-rotation,” *Physical Review A*, vol. 68, no. 2, p. 025801, 2003.
- [21] L. Orozco, M. Raizen, M. Xiao, R. Brecha, and H. Kimble, “Squeezed-state generation in optical bistability,” *JOSA B*, vol. 4, no. 10, pp. 1490–1500, 1987.

- [22] M. Vallet, M. Pinard, and G. Grynberg, “Generation of twin photon beams in a ring four-wave mixing oscillator,” *EPL (Europhysics Letters)*, vol. 11, no. 8, p. 739, 1990.
- [23] V. Josse, A. Dantan, L. Vernac, A. Bramati, M. Pinard, and E. Giacobino, “Polarization squeezing with cold atoms,” *Physical review letters*, vol. 91, no. 10, p. 103601, 2003.
- [24] C. McCormick, V. Boyer, E. Arimondo, and P. Lett, “Strong relative intensity squeezing by four-wave mixing in rubidium vapor,” *Optics letters*, vol. 32, no. 2, pp. 178–180, 2007.
- [25] N. V. Corzo, Q. Glorieux, A. M. Marino, J. B. Clark, R. T. Glasser, and P. D. Lett, “Rotation of the noise ellipse for squeezed vacuum light generated via four-wave mixing,” *Physical Review A*, vol. 88, no. 4, p. 043836, 2013.
- [26] A. M. Marino, R. C. Pooser, V. Boyer, and P. D. Lett, “Tunable delay of einstein–podolsky–rosen entanglement,” *Nature*, vol. 457, no. 7231, pp. 859–862, 2009.
- [27] V. Boyer, A. M. Marino, R. C. Pooser, and P. D. Lett, “Entangled images from four-wave mixing,” *Science*, vol. 321, no. 5888, pp. 544–547, 2008.
- [28] Q. Glorieux, L. Guidoni, S. Guibal, J.-P. Likforman, and T. Coudreau, “Quantum correlations by four-wave mixing in an atomic vapor in a nonamplifying regime: Quantum beam splitter for photons,” *Physical Review A*, vol. 84, no. 5, p. 053826, 2011.
- [29] U. Vogl, R. T. Glasser, Q. Glorieux, J. B. Clark, N. V. Corzo, and P. D. Lett, “Experimental characterization of gaussian quantum discord generated by four-wave mixing,” *Physical Review A*, vol. 87, no. 1, p. 010101, 2013.
- [30] A. MacRae, T. Brannan, R. Achal, and A. Lvovsky, “Tomography of a high-purity narrowband photon from a transient atomic collective excitation,” *Physical Review Letters*, vol. 109, no. 3, p. 033601, 2012.
- [31] J. Jing, C. Liu, Z. Zhou, Z. Ou, and W. Zhang, “Realization of a nonlinear interferometer with parametric amplifiers,” *Applied Physics Letters*, vol. 99, no. 1, p. 011110, 2011.

- [32] J. Kong, J. Jing, H. Wang, F. Hudelist, C. Liu, and W. Zhang, “Experimental investigation of the visibility dependence in a nonlinear interferometer using parametric amplifiers,” *Applied Physics Letters*, vol. 102, no. 1, p. 011130, 2013.
- [33] C. M. Caves, “Quantum limits on noise in linear amplifiers,” *Physical Review D*, vol. 26, no. 8, p. 1817, 1982.
- [34] H. P. Yuen, “Two-photon coherent states of the radiation field,” *Physical Review A*, vol. 13, no. 6, p. 2226, 1976.
- [35] M. Reid and D. Walls, “Quantum theory of nondegenerate four-wave mixing,” *Physical Review A*, vol. 34, no. 6, p. 4929, 1986.
- [36] F. Li, T. Li, and G. S. Agarwal, “Temporal quantum noise reduction acquired by an electron-multiplying charge-coupled-device camera,” *Opt. Express*, vol. 28, pp. 37538–37545, Dec 2020.
- [37] R. E. Slusher, L. W. Hollberg, B. Yurke, J. C. Mertz, and J. F. Valley, “Observation of squeezed states generated by four-wave mixing in an optical cavity,” *Phys. Rev. Lett.*, vol. 55, pp. 2409–2412, Nov 1985.
- [38] J. Jing, J. Zhang, Y. Yan, F. Zhao, C. Xie, and K. Peng, “Experimental demonstration of tripartite entanglement and controlled dense coding for continuous variables,” *Phys. Rev. Lett.*, vol. 90, p. 167903, Apr 2003.
- [39] H. Yuen and J. Shapiro, “Optical communication with two-photon coherent states—part i: Quantum-state propagation and quantum-noise,” *IEEE Transactions on Information Theory*, vol. 24, pp. 657–668, November 1978.
- [40] J. Shapiro, H. Yuen, and A. Mata, “Optical communication with two-photon coherent states—part ii: Photoemissive detection and structured receiver performance,” *IEEE Transactions on Information Theory*, vol. 25, pp. 179–192, March 1979.
- [41] S. L. Braunstein and H. J. Kimble, “Dense coding for continuous variables,” *Phys. Rev. A*, vol. 61, p. 042302, Mar 2000.

- [42] C. M. Caves, “Quantum-mechanical noise in an interferometer,” *Phys. Rev. D*, vol. 23, pp. 1693–1708, Apr 1981.
- [43] S. S. Y. Chua, B. J. J. Slagmolen, D. A. Shaddock, and D. E. McClelland, “Quantum squeezed light in gravitational-wave detectors,” *Classical and Quantum Gravity*, vol. 31, p. 183001, sep 2014.
- [44] J. Abadie, B. Abbott, R. Abbott, and et al., “A gravitational wave observatory operating beyond the quantum shot-noise limit,” *Nature Physics*, vol. 7, no. 12, pp. 962–965, 2011.
- [45] J. Aasi, J. Abadie, B. Abbott, and Collaborators, “Enhanced sensitivity of the ligo gravitational wave detector by using squeezed states of light,” *Nature Photonics*, vol. 7, no. 8, pp. 613–619, 2013.
- [46] S. L. Braunstein and H. J. Kimble, “Teleportation of continuous quantum variables,” *Phys. Rev. Lett.*, vol. 80, pp. 869–872, Jan 1998.
- [47] A. Furusawa, J. L. Sørensen, S. L. Braunstein, C. A. Fuchs, H. J. Kimble, and E. S. Polzik, “Unconditional quantum teleportation,” *Science*, vol. 282, no. 5389, pp. 706–709, 1998.
- [48] N. C. Menicucci, P. van Loock, M. Gu, C. Weedbrook, T. C. Ralph, and M. A. Nielsen, “Universal quantum computation with continuous-variable cluster states,” *Phys. Rev. Lett.*, vol. 97, p. 110501, Sep 2006.
- [49] T. Aoki, G. Takahashi, T. Kajiya, J.-i. Yoshikawa, S. L. Braunstein, P. van Loock, and A. Furusawa, “Quantum error correction beyond qubits,” *Nature Physics*, vol. 5, no. 8, pp. 541–546, 2009.
- [50] M. Lassen, M. Sabuncu, A. Huck, J. Niset, G. Leuchs, N. J. Cerf, and U. L. Andersen, “Quantum optical coherence can survive photon losses using a continuous-variable quantum erasure-correcting code,” *Nature Photonics*, vol. 4, no. 10, pp. 700–705, 2010.
- [51] A. A. Berni, T. Gehring, B. M. Nielsen, V. Händchen, M. G. A. Paris, and U. L. Andersen, “Ab initio quantum-enhanced optical phase estimation using real-time feedback control,” *Nature Photonics*, vol. 9, no. 9, pp. 577–581, 2015.

- [52] H. Yonezawa, D. Nakane, T. A. Wheatley, K. Iwasawa, S. Takeda, H. Arao, K. Ohki, K. Tsumura, D. W. Berry, T. C. Ralph, H. M. Wiseman, E. H. Huntington, and A. Furusawa, “Quantum-enhanced optical-phase tracking,” *Science*, vol. 337, no. 6101, pp. 1514–1517, 2012.
- [53] M. D. Reid and P. D. Drummond, “Quantum correlations of phase in nondegenerate parametric oscillation,” *Phys. Rev. Lett.*, vol. 60, pp. 2731–2733, Jun 1988.
- [54] M. D. Reid, P. D. Drummond, W. P. Bowen, E. G. Cavalcanti, P. K. Lam, H. A. Bachor, U. L. Andersen, and G. Leuchs, “Colloquium: The einstein-podolsky-rosen paradox: From concepts to applications,” *Rev. Mod. Phys.*, vol. 81, pp. 1727–1751, Dec 2009.
- [55] Z. Y. Ou, S. F. Pereira, H. J. Kimble, and K. C. Peng, “Realization of the einstein-podolsky-rosen paradox for continuous variables,” *Phys. Rev. Lett.*, vol. 68, pp. 3663–3666, Jun 1992.
- [56] M. I. Kolobov and C. Fabre, “Quantum limits on optical resolution,” *Phys. Rev. Lett.*, vol. 85, pp. 3789–3792, Oct 2000.
- [57] N. Treps, U. Andersen, B. Buchler, P. K. Lam, A. Maître, H.-A. Bachor, and C. Fabre, “Surpassing the standard quantum limit for optical imaging using nonclassical multimode light,” *Phys. Rev. Lett.*, vol. 88, p. 203601, May 2002.
- [58] M. A. Taylor, J. Janousek, V. Daria, J. Knittel, B. Hage, H.-A. Bachor, and W. P. Bowen, “Biological measurement beyond the quantum limit,” *Nature Photonics*, vol. 7, no. 3, pp. 229–233, 2013.
- [59] V. Giovannetti, S. Lloyd, and L. Maccone, “Quantum-enhanced positioning and clock synchronization,” *Nature*, vol. 412, no. 6845, pp. 417–419, 2001.
- [60] F. Wolfgramm, A. Cerè, F. A. Beduini, A. Predojević, M. Koschorreck, and M. W. Mitchell, “Squeezed-light optical magnetometry,” *Phys. Rev. Lett.*, vol. 105, p. 053601, Jul 2010.
- [61] N. Otterstrom, R. C. Pooser, and B. J. Lawrie, “Nonlinear optical magnetometry with accessible in situ optical squeezing,” *Opt. Lett.*, vol. 39, pp. 6533–6536, Nov 2014.

- [62] A. Ourjoumtsev, R. Tualle-Brouri, J. Laurat, and P. Grangier, “Generating optical schrödinger kittens for quantum information processing,” *Science*, vol. 312, no. 5770, pp. 83–86, 2006.
- [63] J. S. Neergaard-Nielsen, B. M. Nielsen, C. Hettich, K. Mølmer, and E. S. Polzik, “Generation of a superposition of odd photon number states for quantum information networks,” *Phys. Rev. Lett.*, vol. 97, p. 083604, Aug 2006.
- [64] F. Dell’Anno, S. D. Siena], and F. Illuminati, “Multiphoton quantum optics and quantum state engineering,” *Physics Reports*, vol. 428, no. 2, pp. 53 – 168, 2006.
- [65] U. L. Andersen, J. S. Neergaard-Nielsen, P. van Loock, and A. Furusawa, “Hybrid discrete- and continuous-variable quantum information,” *Nature Physics*, vol. 11, no. 9, pp. 713–719, 2015.
- [66] J. Eisert, S. Scheel, and M. B. Plenio, “Distilling gaussian states with gaussian operations is impossible,” *Phys. Rev. Lett.*, vol. 89, p. 137903, Sep 2002.
- [67] J. Fiurášek, “Gaussian transformations and distillation of entangled gaussian states,” *Phys. Rev. Lett.*, vol. 89, p. 137904, Sep 2002.
- [68] G. Giedke and J. Ignacio Cirac, “Characterization of gaussian operations and distillation of gaussian states,” *Phys. Rev. A*, vol. 66, p. 032316, Sep 2002.
- [69] J. Niset, J. Fiurášek, and N. J. Cerf, “No-go theorem for gaussian quantum error correction,” *Phys. Rev. Lett.*, vol. 102, p. 120501, Mar 2009.
- [70] S. D. Bartlett, B. C. Sanders, S. L. Braunstein, and K. Nemoto, “Efficient classical simulation of continuous variable quantum information processes,” *Phys. Rev. Lett.*, vol. 88, p. 097904, Feb 2002.
- [71] H. Vahlbruch, M. Mehmet, K. Danzmann, and R. Schnabel, “Detection of 15 db squeezed states of light and their application for the absolute calibration of photoelectric quantum efficiency,” *Phys. Rev. Lett.*, vol. 117, p. 110801, Sep 2016.

- [72] N. Samantaray, I. Ruo-Berchera, A. Meda, and M. Genovese, “Realization of the first sub-shot-noise wide field microscope,” *Light: Science & Applications*, vol. 6, no. 7, pp. e17005–e17005, 2017.
- [73] G. Brida, M. Genovese, and I. Ruo Berchera, “Experimental realization of sub-shot-noise quantum imaging,” *Nature Photonics*, vol. 4, no. 4, pp. 227–230, 2010.
- [74] A. Kumar, H. Nunley, and A. M. Marino, “Observation of spatial quantum correlations in the macroscopic regime,” *Phys. Rev. A*, vol. 95, p. 053849, May 2017.
- [75] A. Kumar and A. M. Marino, “Spatial squeezing in bright twin beams generated with four-wave mixing: Constraints on characterization with an electron-multiplying charge-coupled-device camera,” *Phys. Rev. A*, vol. 100, p. 063828, Dec 2019.
- [76] M. Dowran, A. Kumar, B. J. Lawrie, R. C. Pooser, and A. M. Marino, “Quantum-enhanced plasmonic sensing,” *Optica*, vol. 5, pp. 628–633, May 2018.
- [77] L. Cao, J. Qi, J. Du, and J. Jing, “Experimental generation of quadruple quantum-correlated beams from hot rubidium vapor by cascaded four-wave mixing using spatial multiplexing,” *Phys. Rev. A*, vol. 95, p. 023803, Feb 2017.
- [78] F. Hudelist, J. Kong, C. Liu, J. Jing, Z. Y. Ou, and W. Zhang, “Quantum metrology with parametric amplifier-based photon correlation interferometers,” *Nature Communications*, vol. 5, p. 3049, 01 2014.
- [79] B. E. Anderson, P. Gupta, B. L. Schmittberger, T. Horrom, C. Hermann-Avigliano, K. M. Jones, and P. D. Lett, “Phase sensing beyond the standard quantum limit with a variation on the SU(1,1) interferometer,” *Optica*, vol. 4, pp. 752–756, Jul 2017.
- [80] T. Li, B. E. Anderson, T. Horrom, B. L. Schmittberger, K. M. Jones, and P. D. Lett, “Improved measurement of two-mode quantum correlations using a phase-sensitive amplifier,” *Opt. Express*, vol. 25, pp. 21301–21311, Sep 2017.
- [81] R. C. Pooser and B. Lawrie, “Ultrasensitive measurement of microcantilever displacement below the shot-noise limit,” *Optica*, vol. 2, pp. 393–399, May 2015.

- [82] J. B. Clark, R. T. Glasser, Q. Glorieux, U. Vogl, T. Li, K. M. Jones, and P. D. Lett, “Quantum mutual information of an entangled state propagating through a fast-light medium,” *Nature Photonics*, vol. 8, pp. 515–519, 05 2014.
- [83] T. Li, F. Li, C. Altuzarra, A. Classen, and G. S. Agarwal, “Squeezed light induced two-photon absorption fluorescence of fluorescein biomarkers,” *Applied Physics Letters*, vol. 116, no. 25, p. 254001, 2020.
- [84] C. F. McCormick, A. M. Marino, V. Boyer, and P. D. Lett, “Strong low-frequency quantum correlations from a four-wave-mixing amplifier,” *Phys. Rev. A*, vol. 78, p. 043816, Oct 2008.
- [85] C. F. McCormick, V. Boyer, E. Arimondo, and P. D. Lett, “Strong relative intensity squeezing by four-wave mixing in rubidium vapor,” *Opt. Lett.*, vol. 32, pp. 178–180, Jan 2007.
- [86] R. T. Glasser, U. Vogl, and P. D. Lett, “Stimulated Generation of Superluminal Light Pulses via Four-Wave Mixing,” *Physical Review Letters*, vol. 108, p. 173902, Apr. 2012.
- [87] L. M. Duan, M. D. Lukin, J. I. Cirac, and P. Zoller, “Long-distance quantum communication with atomic ensembles and linear optics,” *Nature*, vol. 414, no. 6862, pp. 413–418, 2001.
- [88] H. Vahlbruch, M. Mehmet, S. Chelkowski, B. Hage, A. Franzen, N. Lastzka, S. Gößler, K. Danzmann, and R. Schnabel, “Observation of squeezed light with 10-db quantum-noise reduction,” *Phys. Rev. Lett.*, vol. 100, p. 033602, Jan 2008.
- [89] N. V. Corzo, A. M. Marino, K. M. Jones, and P. D. Lett, “Noiseless optical amplifier operating on hundreds of spatial modes,” *Phys. Rev. Lett.*, vol. 109, p. 043602, Jul 2012.
- [90] N. Corzo, A. M. Marino, K. M. Jones, and P. D. Lett, “Multi-spatial-mode single-beam quadrature squeezed states of light from four-wave mixing in hot rubidium vapor,” *Opt. Express*, vol. 19, pp. 21358–21369, Oct 2011.
- [91] Y. Shih, *An Introduction to Quantum Optics: Photon and Biphoton Physics*. CRC, Taylor & Francis Publishing Group, 2011.

- [92] V. Buzek and P. L. Knight, *Progress in Optics*, vol. XXXIV. North Holland, Amsterdam, 1995.
- [93] S. Scheel and D.-G. Welsch, “Entanglement generation and degradation by passive optical devices,” *Phys. Rev. A*, vol. 64, p. 063811, Nov 2001.
- [94] A. G. Kofman and G. Kurizki, “Unified theory of dynamically suppressed qubit decoherence in thermal baths,” *Phys. Rev. Lett.*, vol. 93, p. 130406, Sep 2004.
- [95] M. A. Ciampini, G. Pinna, P. Mataloni, and M. Paternostro, “Experimental signature of quantum darwinism in photonic cluster states,” *Phys. Rev. A*, vol. 98, p. 020101, Aug 2018.
- [96] B. A. Stickler, F. T. Ghahramani, and K. Hornberger, “Rotational alignment decay and decoherence of molecular superrotors,” *Phys. Rev. Lett.*, vol. 121, p. 243402, Dec 2018.
- [97] T. K. Unden, D. Louzon, M. Zwolak, W. H. Zurek, and F. Jelezko, “Revealing the emergence of classicality using nitrogen-vacancy centers,” *Phys. Rev. Lett.*, vol. 123, p. 140402, Oct 2019.
- [98] E. Joos, H. Zeh, C. Kiefer, D. Giulini, J. Kupsch, and I. Stamatescu, *Decoherence and the Appearance of a Classical World in Quantum Theory*. Springer, New York, 2003.
- [99] M. Schlosshauer, *Decoherence and the Quantum-to-Classical Transition*. Springer, Berlin/Heidelberg, 2007.
- [100] W. H. Zurek, “Pointer basis of quantum apparatus: Into what mixture does the wave packet collapse?,” *Phys. Rev. D*, vol. 24, pp. 1516–1525, Sep 1981.
- [101] W. H. Zurek, “Environment-induced superselection rules,” *Phys. Rev. D*, vol. 26, pp. 1862–1880, Oct 1982.
- [102] W. H. Zurek, “Decoherence, einselection, and the quantum origins of the classical,” *Rev. Mod. Phys.*, vol. 75, pp. 715–775, May 2003.
- [103] M. Schlosshauer, “Decoherence, the measurement problem, and interpretations of quantum mechanics,” *Rev. Mod. Phys.*, vol. 76, pp. 1267–1305, Feb 2005.

- [104] P. G. Kwiat, A. J. Berglund, J. B. Altepeter, and A. G. White, “Experimental verification of decoherence-free subspaces,” *Science*, vol. 290, no. 5491, pp. 498–501, 2000.
- [105] M. P. Almeida, F. de Melo, M. Hor-Meyll, A. Salles, S. P. Walborn, P. H. S. Ribeiro, and L. Davidovich, “Environment-induced sudden death of entanglement,” *Science*, vol. 316, no. 5824, pp. 579–582, 2007.
- [106] T. Yu and J. H. Eberly, “Sudden death of entanglement,” *Science*, vol. 323, no. 5914, pp. 598–601, 2009.
- [107] T. D. Ladd, F. Jelezko, R. Laflamme, Y. Nakamura, C. Monroe, and J. L. O’Brien, “Quantum computers,” *Nature*, vol. 464, p. 45–53, 2010.
- [108] L. Pezzè, A. Smerzi, M. K. Oberthaler, R. Schmied, and P. Treutlein, “Quantum metrology with nonclassical states of atomic ensembles,” *Rev. Mod. Phys.*, vol. 90, p. 035005, Sep 2018.
- [109] S. S. Esfahani, Z. Liao, and M. S. Zubairy, “Robust quantum state recovery from amplitude damping within a mixed states framework,” *Journal of Physics B: Atomic, Molecular and Optical Physics*, vol. 49, p. 155501, jul 2016.
- [110] W. H. Zurek, “Quantum reversibility is relative, or does a quantum measurement reset initial conditions?,” *Philosophical Transactions of the Royal Society A: Mathematical, Physical and Engineering Sciences*, vol. 376, no. 2123, p. 20170315, 2018.
- [111] J. M. Raimond, M. Brune, and S. Haroche, “Reversible decoherence of a mesoscopic superposition of field states,” *Phys. Rev. Lett.*, vol. 79, pp. 1964–1967, Sep 1997.
- [112] T. Yu and J. H. Eberly, “Quantum open system theory: Bipartite aspects,” *Phys. Rev. Lett.*, vol. 97, p. 140403, Oct 2006.
- [113] G. S. Agarwal and K. Tara, “Transformations of the nonclassical states by an optical amplifier,” *Phys. Rev. A*, vol. 47, pp. 3160–3166, Apr 1993.

- [114] R. C. Pooser, A. M. Marino, V. Boyer, K. M. Jones, and P. D. Lett, “Low-noise amplification of a continuous-variable quantum state,” *Phys. Rev. Lett.*, vol. 103, p. 010501, Jun 2009.
- [115] R. F. Loring and S. Mukamel, “Unified theory of photon echoes: The passage from inhomogeneous to homogeneous line broadening,” *Chemical Physics Letters*, vol. 114, no. 4, pp. 426 – 429, 1985.
- [116] P. R. Berman and R. G. Brewer, “Modified optical bloch equations for solids,” *Phys. Rev. A*, vol. 32, pp. 2784–2796, Nov 1985.
- [117] J. M. Raimond, M. Brune, and S. Haroche, “Manipulating quantum entanglement with atoms and photons in a cavity,” *Rev. Mod. Phys.*, vol. 73, pp. 565–582, Aug 2001.
- [118] M. Arndt, K. Hornberger, and A. Zeilinger, “Probing the limits of the quantum world,” *Physics World*, vol. 18, pp. 35–40, mar 2005.
- [119] A. J. Leggett, “Testing the limits of quantum mechanics: motivation, state of play, prospects,” *Journal of Physics: Condensed Matter*, vol. 14, pp. R415–R451, apr 2002.
- [120] D. Leibfried, R. Blatt, C. Monroe, and D. Wineland, “Quantum dynamics of single trapped ions,” *Rev. Mod. Phys.*, vol. 75, pp. 281–324, Mar 2003.
- [121] M. Aspelmeyer, T. J. Kippenberg, and F. Marquardt, “Cavity optomechanics,” *Rev. Mod. Phys.*, vol. 86, pp. 1391–1452, Dec 2014.
- [122] M. Schlosshauer, “Quantum decoherence,” *Physics Reports*, vol. 831, pp. 1 – 57, 2019.
- [123] L. K. Shalm, M. W. Mitchell, and A. M. Steinberg, “Limitations of quantum process tomography,” in *Quantum Optics and Applications in Computing and Communications II* (G.-C. Guo, H.-K. Lo, M. Sasaki, and S. Liu, eds.), vol. 5631, pp. 60 – 67, International Society for Optics and Photonics, SPIE, 2005.
- [124] M. W. Mitchell, C. W. Ellenor, R. B. A. Adamson, J. S. Lundeen, and A. M. Steinberg, “Quantum process tomography and the search for decoherence-free subspaces,” in *Quantum*

- Information and Computation II* (E. Donkor, A. R. Pirich, and H. E. Brandt, eds.), vol. 5436, pp. 223 – 231, International Society for Optics and Photonics, SPIE, 2004.
- [125] P. H. S. Ribeiro, C. Schwob, A. Maître, and C. Fabre, “Sub-shot-noise high-sensitivity spectroscopy with optical parametric oscillator twin beams,” *Opt. Lett.*, vol. 22, pp. 1893–1895, Dec 1997.
- [126] M. M. Hayat, A. Joobeur, and B. E. A. Saleh, “Reduction of quantum noise in transmittance estimation using photon-correlated beams,” *J. Opt. Soc. Am. A*, vol. 16, pp. 348–358, Feb 1999.
- [127] N. Treps, N. Grosse, W. P. Bowen, C. Fabre, H.-A. Bachor, and P. K. Lam, “A quantum laser pointer,” *Science*, vol. 301, no. 5635, pp. 940–943, 2003.
- [128] V. Giovannetti, S. Lloyd, and L. Maccone, “Quantum-enhanced measurements: Beating the standard quantum limit,” *Science*, vol. 306, no. 5700, pp. 1330–1336, 2004.
- [129] V. D’Auria, C. de Lisio, A. Porzio, S. Solimeno, and M. G. A. Paris, “Transmittivity measurements by means of squeezed vacuum light,” *Journal of Physics B: Atomic, Molecular and Optical Physics*, vol. 39, pp. 1187–1198, feb 2006.
- [130] M. Bondani, A. Allevi, G. Zambra, M. G. A. Paris, and A. Andreoni, “Sub-shot-noise photon-number correlation in a mesoscopic twin beam of light,” *Phys. Rev. A*, vol. 76, p. 013833, Jul 2007.
- [131] J.-L. Blanchet, F. Devaux, L. Furfaro, and E. Lantz, “Measurement of sub-shot-noise correlations of spatial fluctuations in the photon-counting regime,” *Phys. Rev. Lett.*, vol. 101, p. 233604, Dec 2008.
- [132] E. Brambilla, L. Caspani, O. Jedrkiewicz, L. A. Lugiato, and A. Gatti, “High-sensitivity imaging with multi-mode twin beams,” *Phys. Rev. A*, vol. 77, p. 053807, May 2008.
- [133] F. Wolfgramm, C. Vitelli, F. A. Beduini, N. Godbout, and M. W. Mitchell, “Entanglement-enhanced probing of a delicate material system,” *Nature Photonics*, vol. 7, no. 1, pp. 28–32, 2013.

- [134] M. A. Taylor, J. Janousek, V. Daria, J. Knittel, B. Hage, H.-A. Bachor, and W. P. Bowen, “Biological measurement beyond the quantum limit,” *Nature Photonics*, vol. 7, no. 3, pp. 229–233, 2013.
- [135] M. A. Taylor and W. P. Bowen, “Quantum metrology and its application in biology,” *Physics Reports*, vol. 615, pp. 1 – 59, 2016.
- [136] R. Whittaker, C. Erven, A. Neville, M. Berry, J. L. O’Brien, H. Cable, and J. C. F. Matthews, “Absorption spectroscopy at the ultimate quantum limit from single-photon states,” *New Journal of Physics*, vol. 19, p. 023013, feb 2017.
- [137] P.-A. Moreau, J. Sabines-Chesterking, R. Whittaker, S. K. Joshi, P. M. Birchall, A. McMillan, J. G. Rarity, and J. C. F. Matthews, “Demonstrating an absolute quantum advantage in direct absorption measurement,” *Scientific Reports*, vol. 7, no. 1, p. 6256, 2017.
- [138] G. Triginer Garces, H. M. Chrzanowski, S. Daryanoosh, V. Thiel, A. L. Marchant, R. B. Patel, P. C. Humphreys, A. Datta, and I. A. Walmsley, “Quantum-enhanced stimulated emission detection for label-free microscopy,” *Applied Physics Letters*, vol. 117, no. 2, p. 024002, 2020.
- [139] W. N. Plick, J. P. Dowling, and G. S. Agarwal, “Coherent-light-boosted, sub-shot noise, quantum interferometry,” *New Journal of Physics*, vol. 12, p. 083014, aug 2010.
- [140] A. Kolkiran and G. S. Agarwal, “Quantum interferometry using coherent beam stimulated parametric down-conversion,” *Opt. Express*, vol. 16, pp. 6479–6485, Apr 2008.
- [141] N. Thomas-Peter, B. J. Smith, A. Datta, L. Zhang, U. Dorner, and I. A. Walmsley, “Real-world quantum sensors: Evaluating resources for precision measurement,” *Phys. Rev. Lett.*, vol. 107, p. 113603, Sep 2011.
- [142] S. N. Arkipov, I. Saytashev, and M. Dantus, “Intravital imaging study on photodamage produced by femtosecond near-infrared laser pulses in vivo,” *Photochemistry and Photobiology*, vol. 92, no. 2, pp. 308–313, 2016.

- [143] G. Y. Xiang, B. L. Higgins, D. W. Berry, H. M. Wiseman, and G. J. Pryde, “Entanglement-enhanced measurement of a completely unknown optical phase,” *Nature Photonics*, vol. 5, no. 1, pp. 43–47, 2011.
- [144] A. A. Berni, T. Gehring, B. M. Nielsen, V. Händchen, M. G. A. Paris, and U. L. Andersen, “Ab initio quantum-enhanced optical phase estimation using real-time feedback control,” *Nature Photonics*, vol. 9, no. 9, pp. 577–581, 2015.
- [145] M. Xiao, L.-A. Wu, and H. J. Kimble, “Detection of amplitude modulation with squeezed light for sensitivity beyond the shot-noise limit,” *Opt. Lett.*, vol. 13, pp. 476–478, Jun 1988.
- [146] K. Schneider, R. Bruckmeier, H. Hansen, S. Schiller, and J. Mlynek, “Bright squeezed-light generation by a continuous-wave semimonolithic parametric amplifier,” *Opt. Lett.*, vol. 21, pp. 1396–1398, Sep 1996.
- [147] T. Ono, R. Okamoto, and S. Takeuchi, “An entanglement-enhanced microscope,” *Nature Communications*, vol. 4, no. 1, p. 2426, 2013.
- [148] T. S. Iskhakov, V. C. Usenko, U. L. Andersen, R. Filip, M. V. Chekhova, and G. Leuchs, “Heralded source of bright multi-mode mesoscopic sub-poissonian light,” *Opt. Lett.*, vol. 41, pp. 2149–2152, May 2016.
- [149] F. Li, T. Li, and G. Agarwal, “Temporal quantum noise reduction acquired by an electron-multiplying charge-coupled-device camera,” *arXiv:2005.00108*, no. :2005.00108, 2020.
- [150] E. Knyazev, F. Y. Khalili, and M. V. Chekhova, “Overcoming inefficient detection in sub-shot-noise absorption measurement and imaging,” *Opt. Express*, vol. 27, pp. 7868–7885, Mar 2019.
- [151] A. Jechow, A. Heuer, and R. Menzel, “High brightness, tunable biphoton source at 976 nm for quantum spectroscopy,” *Opt. Express*, vol. 16, pp. 13439–13449, Aug 2008.
- [152] J. P. Villabona-Monsalve, O. Varnavski, B. A. Palfey, and T. Goodson, “Two-photon excitation of flavins and flavoproteins with classical and quantum light,” *Journal of the American Chemical Society*, vol. 140, pp. 14562–14566, 11 2018.

- [153] O. Varnavski, B. Pinsky, and T. Goodson, “Entangled photon excited fluorescence in organic materials: An ultrafast coincidence detector,” *The Journal of Physical Chemistry Letters*, vol. 8, pp. 388–393, 01 2017.
- [154] M. Genovese, “Real applications of quantum imaging,” *Journal of Optics*, vol. 18, p. 073002, jun 2016.
- [155] M. I. Kolobov, *Quantum Imaging*. Springer, New York, 2007.
- [156] T. Li, F. Li, C. Altuzarra, A. Classen, and G. S. Agarwal, “Squeezed light induced two-photon absorption fluorescence of fluorescein biomarkers,” *Applied Physics Letters*, vol. 116, no. 25, p. 254001, 2020.
- [157] B. Mollow, “Two-photon absorption and field correlation functions,” *Physical Review*, vol. 175, no. 5, p. 1555, 1968.
- [158] J. Gea-Banacloche, “Two-photon absorption of nonclassical light,” *Physical review letters*, vol. 62, no. 14, p. 1603, 1989.
- [159] F. Helmchen and W. Denk, “Deep tissue two-photon microscopy,” *Nature Methods*, vol. 2, pp. 932 EP –, 11 2005.
- [160] J. B. Pawley, ed., *Handbook of Biological Confocal Microscopy*. Plenum, New York, 1995.
- [161] C. Xu, W. Zipfel, J. B. Shear, R. M. Williams, and W. W. Webb, “Multiphoton fluorescence excitation: new spectral windows for biological nonlinear microscopy,” *Proceedings of the National Academy of Sciences*, vol. 93, no. 20, pp. 10763–10768, 1996.
- [162] W. R. Zipfel, R. M. Williams, and W. W. Webb, “Nonlinear magic: multiphoton microscopy in the biosciences,” *Nature Biotechnology*, vol. 21, no. 11, pp. 1369–1377, 2003.
- [163] M. Drobizhev, N. S. Makarov, S. E. Tillo, T. E. Hughes, and A. Rebane, “Two-photon absorption properties of fluorescent proteins,” *Nature Methods*, vol. 8, no. 5, pp. 393–399, 2011.

- [164] L. Upton, M. Harpham, O. Suzer, M. Richter, S. Mukamel, and T. Goodson, “Optically excited entangled states in organic molecules illuminate the dark,” *The Journal of Physical Chemistry Letters*, vol. 4, pp. 2046–2052, 06 2013.
- [165] C. Xu and W. W. Webb, “Measurement of two-photon excitation cross sections of molecular fluorophores with data from 690 to 1050 nm,” *J. Opt. Soc. Am. B*, vol. 13, pp. 481–491, Mar 1996.
- [166] M. A. Albota, C. Xu, and W. W. Webb, “Two-photon fluorescence excitation cross sections of biomolecular probes from 690 to 960 nm,” *Appl. Opt.*, vol. 37, pp. 7352–7356, Nov 1998.
- [167] B.-C. Chen, W. R. Legant, K. Wang, L. Shao, D. E. Milkie, M. W. Davidson, C. Janetopoulos, X. S. Wu, J. A. Hammer, Z. Liu, B. P. English, Y. Mimori-Kiyosue, D. P. Romero, A. T. Ritter, J. Lippincott-Schwartz, L. Fritz-Laylin, R. D. Mullins, D. M. Mitchell, J. N. Benbenek, A.-C. Reymann, R. Böhme, S. W. Grill, J. T. Wang, G. Seydoux, U. S. Tulu, D. P. Kiehart, and E. Betzig, “Lattice light-sheet microscopy: Imaging molecules to embryos at high spatiotemporal resolution,” *Science*, vol. 346, no. 6208, 2014.
- [168] J. P. Villabona-Monsalve, O. Calderón-Losada, M. Nuñez Portela, and A. Valencia, “Entangled two photon absorption cross section on the 808 nm region for the common dyes zinc tetraphenylporphyrin and rhodamine b,” *The Journal of Physical Chemistry A*, vol. 121, pp. 7869–7875, 10 2017.
- [169] J. Gea-Banacloche, “Two-photon absorption of nonclassical light,” *Phys. Rev. Lett.*, vol. 62, pp. 1603–1606, Apr 1989.
- [170] J. Javanainen and P. L. Gould, “Linear intensity dependence of a two-photon transition rate,” *Phys. Rev. A*, vol. 41, pp. 5088–5091, May 1990.
- [171] N. P. Georgiades, E. S. Polzik, K. Edamatsu, H. J. Kimble, and A. S. Parkins, “Nonclassical excitation for atoms in a squeezed vacuum,” *Phys. Rev. Lett.*, vol. 75, pp. 3426–3429, Nov 1995.

- [172] H.-B. Fei, B. M. Jost, S. Popescu, B. E. A. Saleh, and M. C. Teich, “Entanglement-induced two-photon transparency,” *Phys. Rev. Lett.*, vol. 78, pp. 1679–1682, Mar 1997.
- [173] M. C. Teich and B. E. A. Saleh, “Entangled-photon microscopy,” *Československý časopis pro fyziku*, vol. 47, no. 3, 1997.
- [174] T. Robertson, F. Bunel, and M. Roberts, “Fluorescein derivatives in intravital fluorescence imaging,” *Cells*, vol. 2, no. 3, p. 591, 2013.
- [175] B. R. Mollow, “Two-photon absorption and field correlation functions,” *Phys. Rev.*, vol. 175, pp. 1555–1563, Nov 1968.
- [176] R. d. J. León-Montiel, J. c. v. Svozilík, J. P. Torres, and A. B. U’Ren, “Temperature-controlled entangled-photon absorption spectroscopy,” *Phys. Rev. Lett.*, vol. 123, p. 023601, Jul 2019.
- [177] M. R. Harpham, Ö. Süzer, C.-Q. Ma, P. Bäuerle, and T. Goodson, “Thiophene dendrimers as entangled photon sensor materials,” *Journal of the American Chemical Society*, vol. 131, pp. 973–979, 01 2009.
- [178] A. Jechow, M. Seefeldt, H. Kurzke, A. Heuer, and R. Menzel, “Enhanced two-photon excited fluorescence from imaging agents using true thermal light,” *Nature Photonics*, vol. 7, p. 973, 10 2013.
- [179] T. Scheul, C. D’Amico, I. Wang, and J.-C. Vial, “Two-photon excitation and stimulated emission depletion by a single wavelength,” *Opt. Express*, vol. 19, pp. 18036–18048, Sep 2011.
- [180] J. Javanainen and P. L. Gould, “Linear intensity dependence of a two-photon transition rate,” *Physical Review A*, vol. 41, pp. 5088–5091, 05 1990.
- [181] F. Li, C. Altuzarra, T. Li, M. O. Scully, and G. S. Agarwal, “Beyond sub-rayleigh imaging via high order correlation of speckle illumination,” *Journal of Optics*, vol. 21, p. 115604, oct 2019.

- [182] J. W. Goodman, *Speckle phenomena in optics: theory and applications*. Roberts and Company Publishers, 2007.
- [183] J. W. Goodman, “Some fundamental properties of speckle,” *JOSA*, vol. 66, no. 11, pp. 1145–1150, 1976.
- [184] A. Dunn, H. Bolay, M. A. Moskowitz, and D. Boas, “Dynamic imaging of cerebral blood flow using laser speckle,” *Journal of Cerebral Blood Flow & Metabolism*, vol. 21, no. 3, pp. 195–201, 2001.
- [185] J. C. Dainty, *Laser Speckle and Related Phenomena*. Springer-Verlag Berlin Heidelberg, 1975.
- [186] A. Gatti, E. Brambilla, and L. Lugiato, “Progress in optics vol 51 ed e wolf,” 2008.
- [187] F. Devaux, K. Huy, S. Denis, E. Lantz, and P. Moreau, “Temporal ghost imaging with pseudo-thermal speckle light,” *Journal of Optics*, vol. 19, p. 024001, dec 2016.
- [188] Y. Zhou, J. Liu, J. Simon, and Y. Shih, “Resolution enhancement of third-order thermal light ghost imaging in the photon counting regime,” *JOSA B*, vol. 29, no. 3, pp. 377–381, 2012.
- [189] A. Dogariu and S. Amarande, “Propagation of partially coherent beams: turbulence-induced degradation,” *Optics letters*, vol. 28, no. 1, pp. 10–12, 2003.
- [190] T. Shirai, A. Dogariu, and E. Wolf, “Mode analysis of spreading of partially coherent beams propagating through atmospheric turbulence,” *JOSA A*, vol. 20, no. 6, pp. 1094–1102, 2003.
- [191] G. Siviloglou, J. Broky, A. Dogariu, and D. Christodoulides, “Observation of accelerating airy beams,” *Physical Review Letters*, vol. 99, no. 21, p. 213901, 2007.
- [192] E. Baleine, A. Dogariu, and G. S. Agarwal, “Correlated imaging with shaped spatially partially coherent light,” *Optics letters*, vol. 31, no. 14, pp. 2124–2126, 2006.
- [193] A. Gatti, E. Brambilla, M. Bache, and L. A. Lugiato, “Ghost imaging with thermal light: comparing entanglement and classical correlation,” *Physical review letters*, vol. 93, no. 9, p. 093602, 2004.

- [194] A. Valencia, G. Scarcelli, M. D’Angelo, and Y. Shih, “Two-photon imaging with thermal light,” *Physical review letters*, vol. 94, no. 6, p. 063601, 2005.
- [195] M. Lahiri, E. Wolf, D. G. Fischer, and T. Shirai, “Determination of correlation functions of scattering potentials of stochastic media from scattering experiments,” *Physical review letters*, vol. 102, no. 12, p. 123901, 2009.
- [196] F. T. Arecchi, “Measurement of the statistical distribution of gaussian and laser sources,” *Physical Review Letters*, vol. 15, no. 24, p. 912, 1965.
- [197] A. Classen, J. von Zanthier, M. O. Scully, and G. S. Agarwal, “Superresolution via structured illumination quantum correlation microscopy,” *Optica*, vol. 4, no. 6, pp. 580–587, 2017.
- [198] J. Oh, Y. Cho, G. Scarcelli, and Y. Kim, “Sub-rayleigh imaging via speckle illumination,” *Optics letters*, vol. 38, no. 5, pp. 682–684, 2013.
- [199] Y. Wang, F. Wang, R. Liu, D. Chen, H. Gao, P. Zhang, and F. Li, “Spatial sub-rayleigh imaging analysis via speckle laser illumination,” *Optics letters*, vol. 40, no. 22, pp. 5323–5326, 2015.
- [200] T. A. Smith and Y. Shih, “Turbulence-free double-slit interferometer,” *Physical review letters*, vol. 120, no. 6, p. 063606, 2018.
- [201] J. Sprigg, T. Peng, and Y. Shih, “Super-resolution imaging using the spatial-frequency filtered intensity fluctuation correlation,” *Scientific reports*, vol. 6, p. 38077, 2016.
- [202] T. Dertinger, R. Colyer, G. Iyer, S. Weiss, and J. Enderlein, “Fast, background-free, 3d super-resolution optical fluctuation imaging (sofi),” *Proceedings of the National Academy of Sciences*, vol. 106, no. 52, pp. 22287–22292, 2009.
- [203] A. Vigoren and J. M. Zavislan, “Optical sectioning enhancement using higher-order moment signals in random speckle-structured illumination microscopy,” *JOSA A*, vol. 35, no. 3, pp. 474–479, 2018.

- [204] S. Oppel, R. Wiegner, G. Agarwal, and J. von Zanthier, “Directional superradiant emission from statistically independent incoherent nonclassical and classical sources,” *Physical review letters*, vol. 113, no. 26, p. 263606, 2014.
- [205] K. Chan, M. O’Sullivan, and R. Boyd, “High-order thermal ghost imaging,” *Optics letters*, vol. 34, no. 21, pp. 3343–3345, 2009.
- [206] Y. Shih, *An introduction to quantum optics: photon and biphoton physics*. CRC press, 2016.
- [207] A. Lyons, F. Tonolini, A. Boccolini, A. Repetti, R. Henderson, Y. Wiaux, and D. Faccio, “Computational time-of-flight diffuse optical tomography,” *Nat. Phot.*, vol. 13, p. 575–579, 2019.
- [208] D. A. Boas and A. K. Dunn, “Laser speckle contrast imaging in biomedical optics,” *Journal of biomedical optics*, vol. 15, no. 1, p. 011109, 2010.
- [209] M. A. Davis, L. Gagnon, D. A. Boas, and A. K. Dunn, “Sensitivity of laser speckle contrast imaging to flow perturbations in the cortex,” *Biomedical optics express*, vol. 7, no. 3, pp. 759–775, 2016.
- [210] J. D. Briers and S. Webster, “Laser speckle contrast analysis (lasca): a non-scanning, full-field technique for monitoring capillary blood flow,” *Journal of biomedical optics*, vol. 1, no. 2, pp. 174–180, 1996.
- [211] A. Aminfar, N. Davoodzadeh, G. Aguilar, and M. Princevac, “Application of optical flow algorithms to laser speckle imaging,” *Microvascular Research*, vol. 122, pp. 52 – 59, 2019.
- [212] R. Zhang, L. Song, J. Xu, X. An, W. Sun, X. Zhao, Z. Zhou, and L. Chen, “Laser speckle imaging for blood flow based on pixel resolved zero-padding auto-correlation coefficient distribution,” *Optics Communications*, vol. 439, pp. 38 – 46, 2019.
- [213] E. H. S Howell, “High-resolution speckle imaging,” *Physics Today*, vol. 71, no. 11, pp. 78–79, 2018.